AD/A-003 823

IMPROVED BLACKBODY SIMULATOR

W. L. Wolfe, et al

Arizona University

Prepared for:

Space and Missile Systems Organization
Advanced Research Projects Agency

June 1974

SEC... TY CLASSIFICATION OF THIS PAGE (When Data Entered)

REPORT DOCUMENTATION PAGE		READ INSTRUCTIONS BEFORE COMPLETING FORM
1 REPORT NUMBER SAMSO TR 74-206	2. GOVT ACCESSION NO.	3 RECIPIENT'S CATALOG NUMBER
4. TITLE (and Subtitle) IMPROVED BLACKBODY SIMULATOR		5. TYPE OF REPORT & PERIOD COVERED Final Aug. 1972 - March 1974
		6. PERFORMING ORG. REPORT NUMBER
7. AUTHOR(s) W. L. Wolfe and F. O. Bartell		8. CONTRACT OR GRANT NUMBER(s) FO-4701-72-C-0401
9. PERFORMING ORGANIZATION NAME AND ADDRESS Optical Sciences Center University of Arizona Tucson, Arizona 85721		10. PROGRAM ELEMENT. PROJECT, TASK AREA & WORK UNIT NUMBERS
11. CONTROLLING OFFICE NAME AND ADDRESS Space and Missile Systems Organization (AFSC) P.O. Box 92960, Worldway Postal Center Los Angeles, California 90009		12. REPORT DATE June 1974
		13. NUMBER OF PAGES 184
14. MONITORING AGENCY NAME & ADDRESS(if different from Controlling Office)		15 SECURITY CLASS. (of this report) Unclassified
		15a. DECLASSIFICATION/DOWNGRADING SCHEDULE --

16. DISTRIBUTION STATEMENT (of this Report)

Approved for public release; distribution unlimited.

17. DISTRIBUTION STATEMENT (of the abstract entered in Block 20, if different from Report)

18. SUPPLEMENTARY NOTES

19. KEY WORDS (Continue on reverse side if necessary and identify by block number)

Blackbody
Blackbody simulator
Polythermal blackbody simulators

20. ABSTRACT (Continue on reverse side if necessary and identify by block number)

A study, design, and fabrication effort has resulted in an Improved Blackbody Simulator for the AEDC 7V Chamber Infrared Simulator. During the course of the work, a sequence of problems was confronted and solved.

A theoretical and experimental investigation to determine the best cavity shape led to a new shape theory for blackbody simulator cavities. The new theory shows that all geometrical shape effects can be expressed in terms of

DD FORM 1473 EDITION OF 1 NOV 65 IS OBSOLETE
S/N 0102-014-6601 1

PRICES SUBJECT TO CHANGE

20. Abstract (cont.)

$\int_a d\Omega$, the projected solid angle of the aperture as seen from a point on the cavity wall. This investigation also considered cavity temperature uniformity and cavity emittance uniformity. As a result of the investigation, a spherical cavity shape was selected in contrast to the customary conical cavity.

A study of core and wall materials resulted in the choice of aluminum type 6061-T6 with a hard black anodized coating called Hardas. The aluminum provides excellent thermal conductivity to aid in achieving uniform cavity temperature, and the Hardas coating provides a rugged, stable emitting surface. The wall emissivity is 0.9 or higher except from 3.0 to 7.0 µm, where it is between 0.71 and 0.91. A computer program for polythermal cavity effects showed spectral radiance errors of about 0.5% or less over the range 2 to 32 µm.

A study of temperature control and uniformity led to selection of an Artronix Model 5301-E temperature controller used with Rosemount platinum resistance thermometers. Temperature uniformity is about 1 K or better, and temperature stability and control are about 50 mK or better.

A study of attenuation and calibration showed the best technique to be a sequence of demagnifying optical modules. This method can provide stable, reliable, predictable signals at very low levels. It has excellent uniformity as a function of wavelength, and it can incorporate self-contained and self-checked calibration capabilities.

A study of the 7V Chamber optical system resulted in a new design that adds a toroidal concave mirror and a hyperbolic concave mirror to the existing large concave spherical mirror. The new design has a nominal half-angle tilt of 5°, and along this axis the imagery is about 40 times better than in the present system.

The Improved Blackbody Simulator can be calibrated in two ways, with NBS traceability for both. The first is on the basis of aperture diameter and cavity temperature measurements, and the second is on the basis of sending the Improved Blackbody Simulator to NBS for calibration in the low-temperature blackbody simulator calibration facility.

Features of the Improved Blackbody Simulator include the following: a 38-mm (1.5-in.) diameter cylinder having, near one end, a 32-mm (1.25-in.) diameter spherical cavity with a 5.1-mm (0.20-in.) diameter aperture; a heater consisting of 25-AWG nichrome wire wrapped around the cylinder; electrical insulation for the heater consisting of an anodized coating on the aluminum cylinder plus a fiberglass sheath around the wire; thermal insulation for the heated core consisting of alternating layers of fiberglass cloth and aluminum foil; further thermal insulation in the form of two concentric cylindrical radiation shields with the precision, 0.696-mm (0.0274-in.) diameter aperture a part of the inner cylinder; support for the core consisting of three steel pins near the aperture and a thin-walled (0.15-mm, or 0.006-in.) steel tube at the opposite end; an off-axis design to avoid specular reflection from the back wall, achieved by using a symmetric core with a 17.5° tilted base plate and a countertilted aperture arrangement.

FOREWORD

This technical report, prepared by the Optical Sciences Center, University of Arizona summarizes a study, design, and fabrication effort for an Improved Blackbody Simulator. The work was performed under U.S. Air Force contract FO-4701-72-C-0401 during the period August 1972 through March 1974.

Blackbody simulators are commonly used for standards and test equipment in infrared measurement programs. However, advances in infrared technology have required improved accuracy for infrared standards used in high-vacuum, low-temperature environments. For this reason, a contract was sponsored by the Advanced Research Projects Agency (ARPA) in cooperation with the Management Office, SAMSO/SYJT, and the using agency, Arnold Engineering and Development Center (AEDC).

The study covered cavity shape, core material, cavity wall coating, temperature uniformity, emittance uniformity, temperature measurement and control, attenuation and calibration methods, optical analysis and design, NBS traceable calibration, and fabrication methods. The results of the study led to the design and fabrication of the Improved Blackbody Simulator. Over-all performance characteristics include temperature stability and control of about 50 mK, temperature uniformity of about 1 K, and spectral radiance accuracy of about 0.5% or better.

The Improved Blackbody Simulator was delivered to AEDC for use in the 7V Chamber Infrared Simulator.

The use of trade names in this report does not constitute official endorsement or approval of the use of such commercial hardware. This report may not be cited for purposes of advertisement.

Publication of this report does not constitute Air Force approval of the report's findings or conclusions. It is published only for the exchange and stimulation of ideas.

W. L. Wolfe
Principal Investigator
Optical Sciences Center

F. O. Bartell
Project Scientist
Optical Sciences Center

ii

TABLE OF CONTENTS

iii

TABLE OF CONTENTS--Continued

TABLE OF CONTENTS--<u>Continued</u>

LIST OF ILLUSTRATIONS

LIST OF TABLES

SECTION 1

CAVITY SHAPE

Our study has shown that the best cavity shape for a blackbody simulator for the 7V IR Simulator application is a sphere. The superiority of the sphere has been shown both theoretically and experimentally--with equations, theoretical curves, and experimental graphs. This result is in contrast to common practice as indicated on pp. 52-55 of the *Handbook of Military Infrared Technology*, W. Wolfe, editor, 1965, where 27 commercially available blackbody simulators are listed and 23 of these have conical cavities.

The new theory is derived in Appendix A, where it is shown that nearly all cavity geometry effects can be expressed in terms of $\int_a d\Omega$, the projected solid angle of the aperture as seen from a point on the cavity wall. Variations in $\int_a \Omega$ for different points on the wall of the cavity correspond to variations in infrared signals in a collimated beam for blackbody simulators used with collimators. This theory is especially important for the 7V IR Simulator application, where a relatively fast $f/4$ optical system must be filled.

Figure 1 (which is identical to Fig. A2 in Appendix A) shows the geometrical arrangement corresponding to the new theory. Equation (A14) of Appendix A is the result of the theory; it is give here as Eq. (1):

$$
\begin{aligned}
E_d \;=\; & A_\alpha \ell_\alpha^{-2} \sigma T_t^4 \pi^{-1} \epsilon \;+\; A_\alpha \ell_\alpha^{-2} \sigma T_m^4 \pi^{-1} (1-\epsilon) \\[2mm]
& - A_\alpha \ell_\alpha^{-2} \sigma T_m^4 \pi^{-1} (1-\epsilon)\pi^{-1} \int_a d\Omega_{10} \\[2mm]
& - A_\alpha \ell_\alpha^{-2} \sigma T_t^4 \pi^{-1} \Bigg[4\epsilon^2 \sigma T_0^4 T_t^{-1} r_0 \big[\ln(r_c/r_0) K_{0c}^{-1} \\
& \qquad\qquad\qquad\qquad + \ln(r_t/r_c) K_{ct}^{-1}\big]\pi^{-1} \Bigg] \int_a d\Omega_{10}
\end{aligned}
$$

(equation continued)

1
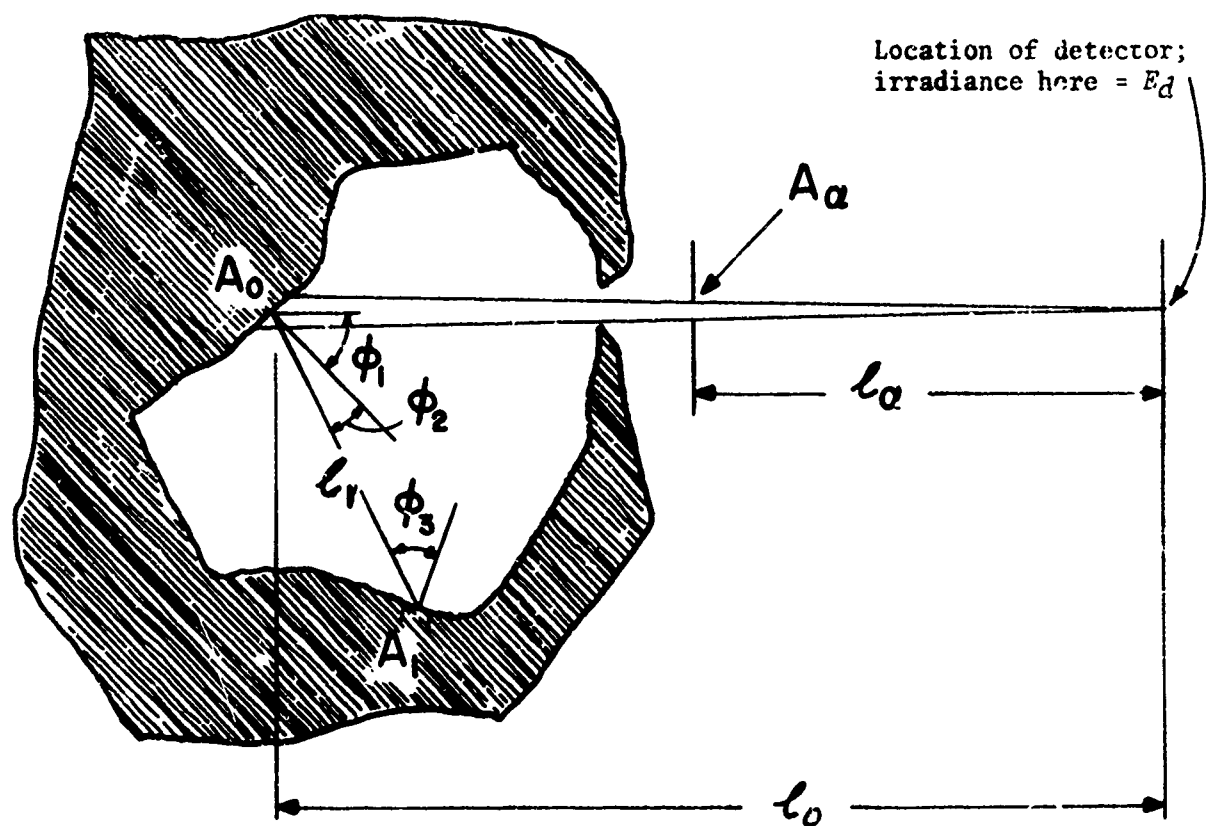
Fig. 1. Geometry for Theory.

$$- A_a \ell_a^{-2} \sigma T_m^4 \pi^{-1} (1-\epsilon)^2 \epsilon^{-1} \pi^{-1} \overline{\int_a d\Omega}$$

$$\cdot \left[1 - \pi^{-1} \int_a d\Omega_{10} \right] \left[1 + \frac{1-\epsilon}{\pi\epsilon} \overline{\int_a d\Omega} \right]^{-1}.$$

(1)

This equation has five terms, which can be interpreted one term at a time:

The first term is the radiation from a surface at temperature T_t with surface emissivity ϵ. Note that T_t is the temperature at a point inside the core some distance away from A_0, where A_0 is at temperature T_0. The difference between T_t and T_0 will be described under the discussion of the fourth term.

The second term is the radiation originating in the cavity at a special mean temperature T_m and then reflected from the surface with a reflectivity of $(1-\epsilon)$.

The third term is like the second, but it has a negative sign and a multiplying factor $\pi^{-1} \int_a d\Omega_{10}$. This term represents the deficiency in reflected radiation due to the aperture: The larger the projected solid angle of the aperture as given by $\pi^{-1} \int_a d\Omega_{10}$, the larger the deficiency of the reflected radiation.

The fourth term represents the deficiency in emitted radiation due to a temperature difference $T_t - T_0$. This term assumes that there is a core with a coating. The core is usually selected for high conductivity and the coating for high emissivity. Figure 2 (the same as Fig. A3 in Appendix A) shows the geometrical relationships between T_t and T_0. Here r_o locates the cavity surface, r_c locates the interface between core and coating, and r_t locates the position where the temperature is measured. K_{oc} is the conduc-
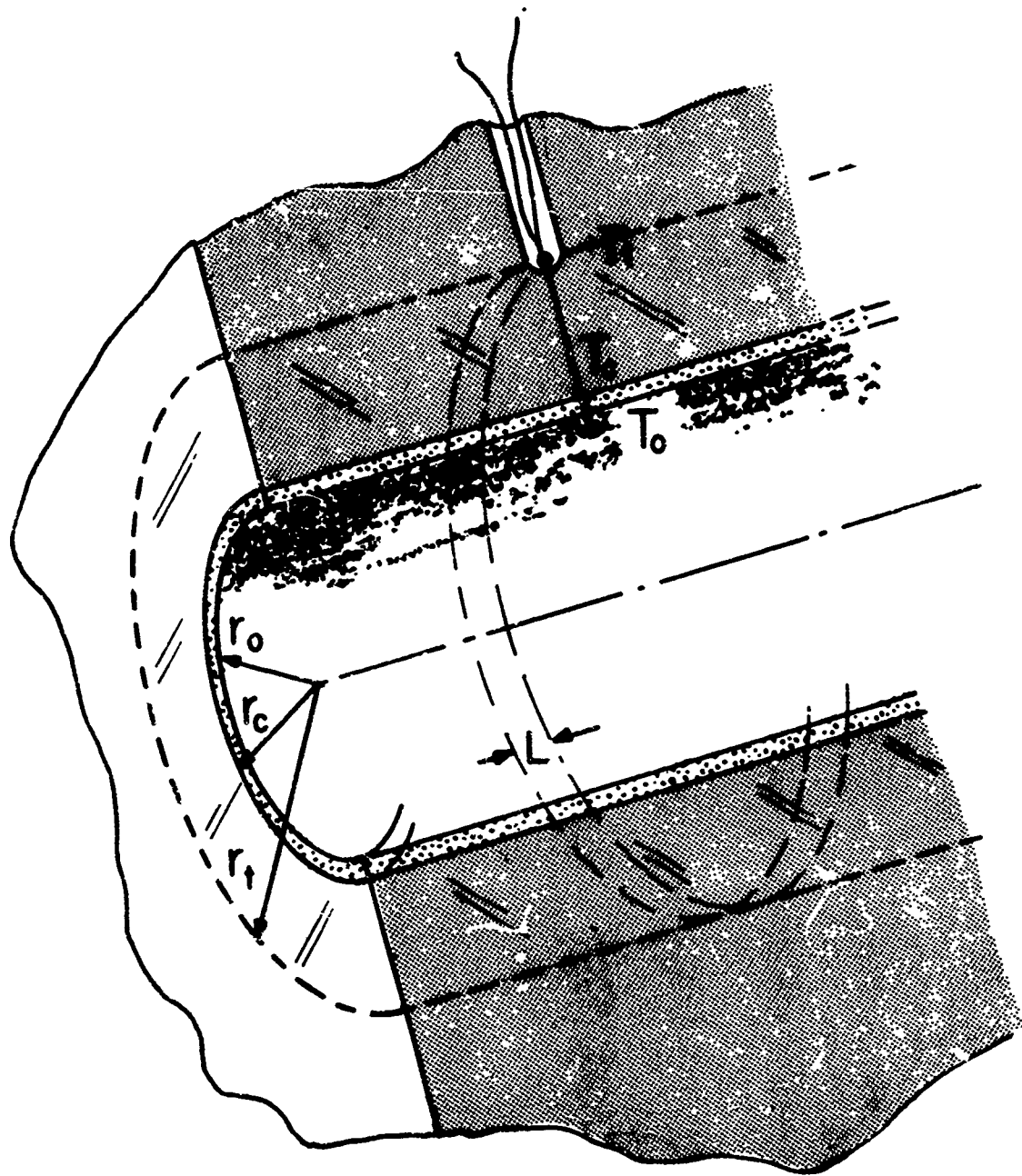
Fig. 2. T_0, T_t Geometry.

tivity of the coating, and K_{ct} is the conductivity of the core. Note that this term has the same factor $\pi^{-1} \int_a d\Omega_{10}$ as the previous term. This shows the effects of the projected solid angle of the aperture on the temperature difference and also on the signal at the detector.

Finally, the fifth term is a higher order correction in $(1-\epsilon)^2$, ϵ, $\pi^{-1} \int_a d\Omega_{10}$, and a mean value of this integral, $\overline{\int_a d\Omega}$. For good blackbody simulator design, ϵ will be about 0.9 or more and $\overline{\int_a d\Omega}$ will be 0.1 or less, and then this fifth term can be neglected.

Reviewing our interpretation of Eq. (1), we see that the first two terms represent simple emission and reflection, the third term shows aperture effects on the reflected radiation, and the fourth term shows aperture effects on temperature differences. It is most important to note that all cavity geometry effects are manifest in the factor $\pi^{-1} \int_a d\Omega_{10}$, which is common to the third and fourth terms. Since a primary task of contract F04701-72-C-0401 is to select the best cavity shape for the 7V IR Simulator application, a study of this factor is very important.

Section A3 of Appendix A provides an evaluation of the aperture effect factor $\pi^{-1} \int_a d\Omega_{10}$. Equations (A19), (A20), and (A21) summarize that analysis for sphere, cone, and cylinder side wall:

$$\pi^{-1} \int_a d\Omega \;=\; a^2/4R^2 \qquad\qquad \text{(sphere)} \qquad \text{(A19)}$$

$$\pi^{-1} \int_a d\Omega \;=\; za^3(1 + a^2/h^2)^{-\frac{1}{2}}[z^2 + a^2(1 - z/h)^2]^{-2} \qquad \text{(cone)} \qquad \text{(A20)}$$

$$\pi^{-1} \int_a d\Omega \;=\; za^3(z^2 + a^2)^{-2} \qquad\qquad \text{(cylinder side wall)} \qquad \text{(A21)}$$

Equations (A19), (A20), and (A21) have been evaluated graphically in Fig. 3. The values of the parameters used in Fig. 3 are the ones that correspond to the cavity being supplied to AEDC under the terms of the present contract: $a = 0.1$ in. (2.54 mm); $R = 0.625$ in. (1.59 cm); $h = 1.242$ in. (3.15 cm). Note that z is the axial position variable.
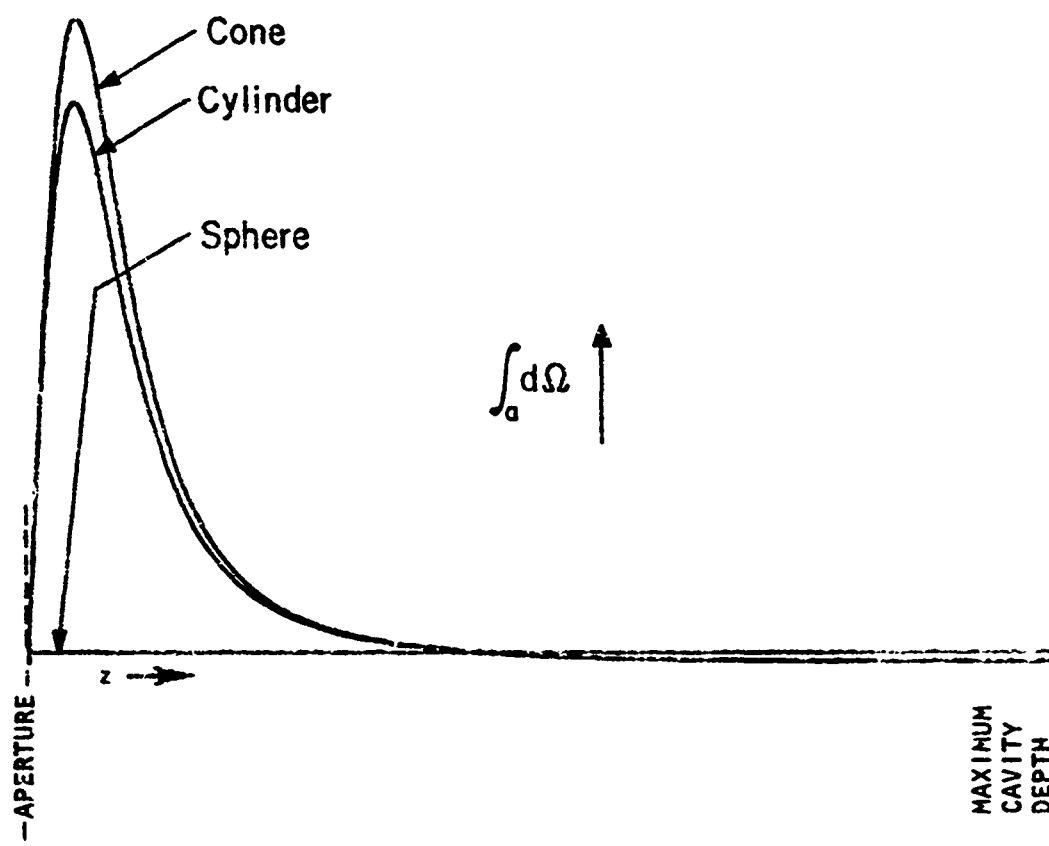
Fig. 3. Aperture Effects.

Figure 3 shows that cone and cylinder have very large values of $\int_a d\Omega_{10}$ near the cavity mouth and the sphere has a constant value of $\int_a d\Omega_{10}$ everywhere. The appearance of the curves in Fig. 3 is confirmed by an examination of Eqs. (A19), (A20), and (A21). No position variables appear in Eq. (A19), so it should be expected that the curve in Fig. 3 for the sphere would be a constant. Both Eq. (A20) and Eq. (A21) have a factor $z(z^2 + B^2)^{-2}$ where $B^2 = a^2$ or $B^2 = a^2(1 - z/h)^2$, so it should be expected that there would be zero values at $z = 0$ and then rather large values near $z = 0$; and this is indeed what Fig. 3 shows. Figure 3 and Eqs. (A20) and (A21) lead us to conclude that a cone or cylinder is a poor choice for our blackbody simulator cavity; Fig. 3 and Eq. (A19) show that a sphere is an excellent choice.

The theory that gives Eq. (1) is associated with the experimental arrangement of Fig. 4, which is the same as Fig. A1 of Appendix A. This experiment was performed on three cavity types of blackbody simulator: a sphere, a cone, and a cylinder. Each cavity was made from a 4-in. (10.16-cm) cube of aluminum. The sphere is illustrated in Fig. 5. All three cavities have four cartridge type heaters located as shown in Fig. 5. All three have the same cavity aperture diameter and cavity depth. All three were operated at the same temperature, 400°C. All three have aluminum cores with a cavity surface coating made of fine granulated quartz (sand) lightly bonded to the core with Aquadag (colloidal graphite in water) and Aerodag (an aerosol of micron-sized graphite in isopropyl alcohol). Aquadag and Aerodag are available from Acheson Colloids Company, Port Huron, Michigan. The coating provides a diffuse surface and increases the effective wall emissivity. The quartz is a relatively poor conductor of heat, so the coating allows thermal gradients to develop and thus prove or disprove the theory of Eq. (1) while
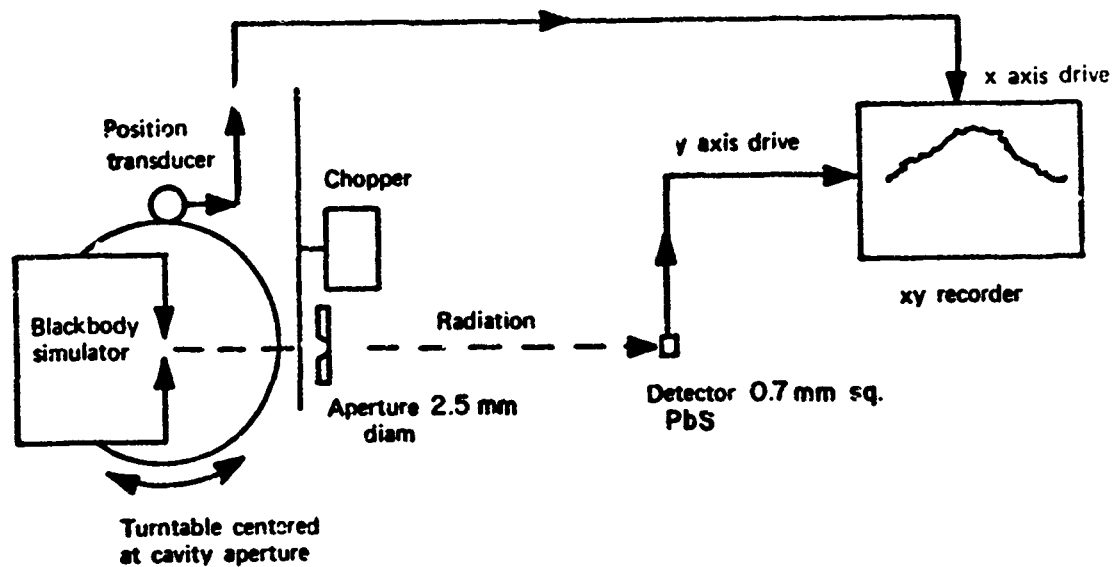
Fig. 4 . Experimental arrangement.
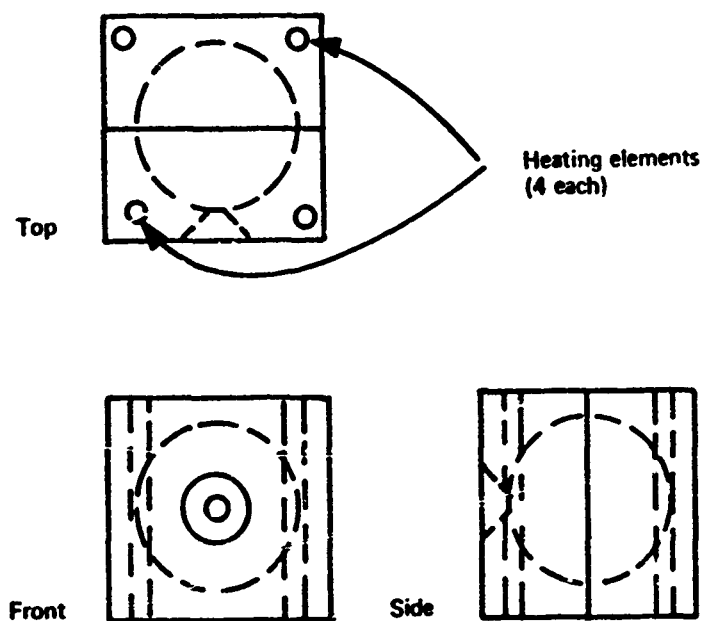
Fig. 5 . Spherical cavity blackbody simulator.

a simple aluminum cavity with its higher conductivity might mask the phenomena being investigated.

The experiment was designed to monitor the radiation emitted from different parts of the cavity surface as viewed by the detector through the aperture. Radiation from the sources was detected by a 0.7-mm-square lead sulfide detector. Readout was performed by a Princeton Applied Research (PAR) model HR-8 lock-in amplifier connected to a Hewlett-Packard-Moseley model 7000AM XY recorder. The tests were run by rotating the turntable (see Fig. 4), which was centered at the cavity aperture. The detector signal was connected to the Y axis of the plotter, and a rotation-sensing transducer was connected to the X axis. The plotter gains for both vertical and horizontal axes were adjusted for convenient displays, and the horizontal and vertical scales were marked from turntable and amplifier readings. Alignment was performed with a small helium-neon laser and was checked radiometrically through the final readout system.

Figure 3 gives $\int_a d\Omega$ for the geometry of the cavity delivered to AEDC. Figure 6 gives the same $\int_a d\Omega$ for the three cavities used in the experiment of Fig. 4: $a = 0.5$ in. (1.27 cm), $R = 3$ in. (7.62 cm), $h = 2.9$ 4 in. (7.40 cm), and z is the axial position variable measured from the cavity aperture. The results of the tests on the three cavities--sphere, cone, and cylinder--are given in Fig. 7. Several things may be predicted from the theory and verified by the plots of Fig. 7.

(1) Equations (A19), (A20), and (A21) and Fig. 6 predict that the radiometric signal from a spherical cavity should be much more uniform than that from a conical or cylindrical cavity, and this is verified by the experimental plots of Fig. 7. Total excursions between -50° and $+50^{\circ}$ for the three cavity shapes are: cone 8.3%, cylinder 6.3%, and sphere 1.5%.

Vertical line represents Z value corresponding to 50° position in Fig. 7
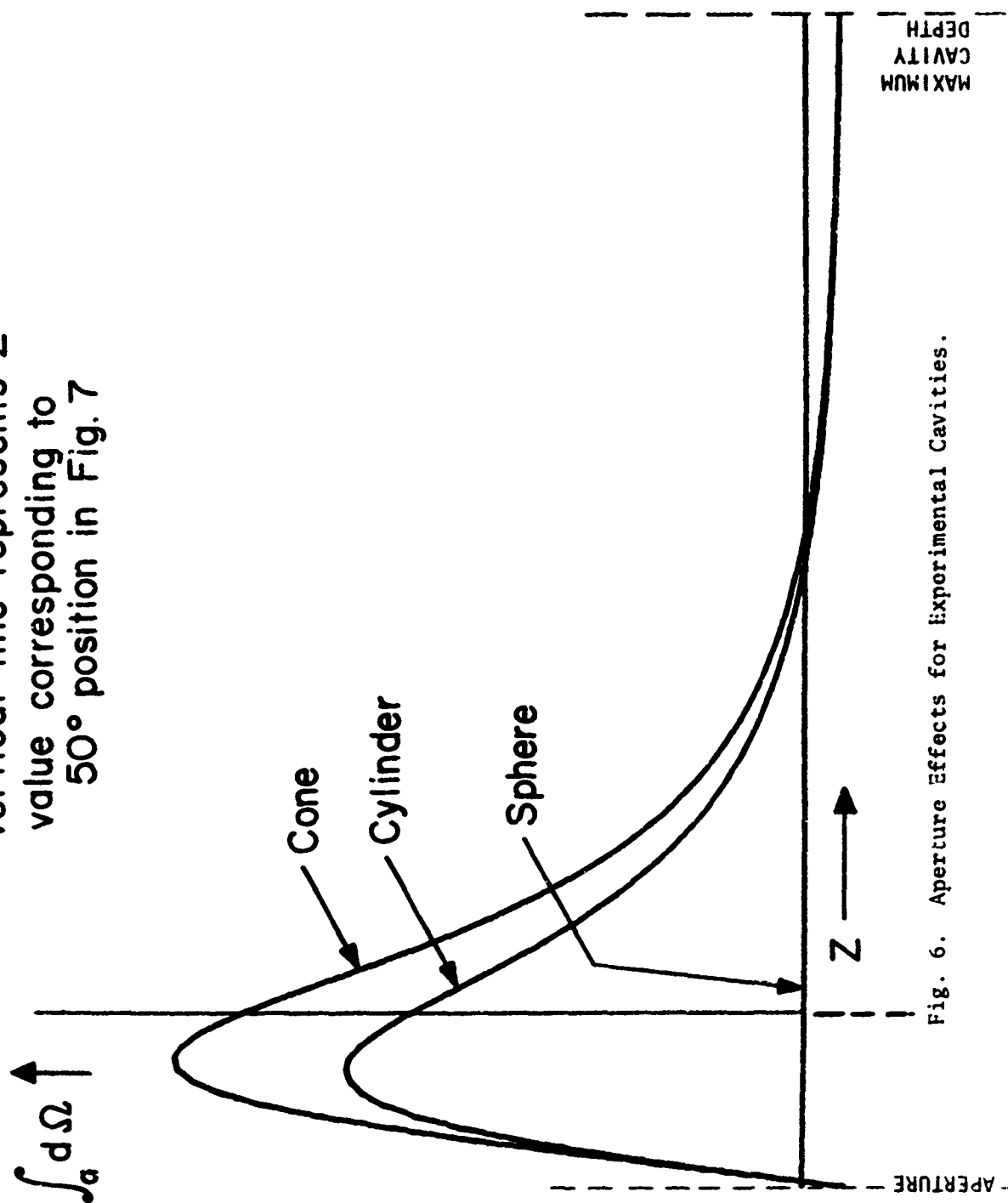
Fig. 6. Aperture Effects for Experimental Cavities.

Cone

100 %

4.2 mv

-8.0 %

-8.3 %

3.7 mv

-50° -40°   -20°   0°   20°   40° 50°

Cylinder

100 %

4.5 mv

-5.7 %

-6.3 %

4.1 mv

-50° -40°   -20°   0°   20°   40° 50°

Sphere

-1.5 %

4.5 mv

100%

4.2 m∕

-50° -40°   -20°   0°   20°   40° 50°
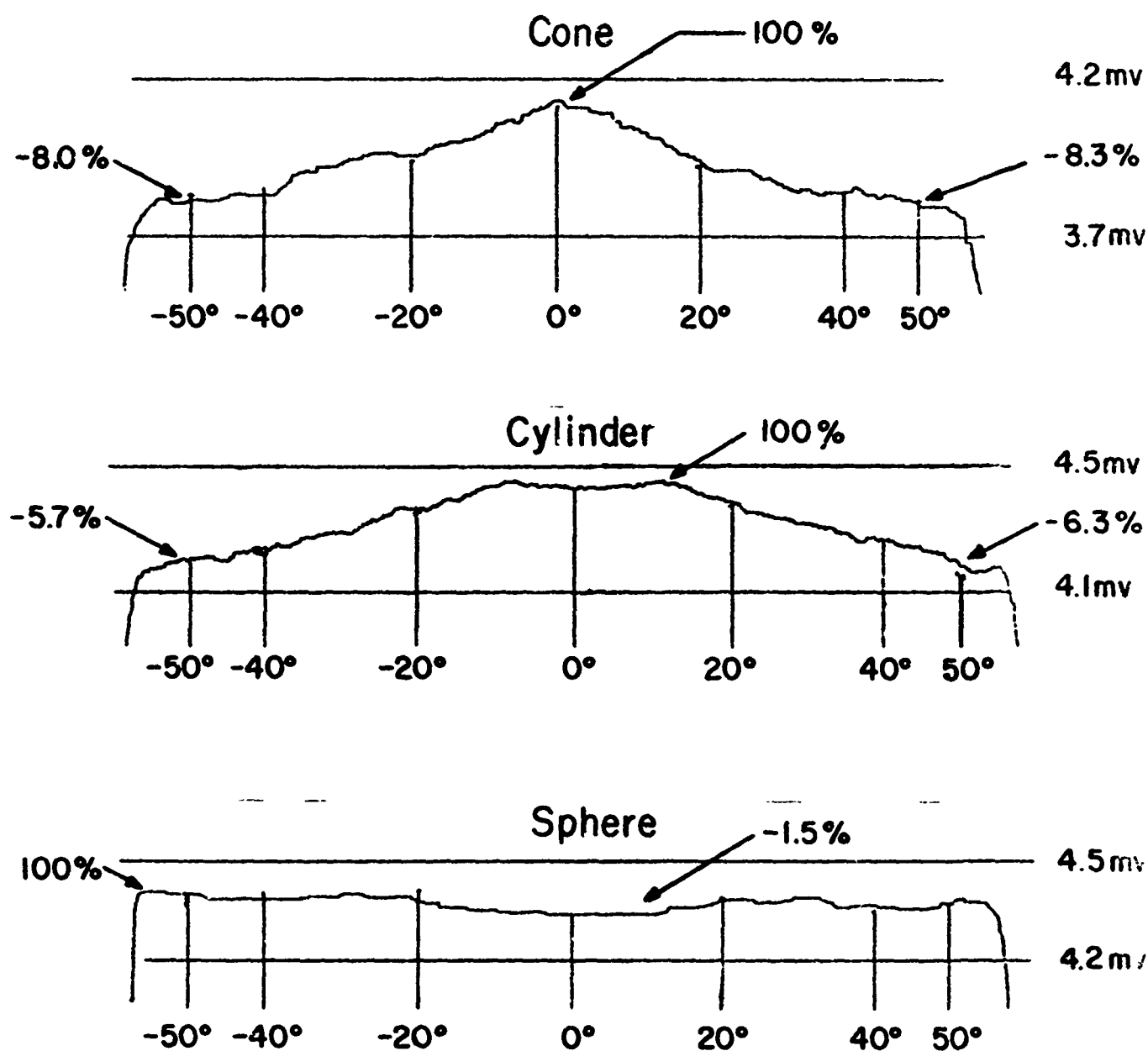
Fig. 7. Performance of Experimental Cavities.

(2) The *Handbook of Military Infrared Technology* has shown that conical cavities are preferred by blackbody simulator manufacturers, but Fig. 6 suggests that, among sphere, cone, or cylinder shapes, the cone may well be the worst. The experimental data of Fig. 7 verify that for uniform output the cone is indeed the worst.

(3) Equations (A21a) and (A22a) and Fig. A8 of Appendix A and their associated discussion suggest that tne highest radiometric signals from a cylindrical cavity probably come from points on the cylinder side wall near the back. The experimental arrangement for the data of Fig. 7 involved a cylinder with the side-back interface at an angle of 9.7^o. Thus the theory predicts a maximum signal for the cylinder plot of Fig. 7 at an angle close to but somewhat greater than 9.7^o. Figure 7 clearly shows two off-zero maxima nea $\pm10^o$.

(4) Figures 6 and 7 cannot be exactly compared because Fig. 6 plots aperture effects, $\int_a d\Omega$, as a function of cavity depth and Fig. 7 gives radiometric signal as a function of angle as seen from the center of the aperture. However, the $\pm50^o$ points of Fig. 7 can be located approximately on Fig. 6, and this has been done. Then we see the relative droops of cone, cylinder, and sphere at $\pm50^o$ are similar in the two figures.

Let us summarize the reasons that we have chosen a spherical-shaped cavity for the 7V IR Simulator application.

(1) Equation (1) shows that all geometrical effects for blackbody simulator cavities are manifest in the factor $\int_a d\Omega$, which is the projected solid angle of the aperture as seen from different points within the cavity. Then Eqs. (A19), (A20), and (A21) and Fig. 6 show

that, for the simple shapes of cone, cylinder, and sphere, only the sphere has a uniform value of $\int_a d\Omega$, whereas the cone and cylinder have large values of $\int_a d\Omega$ in the vicinity of the aperture. Thus the sphere will make a far more uniform and far more isothermal cavity for a blackbody simulator.

(2) Experimental data given in Fig. 7 verify several detailed points of the theory used here, and in particular Fig. 7 shows the far greater uniformity of output of the spherical cavity.

(3) It is shown in Section 2 of this report that radiometric processes tend to produce lower temperatures near cavity aperture for cones and cylinders but not for spheres. Furthermore, if temperature differences arise within spherical cavities, radiometric processes tend to equalize those temperatures, but for other cavity shapes depending on the variables ϕ_1, ϕ_2, and r (see page 14 for definitions of these variables), there may be a greater or lesser tendency for radiometric temperature equalization.

(4) In Section 3 of this report it is shown that the spherical configuration is the only one that will have uniform isotropic emittance across the entire aperture.

CAVITY TEMPERATURE UNIFORMITY

Our study has shown that a spherical cavity is the best shape for achieving uniform cavity temperature. This section of the report has three parts to describe temperature uniformity and its effects: (1) radiometric temperature equalization, (2) measurements of temperature uniformity, and (3) polythermal cavity effects.

(1) Radiometric Temperature Equalization

It may be shown that radiometric processes tend to equalize spherical cavity temperatures but may produce serious temperature differences within cavities of other shapes. In Section 1 of this report it was stated that the spherical shape has been selected for the blackbody simulator of the present contract. Therefore, the temperature equalization phenomenon just mentioned becomes an important factor for achieving uniform temperature for our cavity surface.

Radiometric temperature equalization of spherical cavities may be shown as follows: An analytic expression for energy or flux interaction can be developed from the flux-exchange equation (7.7) of M. A. Bramson (*Infrared Radiation*, Plenum Press, 1968, p. 214):

$$F = \sigma(T_1^4 - T_2^4) \int_{S_1} \int_{S_2} (\cos\phi_1 \cos\phi_2 / \pi r^2) \, ds_1 \, ds_2$$

where

F = the resultant flux from surface S_1 to surface S_2
σ = the Stefan-Boltzmann constant
T_1 = the temperature in K of surface S_1
T_2 = the temperature in K of surface S_2
ϕ_1 = the angle between the normal at ds_1 and the line from ds_1 to ds_2
ϕ_2 = the angle between the normal at ds_2 and the line from ds_1 to ds_2
r = the length of the line from ds_1 to ds_2.

14

If S_1 and S_2 are very small:

$$r \;\simeq\; \text{constant}$$

$$\varphi_1 \;\simeq\; \text{constant} \quad\Bigg\} \qquad \text{over} \;\; \int_{S_1}\!\int_{S_2} ds_1 ds_2$$

$$\varphi_2 \;\simeq\; \text{constant}$$

Then

$$F \;=\; \sigma(T_1^{\,4} - T_2^{\,4})\cos\varphi_1\cos\varphi_2 S_1 S_2/\pi r^2 \tag{2}$$

General Cavity Shape

Let us now express the last equation in terms of a geometry that is more useful for this analysis (see Fig. 8).

$\cos\varphi_2 = z/r$

$\varphi_1 = \psi_3 + u$

$\cos\varphi_1 = \cos\varphi_3 \cos u - \sin\varphi_3 \sin u$, where u is the off-axis tilt of the surface element ds_1,

but

$\cos\varphi_3 = y/r$

$\sin\varphi_3 = z/r$;
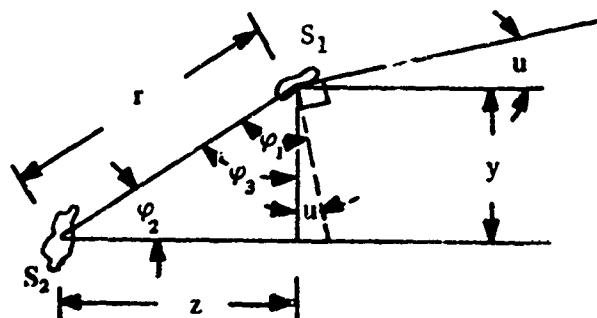
Figure 8 General cavity geometry

therefore

$\cos\varphi_1 = (y\cos u - z\sin u)/r$

and

$$F \;=\; \sigma(T_1^{\,4} - T_2^{\,4})(y\cos u - z\sin u)z S_1 S_2/\pi r^4 . \tag{3}$$

Spherical Cavity

Figure 9 shows

$$y = R\cos u$$

$$z = R(1 - \sin u)$$

Figure 9   Spherical cavity

By substituting into Eq. (3) we have

$$F = \sigma(T_1^4 - T_2^4)\left[(R\cos u)\cos u - R(1-\sin u)\sin u\right]zS_1S_2/\pi r^4$$

$$= \sigma(T_1^4 - T_2^4)R(\cos^2 u + \sin^2 u - \sin u)z S_1S_2/\pi r^4$$

$$= \sigma(T_1^4 - T_2^4)R(1 - \sin u)zS_1S_2/\pi r^4$$

$$= \sigma(T_1^4 - T_2^4)z^2 S_1S_2/\pi r^4.$$

However, in triangles ABC and ADO in Fig. 9,

$$z/r = (r/2)/R;$$

therefore

$$z^2/r^4 = 1/4R^2$$

and

$$F = \sigma(T_1^4 - T_2^4)S_1S_2/4\pi R^2 \qquad \text{(sphere)}. \qquad (4)$$

This equation gives the energy of flux exchange between any two small areas S_1 and S_2 at temperatures T_1 and T_2 on the inner surface of a spherical cavity. The important point in Eq. (4) is that it does not contain any of the position variables r, y, z, ϕ_1, ϕ_2, or u. Thus, any two small areas S_1 and S_2 at different temperatures on the cavity surface will have a net transfer of radiation proportional only to the difference of the fourth power of the temperatures, no matter where the two areas are located. In contrast to this situation for spherical cavities, other cavity shapes have energy exchange relationships that are not constant. When an analysis like that for Eq. (4) is performed for cones or cylinders, the effects of $\cos\phi_1$, $\cos\phi_2$, and r^2 in Eq. (2) are such that the radiant exchange between two areas S_1 and S_2 varies considerably as a function of position within the cavity. For example, consider S_1 near the apex of a conical cavity and S_2 near the aperture and located so that the line from S_2 to S_1 passes through the apex. For this case $\cos\phi_1 = \cos\phi_2 = 0$ in Eq. (2), so there is no radiant heat exchange even though one area is near the hottest point and the other is near the coldest point on the cavity surface.

In Section 1 it was shown, both theoretically and experimentally, that as the back walls of different cavities are scanned with narrow search beams, spherical cavities tend to give rather uniform radiometric signals but conical and cylindrical cavities tend to give signals that vary with position and have reduced values when the scan moves away from the axis down the side wall toward the aperture. Part of this effect is attributed to the third term in Eq. (1)--a varying cavity effect dependent on $\int_a d\Omega_{10}$, which is larger near the aperture for conical and cylindrical cavities. Another part of this effect (reduced signals from regions near cylinder or cone apertures) is attributed to the fourth term of Eq. (1)--a varying temperature loss that is also

dependent on $\int_a d\Omega_{10}$. In Section 1 both the third and fourth terms of Eq. (1) were considered, but here in Section 2 only the fourth term is studied, and it is noted that the constant $\int_a d\Omega_{10}$ of the sphere tends to result in uniform cavity temperatures whereas the varying $\int_a d\Omega_{10}$ of the cone and cylinder tend to result in cooler temperatures near the aperture.

This discussion of radiometric temperature equalization may be summarized as follows:

(a) $\int_a d\Omega_{10}$ is constant over the interior surfaces of spherical cavities, but varies over the surfaces of conical and cylindrical cavities with larger values near their apertures.

(b) Because of these properties of $\int_a d\Omega_{10}$, the fourth term of Eq. (1) indicates that there are radiometric processes that tend to lower temperatures near cylindrical and conical cavity apertures; but the radiometric processes do not tend to establish temperature differences for spherical cavities.

(c) If temperature differences arise within spherical cavities, radiometric processes tend to equalize those temperatures, but for other cavity shapes, depending on the variables ϕ_1, ϕ_2, and r, there may be greater or less tendency for radiometric temperature equalization.

(2) Measurements of Temperature Uniformity

There are two problems of temperature uniformity that are of concern in blackbody simulator design and fabrication. The first is temperature uniformity among points within the cavity. The second concerns the uniformity of temperature between points within the cavity and the point where the

temperature is measured for control and recording purposes. A series of measurements was performed to monitor both these types of temperature uniformity.

Figure 10 shows the experimental setup. The core design is like that of the blackbody simulator delivered to AEDC. The insulation and mounting details are also similar to the delivered unit. A twin-junction thermocouple circuit was used to measure temperature uniformity. One junction was located in a temperature-transducer well in the rear of the core simulating the platinum resistance thermometer used in the simulator delivered to AEDC. The other junction was inserted into the aperture of the spherical cavity and moved around to map the temperature distribution in the cavity. This second junction was also (1) brought to equilibrium at room temperature and (2) placed in liquid nitrogen. These two steps make it possible to establish thermocouple calibration and to measure blackbody simulator core temperature.

Chromel-constantan thermocouples with 0.005-in. and 0.010-in. diameter wires were employed. Difficulty was experienced in maintaining good thermal contact between the thermocouple junction and the cavity wall. This problem was solved by applying a small amount of Dow Corning 340 Silicone Heat Sink Compound to the junction. This material is available from Dow Corning Corporation, Hemlock, Michigan.

Readout was performed on a Data Precision Digital Multimeter Model 2540 A1. Excessive fluctuations were initially encountered, but, with greater care, variations were reduced to the range of about 0.01 K to 0.10 K. Experimental techniques that reduced the fluctuations included use of the Dow Corning Heat Sink Compound, waiting longer period for temperature equilibrium to be established, and support of the cavity-probe thermocouple junction by a laboratory fixture instead of by hand.
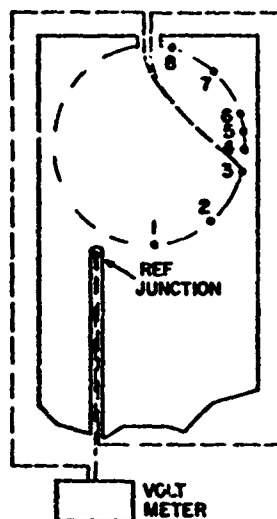
Fig. 10. Temperature Uniformity Test.

Typical test results are as follows (Table I). The numbered points associated with the temperature readings correspond to the numbered points on Fig. 10.

Table I. Cavity Temperature Data.

	533K	522K	522K	523K	607K	608K
1	+0.00	+0.00	+0.02	+0.03	+0.12	+0.01
2	+0.14	+0.08	+0.42	+0.14	+1.10	+0.62
3	+0.36	+0.36	+0.71	+0.25	+1.19	+1.14
4	--	+0.39	+0.88	+0.54	+1.15	+0.88
5	+0.34	--	--	+0.32	--	--
6	--	--	--	+0.23	--	+0.24
7	--	+0.01	-0.02	-0.48	+0.74	+0.11
8	-1.15	-1.06	-0.68	-1.79	+0.13	-0.64
Mean	+0.210	+0.168	+0.402	+0.147	+0.860	+0.500
Std. devia.	+0.149	+0.171	+0.360	+0.295	+0.403	+0.414

For all four data series in Table I from 522 K to 533 K the mean is 0.225 K and the standard deviation is 0.285 K. For both data series at 607 K and 608 K the mean is 0.664 K and the standard deviation is 0.447 K.

These data suggest that temperature measurement errors are less than 0.5 K at 500 K, and they are less than 1.0 K at 600 K. Note that the points labeled 8 in Fig. 10 and Table I were not included in the calculations for the mean and the standard deviation. These points (8) are anomalously low due to their proximity to the aperture, and the surface area represented by these points is small.

(3) Polythermal Cavity Effects

Parts (1) and (2) of this Section have shown that the selected design achieves temperature uniformities within ±1 K at 600 K and within ±0.5 K at 500 K and lower temperatures. We now consider the effects on blackbody simulator output of these small but finite temperature differences within the cavity.

The radiance from an ideal blackbody surface at some wavelength λ and some temperature T is $L_e(\lambda)$:

$$L_e(\lambda) = c_1 \lambda^{-5} \pi^{-1} [\exp(c_2/\lambda T) - 1]^{-1},$$

where c_1 and c_2 are the first and second radiation constants. If the surface is not ideal, but has an emissivity ϵ, then we might write

$$L_e(\lambda) = \epsilon c_1 \lambda^{-5} \pi^{-1} [\exp(c_2/\lambda T) - 1]^{-1}.$$

If the surface is the primary radiating surface of a blackbody simulator cavity, and if we make three assumptions

(1) Aperture effects may be neglected
(2) Only first-order reflections will be considered
(3) The cavity is isothermal

then

$$L_e(\lambda) = \epsilon c_1 \lambda^{-5} \pi^{-1} [\exp(c_2/\lambda T) - 1]^{-1} + (1-\epsilon) c_1 \lambda^{-5} \pi^{-1} [\exp(c_2/\lambda T) - 1]^{-1}.$$

Note that this equation reduces to the first expression of $L_e(\lambda)$. However, if we retain assumptions (1) and (2) but now consider a polythermal rather than an isothermal cavity, then

$$L_e(\lambda) = \epsilon c_1 \lambda^{-5} \pi^{-1} [\exp(c_2/\lambda T) - 1]^{-1} + (1-\epsilon) c_1 \lambda^{-5} \pi^{-1} [\exp(c_2/\lambda T_{ave}) - 1]^{-1},$$

where T_{ave} is some average temperature within the cavity. A more useful form of this equation can be obtained if we divide the cavity into n zones

with equal projected solid angles as seen from the primary radiating surface and assume that each zone (i) can be represented by an average temperature T_i for that ith zone. Then

$$L_e(\lambda) = \varepsilon c_1 \lambda^{-5} \pi^{-1} [\exp(c_2/\lambda T) - 1]^{-1}$$

$$+ (1-\varepsilon) c_1 \lambda^{-5} \pi^{-1} n^{-1} \sum_{i=1}^{n} [\exp(c_2/\lambda T_i) - 1]^{-1}. \qquad (5)$$

The purpose of the present analysis is to calculate the effects, in terms of radiance $L_e(\lambda)$, of the small but finite temperature differences within the cavity. Comparing Eq. (5) with Fig. 10, we see that the equation would agree with the experimental arrangement of the figure if the value of T, the temperature of the primary radiating surface, were known. That temperature is indeed known for the experiment described by Fig. 10, but it is not generally known for an operating blackbody simulator; rather, the temperature that is known in an operating system is the temperature in a temperature measurement well like that labeled "ref. junction" in Fig. 10. Suppose the difference between the measured temperature in the temperature measurement well and the temperature of the primary radiating surface is T_{gap}, where T_{gap} is defined by

$$T = T_{measured} + T_{gap}, \qquad (6)$$

then the actual $L_e(\lambda)$ is that given by Eqs. (5) and (6), but the common and incorrect interpretation of the arrangement of Fig. 10 assumes an isothermal cavity at temperature $T_{measured}$ and a nearly perfect emissivity ($\varepsilon = 1.00$):

$$L_e(\lambda)_{incorrect} = c_1 \lambda^{-5} \pi^{-1} [\exp(c_2/\lambda T_{measured}) - 1]^{-1}. \qquad (7)$$

The difference between the values of L_e given by Eqs. (5) and (7) is one expression of polythermal cavity effects. A convenient percentage expression is PCT, given by

$$PCT = (100\%) (L_e(\lambda)_{incorrect} - L_e(\lambda)) / L_e(\lambda).$$

A computer program has been written for PCT, and the results are tabulated in Table II. The quantities T, ϵ, T_{gap}, and . in this table are identified on the previous two pages; ΔT is the total temperature range within the cavity.

Table II should be interpreted in conjunction with several other parts of this report. The subsection entitled "Temperature Range" in Section 5 (pp. 43-44) suggests avoidance of T values below 200 K. Appendix C4 gives ϵ values of 0.9 or higher except between 3.0 μm and 7.0 μm, where values may be as low as 0.71. Table I on page 21 suggests that T_{gap} values at 500 K are below 0.1 K. Table I also suggests that ΔT values at 500 K are about 0.5 K or less (if we neglect point 8, which may be considered anomalously low owing to its proximity to the aperture--this approximation is consistent with Eq. (5) and with the way Table II was computed). At 300 K and 200 K we should expect ΔT values to be even smaller. When all these considerations are combined, we see that the data in Table II that apply best to the Improved Blackbody Simulator are those entries enclosed in the boxes. Note that all such entries are 0.51% or less.

Table II. Polythermal Cavity Effects (%).

T (K)	ϵ	T_{gap} (K)	ΔT (K)	λ (μm)								
				2	3	4	5	6	7	8	16	32
100	0.9	0.0	0.2	0.68	0.44	0.33	0.26	0.22	0.19	0.16	0.08	0.04
			0.5	1.81	1.16	0.85	0.68	0.56	0.48	0.42	0.20	0.10
			1.0	4.09	2.51	1.81	1.41	1.16	0.98	0.85	0.41	0.21
		0.1	0.2	8.18	5.37	4.00	3.19	2.65	2.27	1.98	0.98	0.50
			0.5	9.40	6.12	4.54	3.61	3.00	2.56	2.23	1.11	0.56
			1.0	11.83	7.53	5.53	4.37	3.61	3.07	2.68	1.32	0.66
		0.2	0.2	16.22	10.53	7.80	6.19	5.13	4.38	3.82	1.89	0.95
			0.5	17.53	11.32	8.36	6.62	5.49	4.68	4.08	2.02	1.02
			1.0	20.13	12.79	9.38	7.40	6.11	5.21	4.53	2.23	1.12
	0.75	0.0	0.2	1.69	1.11	0.83	0.66	0.55	0.47	0.41	0.20	0.10
			0.5	4.53	2.90	2.14	1.69	1.40	1.19	1.04	0.51	0.26
			1.0	10.21	6.27	4.52	3.53	2.89	2.45	2.13	1.03	0.52
		0.1	0.2	9.27	6.07	4.51	3.59	2.98	2.55	2.23	1.11	0.56
			0.5	12.31	7.95	5.87	4.65	3.85	3.29	2.87	1.42	0.71
			1.0	18.40	11.47	8.33	6.54	5.38	4.57	3.98	1.94	0.97
		0.2	0.2	17.39	11.26	9.33	6.61	5.47	4.67	4.08	2.02	1.01
			0.5	20.65	13.23	9.73	7.69	6.36	5.42	4.73	2.33	1.17
			1.0	27.17	16.91	12.28	9.63	7.93	6.73	5.86	2.86	1.43
200	0.9	0.0	0.2	0.16	0.11	0.08	0.07	0.05	0.05	0.04	0.02	0.01
			0.5	0.42	0.27	0.20	0.16	0.14	0.12	0.10	0.05	0.03
			1.0	0.85	0.56	0.42	0.33	0.27	0.23	0.20	0.10	0.06
		0.1	0.2	1.98	1.32	0.98	0.79	0.66	0.56	0.49	0.25	0.14
			0.5	2.24	1.48	1.10	0.89	0.74	0.63	0.55	0.28	0.15
			1.0	2.68	1.77	1.32	1.05	0.88	0.75	0.65	0.33	0.18
		0.2	0.2	3.83	2.54	1.90	1.51	1.26	1.08	0.94	0.48	0.26
			0.5	4.09	2.71	2.02	1.61	1.34	1.15	1.00	0.51	0.28
			1.0	4.54	3.00	2.23	1.78	1.48	1.27	1.11	0.56	0.31
	0.75	0.0	0.2	0.41	0.27	0.20	0.16	0.13	0.12	0.10	0.05	0.03
			0.5	1.04	0.69	0.51	0.41	0.34	0.29	0.25	0.13	0.07
			1.0	2.14	1.40	1.04	0.83	0.69	0.59	0.51	0.26	0.14
		0.1	0.2	2.23	1.48	1.11	0.89	0.74	0.63	0.55	0.28	0.15
			0.5	2.87	1.90	1.42	1.13	0.94	0.81	0.71	0.36	0.20
			1.0	3.99	2.62	1.95	1.55	1.29	1.10	0.96	0.48	0.27
		0.2	0.2	4.08	2.70	2.02	1.61	1.34	1.15	1.00	0.57	0.28
			0.5	4.73	3.13	2.33	1.86	1.55	1.33	1.15	0.58	0.32
			1.0	5.89	3.85	2.87	2.28	1.90	1.62	1.42	0.71	0.39

(Continued)

Table II (Continued)

T (K)	ε	T_{gap} (K)	ΔT (K)	λ (μm)								
				2	3	4	5	6	7	8	16	32
300	0.9	0.0	0.2	0.07	0.05	0.04	0.03	0.02	0.02	0.02	0.01	0.01
			0.5	0.18	0.12	0.09	0.07	0.06	0.05	0.05	0.02	0.01
			1.0	0.36	0.24	0.18	0.15	0.12	0.10	0.09	0.05	0.03
		0.1	0.2	0.88	0.58	0.44	0.35	0.29	0.25	0.22	0.11	0.07
			0.5	0.99	0.66	0.49	0.39	0.33	0.28	0.25	0.13	0.08
			1.0	1.17	0.78	0.58	0.47	0.39	0.33	0.29	0.15	0.09
		0.2	0.2	1.68	1.12	0.84	0.67	0.56	0.48	0.42	0.22	0.13
			0.5	1.80	1.19	0.89	0.71	0.59	0.51	0.45	0.23	0.14
			1.0	1.98	1.32	0.98	0.79	0.66	0.56	0.49	0.26	0.16
	0.75	0.0	0.2	0.18	0.12	0.09	0.07	0.06	0.05	0.05	0.02	0.01
			0.5	0.46	0.30	0.23	0.18	0.15	0.13	0.11	0.06	0.04
			1.0	0.92	0.61	0.45	0.36	0.30	0.26	0.23	0.12	0.07
		0.1	0.2	0.98	0.65	0.49	0.39	0.32	0.28	0.25	0.13	0.08
			0.5	1.26	0.84	0.63	0.50	0.42	0.36	0.31	0.16	0.10
			1.0	1.73	1.15	0.86	0.68	0.57	0.49	0.43	0.22	0.14
		0.2	0.2	1.79	1.19	0.89	0.71	0.59	0.51	0.45	0.23	0.14
			0.5	2.07	1.38	1.03	0.82	0.69	0.59	0.51	0.27	0.16
			1.0	2.54	1.68	1.26	1.01	0.84	0.72	0.63	0.33	0.20
500	0.9	0.0	0.2	0.03	0.02	0.01	0.01	0.01	0.01	0.01	0.00	0.00
			0.5	0.07	0.04	0.03	0.03	0.02	0.02	0.02	0.01	0.01
			1.0	0.13	0.09	0.07	0.05	0.04	0.04	0.03	0.02	0.01
		0.1	0.2	0.31	0.21	0.16	0.13	0.11	0.09	0.08	0.05	0.03
			0.5	0.35	0.24	0.18	0.14	0.12	0.10	0.09	0.05	0.04
			1.0	0.42	0.28	0.21	0.17	0.14	0.12	0.11	0.06	0.04
		0.2	0.2	0.60	0.40	.30	0.24	0.20	0.17	0.15	0.09	0.06
			0.5	0.64	0.43	0.32	0.26	0.22	0.19	0.16	0.10	0.07
			1.0	0.71	0.47	0.35	0.28	0.24	0.20	0.18	0.10	0.07
	0.75	0.0	0.2	0.06	0.04	0.03	0.03	0.02	0.02	0.02	0.01	0.01
			0.5	0.16	0.11	0.08	0.07	0.05	0.05	0.04	0.02	0.02
			1.0	0.33	0.22	0.16	0.13	0.11	0.09	0.08	0.05	0.03
		0.1	0.2	0.35	0.24	0.18	0.14	0.12	0.10	0.09	0.05	0.04
			0.5	0.45	0.30	0.23	0.18	0.15	0.13	0.12	0.07	0.05
			1.0	0.62	0.41	0.31	0.25	0.21	0.18	0.16	0.09	0.06
		0.2	0.2	0.64	0.43	0.32	0.26	0.22	0.19	0.16	0.10	0.07
			0.5	0.74	0.49	0.37	0.30	0.25	0.21	0.19	0.11	0.08
			1.0	0.90	0.60	0.45	0.36	0.30	0.26	0.23	0.13	0.09

SECTION 3

CAVITY EMITTANCE UNIFORMITY

Our study has shown that a spherical cavity is the best shape for
achieving uniform cavity emittance. Emittance or radiant emittance is the
radiant flux density leaving a surface. F. E. Nicodemus (Appl. Opt. 7(7):
1359-1362, June 1968) gives, on p. 1361, the following:

> Incidentally, the note just after Eq. (5) suggests that the spherical
> cavity configuration is the only one that can achieve Lambertian ra-
> diation from its entire aperture (if the problem of heating the walls
> uniformly to achieve a truly isothermal condition can be solved).
> Even if the walls themselves are ideally Lambertian, as assumed in
> this analysis, and, further, if their reflectance is so low that all
> but the first two terms in Eq. (3) may be neglected, N_w will still
> vary with position, because of variations in N_{r1} if there are varia-
> tions in Ω'_w for the different elements dA that originate the rays
> passing through the aperture. It seems clear that departures from
> these ideal conditions can only add to the deviations from that uni-
> form N_w (for all wall elements) that is necessary for uniform and
> isotropic N_a at the cavity aperture.

Equation (5) referred to above gives N_{r1} (the reflected radiance con-
tributed by thermal emission from the cavity walls after no intermediate re-
flections from the walls) as being proportional to Ω'_w (the projected solid
angle subtended at the primary emitting point by the cavity walls). The dis-
cussion following Eq. (5) includes the statement: "A spherical cavity, how-
ever, has the convenient and probably unique property that Ω'_w is the same
at every position of dA...; so, for this case, N_{r1} is the same for all dA.'

This last statement is similar to our discussion in Sec. 1 that $\int_a d\Omega$
is a constant for a spherical cavity.

The above discussion shows that the best way to achieve uniform emit-
tance over the cavity aperture is to employ a spherical cavity. Because of
the importance of the Nicodemus paper (Applied Optics, 1968) to this section
of this report, it is reproduced here as Appendix B.

27

SECTION 4

CAVITY WALL EMITTANCE

Our study has shown that the best choices for wall and coating can be achieved by using aluminum, type 6061-T6, for the core material and then using the Hardas treatment, a commercial hard black anodic g process, for the wall surface coating.

The study of cavity wall emittance has been a combined study of the properties of core materials, the properties of coatings, and the properties of core-coating bonding.

Preliminary Study

A preliminary study was conducted in three phases.

Phase I of the preliminary study concerned selection of a core material. A blackbody simulator for standards use must have a cavity that is as nearly isothermal as possible. With this in mind, a review of the thermal conductivity of various materials showed that the search for a core material should be limited to metals plus graphite. (See Appendix C1.)

Phase II of the preliminary study concerned possible coatings plus core-coating bondings. The blackbody simulator is to operate from 100 K to 600 K in a 20 K environment. This requirement placed extremely severe strains on core-coating bondings in the form of differential thermal expansion. This argument suggested coatings of metal oxides for metal cores or just the graphite itself for graphite cores.

Phase III of the preliminary study was a re-examination of the entire core, coating, and bonding problem for metals and their oxides plus graphite. Three core candidates arose from this re-examination: aluminum, copper, and steel. The candidate coatings were different forms of the oxides of each

28

metal. Aluminum was selected as a candidate because of its high thermal
conductivity and its hard oxide coating. (See Appendix C2.) Copper was
selected as a candidate because of its high conductivity and because of
reports that copper could be oxidized to form a hard black cupric oxide
coating. Steel was selected as a candidate because of its high temperature
capabilities and because previous experience indicated that an adherent
coating of oxides could be formed on the surface of steel. Since the ther-
mal conductivity of steel is much smaller than that of copper or aluminum,
it was the third choice among the three remaining candidate metals.
Graphite was eliminated because of its low tensile strength. (See Appen-
dix C3.)

First Series of Tests

The first tests involved temperature cycling of aluminum substrates
with black anodized coatings. This material was selected for two reasons:
(1) This combination of core and coating materials was one of the most
promising candidates because of the good thermal conductivity of aluminum
and the excellent properties of both the coating and the bonding of the coat-
ing to the core. (2) Previous work had been done at the Optical Sciences
Center under Air Force contract F44620-69-C-0024 for using interferometric
test techniques for polished Al_2O_3 coatings on aluminum substrates. It
was recognized that this technique required removal of the upper layers of
the anodized coating by the polishing process, so only the lower layers of
the coating would be tested but this was done nevertheless because the
technique provided positive, rapid, and very accurate data on important
effects of temperature cycling. This test presented the remarkable oppor-
tunity of making measurements with an accuracy of a fraction of a wavelength

of visible light for coatings that in their original form have surface
irregularities with dimensions from about a wavelength of visible light
to hundre   ¬f wavelengths of visible light.

These first tests gave very valuable results, as follows:

--Cooling to 77 K in liquid nitrogen caused only slight deteriora-
tion in the interference fringe pattern. This favorable result occurred
in spite of abrupt thermal shocks when the samples were immersed in the
liquid nitrogen.

--Cooling to about 20 K with liquid helium gave about the same ef-
fects as cooling to 77 K with liquid nitrogen.

--Heating to 670 K caused considerable changes in the interference
fringe patterns. In some cases no fringe patterns could be seen.

--Rapid temperature increases (room temperature to 670 K in 25 min)
caused greater changes in the surface than slower temperature increases
(room temperature to 670 K in 115 min).

--Some samples with rapid temperature increases to 670 K showed
surface effects similar to the well-known "orange peel" phenomenon of glass
polishing. (Orange peel is a surface irregularity that appears to the eye
somewhat like orange peel.) Some samples under these conditions exhibited
a web of fine lines that looked like cracks in the surface layer. The
spacing of these "cracks" was about 0.25 mm apart.

--There was no indication of any separation of the coating from the
base material in any of the tests.

It was concluded from the first tests that:

--Surface deterioration at high temperature (600 K) would probably be
a more serious problem for our project than surface deterioration at low
temperature (20 K or 100 K).

--Rapid temperature changes should be avoided for Al_2O_3 coatings on aluminum.

Second Series of Tests

The second series of tests included (1) a study of different methods of preparing black oxide coatings on aluminum, copper, and steel, (2) heating samples to 600 K in both an unsealed laboratory oven and a vacuum bell jar arrangement, and (3) spectral reflectivity measurements from 3 to 15 μm wavelength with a Perkin-Elmer model 137 spectrometer. Steel and copper were eliminated during this series of tests.

Steel was eliminated because its thermal conductivity is from 1/3 to 1/10 that of aluminum (see Appendix C1) and the best oxide coatings prepared were no better than those of aluminum in both physical and optical properties.

Copper was eliminated because none of the copper coatings showed satisfactory adherence to the base metal after being heated to 600 K for several hours. Among the surfaces tested were (1) coated samples supplied by vendors, (2) samples prepared from commercial blackening solutions, and (3) samples prepared by electrolysis. Some of these coatings exhibited good physical and optical properties, but they all suffered separation from the base metal at 600 K. For reasons described in Section 5 of this report, it is recommended that the blackbody simulator be operated only from 200 K to 500 K even though it has been built for operation over the 100 K to 600 K range. If the upper temperature value had been 500 K instead of 600 K, copper and cupric oxide might have been selected for the core and coating. There should be special interest in copper as a core material for blackbody simulators because copper has 1.5 times the thermal conductivity of aluminum. However, the failure at 600 K occurred for every copper

sample, so no further testing was performed to determine the suitability of this material for operations at lower temperature..

At the end of the second series of tests, the choice of core material was reduced to the various alloys of aluminum and the choice of coating was limited to different processes involving Al_2O_3.

Third Series of Tests

The third series of tests was like the second except that the materials were limited to aluminum and aluminum coatings.

Among the alloys studied were 6061, 7075, 505C, 3003, and 1100.

Among the coatings studied were the following:

--Hardas, a hard black anodizing process available from

> Anadite, Inc.
> P.O. Box 92078
> Worldway Postal Center
> Los Angeles, California 90009
>
> 213-773-4210

--Aluma Black, a commercial solution used to treat aluminum, which is available from

> Birchwood Casey
> 7900 Fuller Road
> Eden Prairie, Minn. 55343
>
> 612-941-1240

--Martin Black, a special black anodizing process available from

> Martin Marietta Corporation
> Attn: Mr. Jack Wade
> P.O. Box 179
> Denver, Colorado 80201
>
> 303-794-5211

--A..C Black, a special type of black anodizing process, information on which may be obtained from

ARO Inc. AEDC
Attn: Mr. Fred Sherrell
    VKF-ASI
Arnold Air Force Station, Tenn. 37389
615-455-2611

--Kalcolor, a hard black anodizing process, information on which can
be obtained from

Kaiser Center Building
Attn: Mr. Ferd A. Loebach
300 Lakeside Drive
Oakland, Calif. 94612
415-271-3001

In this third series of tests Kalcolor and AEDC-Black were eliminated.

The Kalcolor process forms a hard black anodized coating much like that
of the Hardas process. Preliminary test results for Kalcolor were similar
to and slightly inferior to Hardas results. Furthermore, the Hardas process
by Anadite, Inc., is available in Tucson whereas Kalcolor is not, so it was
decided to continue the study with Hardas and drop Kalcolor.

The AEDC-Black process was described by the suppliers as being similar
to the Martin-Black process. When both AEDC-Black samples and Martin-Black
samples were heated to 600 K in air and in vacuum, the AEDC-Black samples
bleached to a whitish-gray color about the shade of untreated aluminum
and the Martin-Black samples experienced far less color change; some became
brown and some remained black. For this reason, plus a reluctance to
select an almost (visual) white surface for the blackbody cavity, it was de-
cided to continue testing with the Martin-Black but to stop tests with the
AEDC-Black.

In the previous subsection, Second Series of Tests, it is noted that,
if the temperature range had been 200 K to 500 K instead of 100 K to 600 K,

copper and cupric oxide might have been selected. Similarly, if the temperature range had been 200 K to 500 K, AEDC-Black might have been selected. Among the desirable features of AEDC-Black (compared to Martin-Black) are the fact that its surface finish is harder than that of Martin-Black and the fact that its spectral emissivity (before heating to 600 K) is above 0.9 from 3 μm to 15 μm whereas Martin-Black dips to 0.82 near 5 μm. Still more information became available following the fourth and last series of tests that indicated that the AEDC-Black should be considered an important candidate in any future testing program: Among the three blacks--Hardas, Martin, and AEDC--the spectral emissivity data of the Martin and Hardas processes are the two most similar. If this had been known earlier, there might have been a Martin-Hardas comparison, resulting in a halt to Martin tests instead of a Martin-AEDC comparison resulting in a halt to AEDC tests.

Fourth Series of Tests

This final series of tests involved Hardas, Aluma-Black, and Martin-Black.

Hardas blanks were prepared on 6061-T6 and 7075-T6 aluminum; they were anodized with a dc process and an ac-dc process; they were heated to 600 K in air and in vacuum; they were tested on the Perkin-Elmer (P-E) Model 137 spectrometer for reflectivity; and finally they were given spectral emissivity measurements at the following facilities.

> TRW Systems Group
> TRW, Inc.
> One Space Park
> Redondo Beach, California 90278
>
> Attn: E. E. Luedke, Head
> Thermophysics Section

Naval Electronics Laboratory Center
Electronic Materials Sciences Division
San Diego, California 92152

Attn: Dr. Donald L. Stierwalt
Code 2600

The best Hardas results were obtained with 6061-T6 aluminum using an equal ac-dc current mode.

Aluma-Black samples were prepared on 6061-T6 and 7075-T6 aluminum; they were made with a wide variety of processing and washing baths; they were heated to 600 K in air and in vacuum; they were tested on the P-E model 137 spectrometer for reflectivity; and finally they were given a spectral emissivity measurement at the TRW facility. The best Aluma-Black results were obtained by (1) preparing the surface by sandblasting immediately before the water and chemical treatment, (2) using three immersions of 60 sec each in Aluma-Black solution, and (3) using distilled water wash baths before, between, and after the immersions in the Aluma-Black solution.

Martin-Black samples were prepared on 6061-T6 and 7075-T6 aluminum; they were heated to 600 K in air and in vacuum; they were tested on the P-E 137 spectrometer; and finally they were given spectral emmisivity measurements at the TRW facility.

The spectral emissivity measurements are given in Appendix C4.

Martin-Black was dropped as a candidate early in the fourth series of tests, and extensive testing continued with Hardas and Aluma-Black. Martin-Black has remarkably high emissivity values over broad spectral ranges, but it has a dip to 0.82 near 5 μm that is comparable to Hardas. The Martin-Black surface is soft and cannot be touched whereas Hardas has a strong, hard surface. Furthermore, the Martin-Black samples suffered some discoloration at 600 K whereas Hardas did not, so Martin-Black testing was stopped.

The final comparison was between Hardas and Aluma-Black. Clearly, the Aluma-Black has a better spectral emissivity curve than Hardas. The Aluma-Black graph is over 0.88 from 2 um to over 20 µm whereas the Hardas dips to 0.71 near 5 µm. However, the harder, stronger Hardas surface was finally selected on the basis of superior reliability. Hardas surfaces are hard, and they can be handled without damage whereas Aluma-Black surfaces leave black dust on one's fingers when they are handled. Furthermore, Hardas surfaces were least affected by heating to 600 K of all the surfaces tested whereas Aluma-Black surfaces experienced slight color changes.

Two types of calculations were performed to verify that the reduced wall emissivity values near 5.0 µm would not compromise the performance of the blackbody simulator: (1) Effective cavity emissivity values were determined (see Appendix C5) and tabulated in Table III. (2) Special computer runs were made (Section 2(3)), and the results are tabulated in Table II. Table III shows that the effective cavity emissivity is more than .999 except between 3 µm and 7 µm, and it is more than .997 everywhere. Table II shows that, in the 3 µm to 7 µm region where the Hardas emissivity is less than 0.9, errors in spectral radiant output are about 0.5% or less.

Table III. Wall Effects
on Cavity Emissivity.

Wall emissivity	Effective cavity emissivity
1.0	1.0
0.95	0.999 663
0.90	0.999 289
0.85	0.998 872
0.80	0.998 402
0.75	0.997 871
0.70	0.997 265

SECTION 5

TEMPERATURE MEASUREMENT AND CONTROL

Our study has shown that the best method of providing temperature mea-
surement and control for the Improved Blackbody Simulator is with four-
terminal platinum resistance-thermometer temperature indicators and an
Artronix Model 5301-E temperature controller.

Temperature Transducers

Among the temperature transducers considered were resistance thermom-
eters, thermocouples, and silicon diodes.

Platinum resistance thermometers (PRT's) were selected because they
have the best absolute accuracy in the 100 K to 600 K region. In fact, the
International Practical Temperature Scale (IPTS) is defined, in this region,
in terms of a PRT. These devices come in two-, three- and four-wire config-
urations. Four-wire arrangements eliminate lead-resistance effects, so
this design was chosen. A drive current is supplied to two leads and the
voltage drop across the resistive element alone is monitored with the other
two leads. Calculations of heat losses through the PRT leads showed that
they are very small compared to other heat transfer quantities, so the prob-
lem of heat losses through the extra leads is outweighed by the improved
accuracy that a four-wire arrangement provides. Rosemount, Inc., was se-
lected as the supplier for the PRT's:

> Rosemount, Inc.
> P. O. Box 35129
> Minneapolis, Minn. 55435
> 612-941-5560

PRT's for blackbody simulator use are often small, delicate devices subjected to severe thermal shocks, and differential thermal expansion can result in strained or open resistance elements. To minimize the risk of PRT failure, the Improved Blackbody Simulator delivered to AEDC has been provided with three sensors.

Thermocouples (TC's) were also considered, but were not used because of the superior absolute accuracy of PRT's. Among the different types of TC's available, Type E, chromel-constantan, is recommended as best for the 100 K to 600 K region. Although PRT's are better than TC's for controlling the improved blackbody simulator, an important type of measurement can be better done with TC's than PRT's: that is the case where accurate values of small temperature differences are needed rather than the measurement of a single temperature with required absolute accuracy. An example of a case where accurate values of small temperature differences were needed is given in Section 2(2) of this report, where thermocouples were used to measure temperature differences in a blackbody simulator cavity.

Further information on PRT's and TC's and their use in the 100 K to 600 K region may be obtained from

> National Bureau of Standards
> Cryogenic Division
> Boulder, Colorado 80302
> Attn: Larry L. Sparks
> 303-499-1000

Silicon diode temperature transducers were also considered. They provide excellent performance at low temperatures, but they cannot be used above 400 K. Future problems involving temperatures no higher than 400 K might be handled with these devices. For more information about silicon diode

temperature transducers and temperature controllers based on them, contact

Lake Shore Cryotronics, Inc.
9631 Sandrock Road
Eden, New York   14057

Attn: Mr. David L. Swartz

716-992-3411

Temperature Controller

Temperature controllers that operate at low temperatures have special problems. Among these problems, for PRT type controllers, is the requirement that the joule heating in the PRT's be properly handled so that the control circuits are not upset. One way to solve this problem is to use very small currents in the PRT's.

More than 170 suppliers of temperature controllers were contacted for equipment to operate with the Improved Blackbody Simulator. Four sources of such equipment were considered to have special advantages for our use, and the Artronix 5301-E controller was selected as best for our application. Features of the Artronix 5301-E as applied to the Improved Blackbody Simulator are as follows:

--Low heat dissipation (maximum is 10^{-6} W) in the PRT

--DC operation with the PRT, so the NBS traceable calibration of the PRT is applicable

--Rate and reset features

--Temperature deviation meter

--Possible operation with PRT's, TC's, and silicon diodes

Artronix also supplies the 5301-U temperature controller. This unit is somewhat similar to the 5301-E, but it operates in an ac mode. It may

provide more accurate temperature control than the 5301-E. It was not selected, however, because it lacks the multimode capability of the 5301-E (resistive sensors and thermocouples), and its ac operation sacrifices the NBS traceable calibration of the PRT.

More information on the Artronix 5301-E and 5301-U controllers may be obtained from

> Artronix, Inc.
> 716 Hanley Industrial Court
> St. Louis, Missouri 63144
> 314-644-2456

A second vendor that was considered is Lake Shore Cryotronics, Inc. Their equipment was not purchased because some development effort would have been required to adapt to our problem. More information about Lake Shore Cryotronics, Inc., controllers can be obtained from the address given on page 39.

Andonian Cryogenics, Inc., was also considered. They were not selected because of required development effort. More information about Andonian Cryogenics, Inc., control systems may be obtained from

> Andonian Cryogenics, Inc.
> 26 Farwell Street
> Newtonville, Mass. 02160
> 617-969-8010

The last alternative supplier of the temperature controller is the University of Arizona. Our preliminary designs suggested a control unit that would be tailored to the Improved Blackbody Simulator and might be as good as or better than one we could buy; but the necessary development effort in both cost and lead time were such that the Artronix 5301-E unit was selected instead.

Temperature Measurement

Measurements of temperature uniformity within the blackbody simulator cavity have been given in Section 2(2) of this report. Thermocouples were used in these measurements.

Temperature measurements were made to verify the agreement among the three PRT's in the Improved Blackbody Simulator, and measurements were also made to determine the temperature variation with time when the Improved Blackbody Simulator was operated with the Artronix 5301-E controller. These last two measurement series were performed with the four-terminal PRT's connected to a four-terminal resistance monitor. For future use this same technique should be employed. The resistance monitor should deliver 1 mA maximum test current and should read 25 to 250 Ω with an accuracy of 0.01 Ω.

Comparison measurements were made among the three PRT's (serial Nos. 6793, 7760, and 7761) at a temperature of 503 K. The read-out differences were as follows:

$$\Delta T \ (7760-7761): \quad 0.048 \ K$$
$$\Delta T \ (7761-6793): \quad 0.330 \ K$$

It is not possible to explain this data with complete certainty because the PRT's have been bonded into the blackbody simulator core. However, it seems likely that 7760 and 7761 are reading correctly and a 0.3 K error is associated with 6793. This explanation is supported by the fact that the resistance value of 6793 is lower than it would be if it agreed more closely with 7760 and 7761; and an anomalous low resistance reading can be explained by an unwanted resistance shunt that might have developed during the bonding of the PRT's in the core. On the basis of this explanation, operating procedures for the system include use of PRT 6793 with the Artronix 5301-E

temperature controller, and use of either PRT 7760 or 7761 (or both) for reading out the temperature.

During our temperature measurement study it was found that the PRT resistance measurements are polarized. This phenomenon was found to be a thermocouple effect associated with the PRT leads. This problem was solved by reversing the PRT leads in a certain way and then averaging the two readings. Suppose the four PRT leads are labeled A, B, C, and D, and suppose that for the first reading they are connected thus:

A: PLUS Drive Current
B: MINUS Drive Current
C: PLUS Voltage Monitor
D: MINUS Voltage Monitor

The leads should be reversed so that A and B are interchanged and so that C and D are interchanged.

This procedure was applied to PRT's 7760 and 7761. There are eight ways to connect a four-terminal PRT to a four-terminal resistance monitor. PRT's 7760 and 7761 were both connected in these eight ways and readings were recorded. The eight values for each PRT were paired according to A,B and C,D reversal as described above, and this resulted in four corrected resistance values for each PRT. The standard deviation for each PRT was calculated from each set of four values. The standard deviation was also calculated for the eight readings (for each PRT) with no pairing involved. The results are as follows:

PRT serial number:	7760	7761
1σ (for 4 pairs of readings)	0.023 K	0.006 K
1σ (for 8 readings with no pairing)	0.562 K	0.170 K

These data show the importance of reversing the leads and averaging the two readings. Because the 1σ values are so small for the four pairs of readings, any pair of readings is satisfactory and only two readings, not eight, need be taken.

During checkout of the Artronix 5301-E temperature controller, temperature measurements were made to see how uniform the temperature was as a function of time. The results were as follows:

$$1\sigma \text{ (over 1.25 h)} = 0.030 \text{ K}$$
$$1\sigma \text{ (over 3.5 h)} = 0.040 \text{ K}$$
$$1\sigma \text{ (over 5.0 h)} = 0.054 \text{ K}$$

Temperature Range

A requirement for the Improved Blackbody Simulator is that it operate from 10ᵒ K to 600 K in a 20 K environment. The unit delivered to AEDC will meet these requirements. However, in the course of our study it has become evident that 200 K to 500 K is a better operating range than 100 K to 600 K.

Section 2(3), entitled "Polythermal Cavity Effects," discusses radiance errors for various cavity temperature distributions and various cavity temperature errors. These errors are considered at different cavity operating temperatures and for different radiation wavelengths. That discussion shows that radiance errors are severer at lower blackbody simulator temperatures and at shorter radiation wavelengths. In order to avoid the larger errors

at 100 K, it is recommended that the minimum operating temperature of the Improved Blackbody Simulator be limited to 200 K instead of 100 K.

Our study of materials has shown that a number of important substances begin to be affected by high temperature in the range between 500 K and 600 K. Among these materials are copper with a cupric oxide coating, Aluma-Black coating on aluminum, and Teflon, which is used as insulation on the leads of our platinum resistance thermometers. In order to avoid high temperature strains on the components in the Improved Blackbody Simulator, it is recommended that the maximum operating temperature be limited to 500 K instead of 600 K.

The blackbody simulator delivered to AEDC will meet the 100 K to 600 K requirement, and the more limited 200 K to 500 K range is recommended for better accuracy and operating life. These comments should be especially considered for future construction of blackbody simulators. If new specifications are written with 200 K to 500 K limits, a better product may be obtained.

SECTION 6

SIGNAL LEVEL ATTENUATION AND CALIBRATION

Our study has shown that the best way to provide signal level attenuation and calibration for the 7V Chamber IR Simulator application is to use demagnifying optical modules. The first module forms a demagnified image of the blackbody simulator aperture and the other modules form demagnified images of the first demagnified image. This method can give high accuracy attenuation and calibration over many decades of attenuation. Along with the temperature measurement and control described in Sec. 5, this method of signal level attenuation and calibration provides the best method for measuring and controlling the blackbody energy output for the 7V Chamber IR Simulator application. Advantages of this attenuation-calibration system include:

(1) Attenuation whose uniformity as a function of wavelength over the range 1 to 100 μm is the best of all the methods considered.
(2) More than six decades of attenuation.
(3) Self-contained and self-checked calibration. This feature will enable the method to provide a calibration monitor for comparison of signal levels between different laboratories.
(4) Excellent rejection of unwanted radiant energy.
(5) Magnified focal plane to allow greater flexibility for future setups with multiple and/or moving sources.

Infrared signal level attenuation and calibration fall within the general category of infrared radiometry. At even moderate signal levels, infrared radiometry is one of the most difficult technical areas in which to make accurate measurements. At very low signal levels this situation is far more severe. Appendix D1 gives more information on the difficulty of infrared attenuation and calibration at very low signal levels.

45

The first part of this section describes the recommended attenuation-calibration method. The last part of this section describes some alternate methods.

The recommended attenuation-calibration system is illustrated in Fig. 11. Components of this system which nave been studied and are described below include: (1) the blackbody simulator, (2) the apertures, (3) the radiation monitor, and (4) the optical attenuators.

The Blackbody Simulator (1)

The calibration source for the recommended attenuation-calibration system is a blackbody simulator with a 12.5mm (0.5 inch) diameter cavity opening. Apertures varying from 0.5 to 7.5mm (0.020 to 0.300 inches) in diameter should be employed and these apertures will perform like ideal black surfaces because they will be backed up by a blackbody simulator cavity with an oversized opening. Sections 1 through 3 have shown that a spherical cavity makes the best blackbody simulator.

The Apertures (2)

Blackbody simulator systems often employ blackbody simulator cavities with separate aperture plates in front of them, and that plan is recommended here. In such an arrangement the aperture approximates an ideal twc dimensional black surface. Figure 12 illustrates a typical aperture construction. Not the following characteristics of the aperture illustrated in Fig. 12.

Aperture Heating

Aperture heating is a serious problem that can lead to erroneous system test results. To minimize radiation falling on the aperture plate, a shield shoul be placed between the blackbody cavity and the aperture. To minimize the effect of any possible aperture heating, a second radiation shield should be placed between the aperture plate and the infrared simulator optical system.
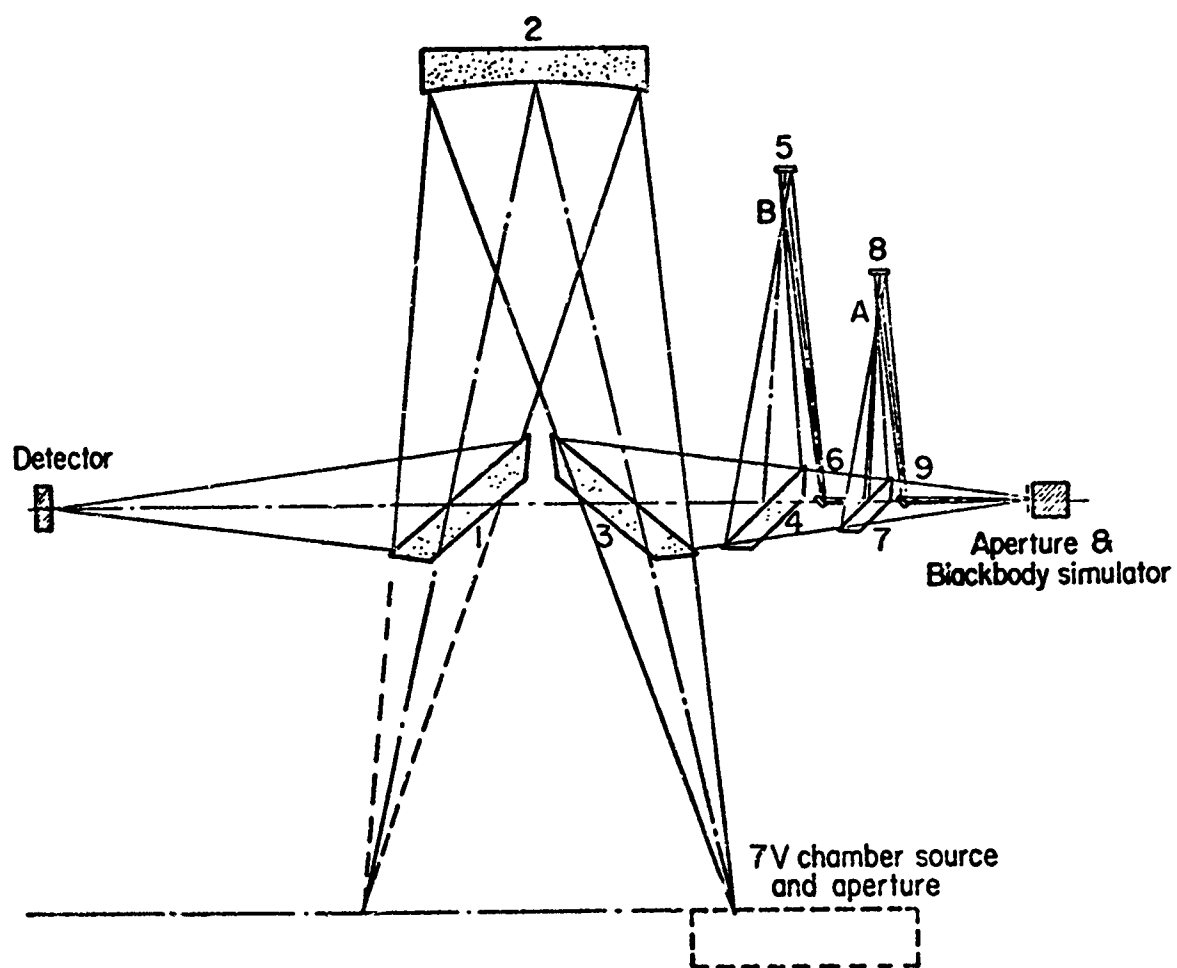
Fig. 11. Simplified Attenuation-Calibration System.

To
heat
sink

Radiation
shields

Oversize cavity
opening

Aperture plate

To optical
system of
infrared
simulator

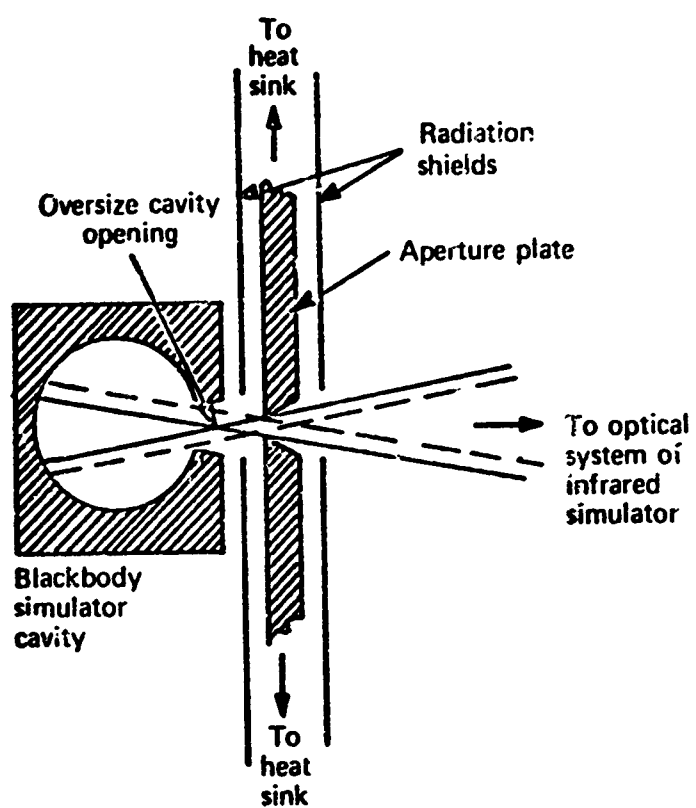Blackbody
simulator
cavity

To
heat
sink

Fig. 12.   Aperture Details.

Furthermore, the aperture plate itself should be made of a relatively thick piece of high conductivity metal with a positive thermal conductive path to a heat sink, because such a design minimizes aperture heating.

Two-Dimensional Effect

Blackbody theory will be employed to determine the radiation field strength for various system configurations. This theory assumes the aperture is an ideal two dimensional black surface. The performance characteristics of ideal blackness will be due to an oversized blackbody simulator cavity located behind the aperture. The two dimensional character will be approximated by careful aperture-plate design. The hole through the plate should have a conical wall as shown in Figure 12 with the cone opening away from the blackbody simulator cavity. A very shallow cone should be machined on the side facing the cavity. This latter feature will assist in providing a sharp-edged circular aperture. The aperture should be located on the side of the aperture plate nearest the cavity so that the aperture-cavity distance can be minimized, for minimum cavity opening, while the cavity-aperture-plate distance is maximized for best radiation shielding.

Aperture Sizes

Previous experimental work has shown that the minimum reliable aperture diameter that can be employed for precision radiometric calibration work is about 0.5mm (0.020 inches). There are several reasons for this. Aperture heating is one reason. As the size of the hole decreases the effect of even a small rise in the temperature of the aperture plate will cause increasing errors. Another problem with small apertures is the effect of edge irregularities. Either a manufacturing flaw or dust particles on the aperture edge will cause a much greater percentage error for small apertures than for large apertures when the same size flaw is involved. Finally there is a problem associated with measuring the diameter of very small apertures. When a filar microscope eyepiece is employed,

there is some question as to where the index hair should be placed relative to the edge of the aperture. Another problem with the measurement of aperture diameters is associated with imperfections in the two dimensional character of the aperture. If the aperture has any thickness or if it is not in a plane perpendicular to the light beam employed in the measurement, then the diameter measured will not correspond to the effective area when the aperture is used with an infrared simulator where an optically fast cone (e.g. f/4) is filled by radiation from the aperture. As an example of aperture measurement errors suppose a 0.5mm (0.020 inch) diameter aperture has a measurement error of $2.5\mu m$ (0.0001 inches). This corresponds to a one half percent diameter error or a one percent area error. These values are typical and help to explain why apertures below about 0.5mm (0.020 inches) diameter should not be used for accurate radiometric calibration. At the other extreme, the maximum diameter aperture used in an infrared simulator depends on the opening of the blackbody simulator cavity, the spacing between the cavity and the aperture plate and finally on the f/# of the infrared simulator optical system. For the recommended system, a preliminary calculation gives a maximum aperture size of 7.5mm (0.30 inches) diameter.

The Radiation Monitor (3)

The recommended radiation monitor can be seen by looking at Fig. 11. It consists of a collecting concave mirror (2), a flat mirror (1), and a detector assembly. This optical collection assembly will be used in two configurations. With mirror (3) in place, the radiation monitor will receive energy from the calibration reference blackbody simulator shown to the right in Fig. 11. When mirror (3) is removed the energy received will be from the AEDC 7V Chamber blackbody simulator assembly. Figure 11 shows an f/4 cone of radiation proceeding from either of these two sources toward the collecting concave mirror (2).

This geometry has been selected so tne radiation will correspond to that traveling from the 7V Chamber source to the large 27 inch diameter collimating mirror when the chamber is in normal operation. Normal chamber operation (see Fig. 13) will occur either when mirrors 2 and 3 of Fig. 11 are removed or when the entire attenuation-calibration assembly is removed.

The ideal shape of the collecting concave mirror as shown in Fig. 11 is a circular mirror taken from the equatorial zone of a prolate ellip oid. This is a difficult design to make, so a study should be made of fabrication and testing techniques and also of alternate mirror designs.

The detector assembly may be designed by following any one of three approaches:

(1) Use a spectrally flat detector.

(2) Use a sensitive, broadband detector whose spectral characteristics are accurately known.

(3) Use a detector package that simulates as closely as possible the characteristics of the detector assembly in the unit under test.

There are advantages and limitations to all three; all three are recommended for use in different applications; and all three have been studied and are reported on below:

Spectrally Flat Detector

This is an obvious choice for a calibration detector device, and it should be employed in general whenever signal levels are sufficiently high to permit the use of such a detector. Unfortunately, spectrally flat detectors are usually less sensitive than their spectrally non-flat counterparts, so test programs will be encountered where this choice of detector type will not be satisfactory.
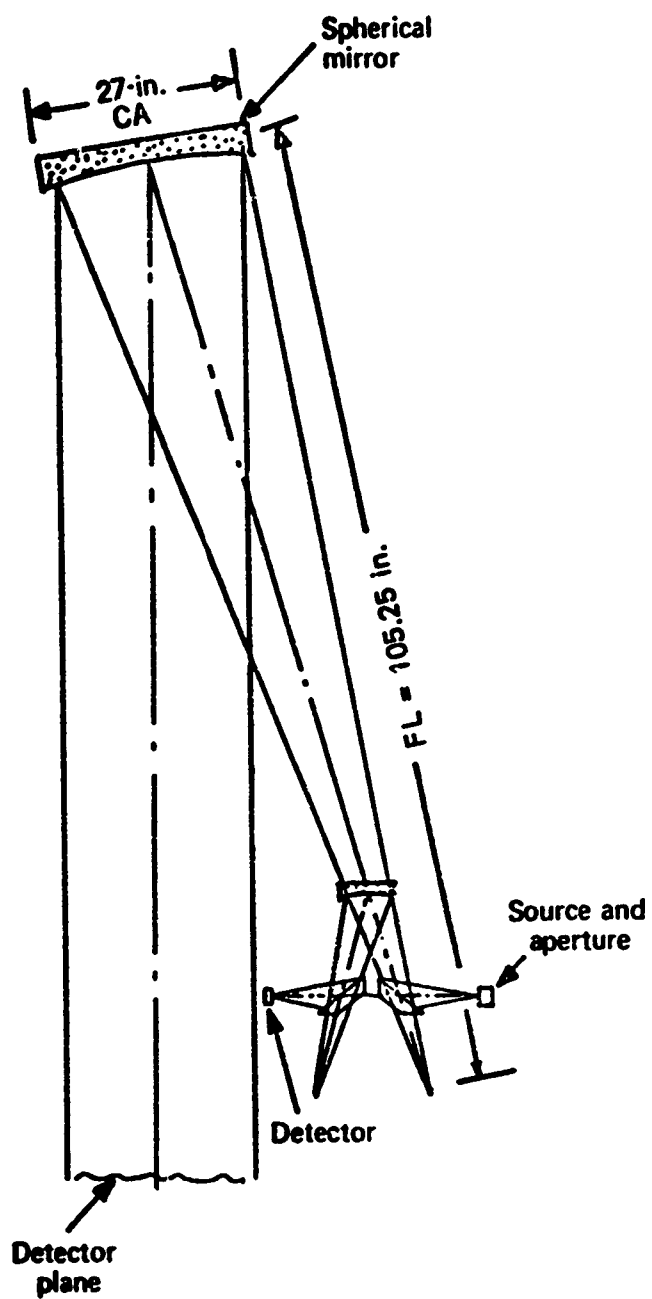
Fig. 13. 7V Chamber with Attenuation-Calibration
System in Place.

Sensitive, Broadband Detector with Accurately Known Spectral Response

This type of detector is recommended for general test and calibration measurements. One such detector assembly can be selected for high sensitivity and reasonably broad spectral response, and then it can be carefully tested and calibrated (especially with respect to spectral response) so that it can be used for calibration purposes when the infrared simulator is testing any one of a large variety of devices. However, even though this is the recommended type of detector, serious problems may be involved. In most cases there will be significant differences in the spectral characteristics of the calibration detector, the calibration source (a blackbody simulator), and the unit under test. These differences in spectral response must be properly taken into account, and the proper way to do so is called normalization. Normalization is best treated by F. E. Nicodemus (Appl. Opt. 12(12): 2960-2973, Dec. 1973). Normalization calculations are always hard to make, and for many situations with infrared simulators they will involve test units whose spectral information will not be as accurate as desired. Normalization calculations often place unusual importance on certain overlap spectral areas where some of the input spectral data are of limited accuracy, and thus normalization calculations often give results with rather large uncertainties or errors.

Custom Detector Assembly

The above-cited problems for a sensitive, general-purpose detector give rise to another solution to the detector selection problem. That solution is to prepare a special detector for each test unit that is brought to the infrared simulator for test. This special detector assembly should duplicate the spectral and spatial image characteristics of the actual unit

under test as closely as possible. This approach to the detector selection problem will result in the simplest and most accurate operation, so this approach is strongly recommended whenever it can be followed. However, two serious problem prevent this solution to the detector selection problem from being followed in every case. These problems are cost and lead time. For most units under test, supplying a semi-duplicate detector package for calibration purposes would prove very costly, and for most units under test such a package would have to be built on short notice.

The radiation monitor has one serious problem that is mentioned here and developed further in Appendix D1, entitled "Ultra-Low Infrared Signals." This problem has to do with contours of sensitivity on the detector. The detector will be used to make comparison measurements between two similar infrared signals that will fall successively on the detector. If the detector sensitive surface were exactly uniform in its response, or if the two signal images falling on the detector were exactly the same in their spatial irradiance distributions, then the detector could accurately read out the ratio of the two signal levels. In general, however, detectors have nonuniform contours of sensitivity, and the two images will be of at least slightly different spatial character, so the ratio of output electrical signals will not exactly represent the ratio of input radiometric signal levels but will include an error effect due to detector sensitivity contours.

The Optical Attenuators (4)

The Attenuator Module

The recommended attenuator module consists of three mirrors--one concave and two flat. The arrangement and function of the attenuator may be seen by examining Fig. 11, mirrors 7, 8, and 9. The two flat mirrors are removable so the attenuator can be inserted into or omitted from the system. The concave

mirror forms a reduced-size image of the aperture. The optical components are so placed that the image of the aperture is located the same optical distance from the collecting mirror 2 when flats 7 and 9 are in place as the aperture itself is when flats 7 and 9 are removed.

Operation of the attenuator can be understood by comparing the two optical arrangements: (1) blackbody, aperture, mirrors 3, 2, 1, detector and (2) black-body, aperture, mirrors 9, 8, 7, 3, 2, 1, detector. In the first case the aperture is imaged on the detector by the concave mirror 2. In the second case a reduced size image of the aperture is formed at point A by concave mirror 8, and this image is re-imaged on the detector by concave mirror 2. Suppose the system is operating in configuration 1, and a signal is being recorded by the detector; then suppose mirrors 7 and 9 are installed so the system then operates in configuration 2. The signal recorded by the detector in the new configuration will be reduced from its previous value by the ratio of the area of the aperture to the area of its image at point A. Thus the attenuator function is performed by the image-size-reduction. The excess energy is lost by overfilling the next optical component - and this excess energy must be adequately suppressed by a system of highly absorbent baffles with appropriate heat sinks.

Cascading Attenuator Modules

It is clear from Fig. 11 that attenuator module 4, 5, 6 performs in the same way that module 7, 8, 9 does. Furthermore, since images of the aperture are formed at points A and B by mirrors 5 and 8 when each attenuator module acts separately; then when both modules are operating by introduction of mirrors 4, 5, 7, and 9, we see that an image of the aperture is formed at point A; an image of that image is formed at point B; and finally an image of the image at B is formed on the detector. If the attenuation of module 7, 8, 9 is α_1 and the attenuation of module 4, 5, 6 is α_2 then the attenuation of the two modules cascaded together is $\alpha_1 \alpha_2$.

The Concave Mirrors

In the earlier section, "The Radiation Monitor," it was noted that the preferred shape for the collecting mirror, 2, is a section of the equatorial zone of a prolate ellipsoid. By similar consideration, it may be seen that the best shapes for the concave mirrors 3 and 8 are off-axis ellipsoids. Preliminary optical analysis has indicated that these ellipsoid shapes can probably be approximated by the use of simple spherical mirrors.

The Complete Attenuation System

Figure 14 illustrates one possible arrangement for the complete attenuation system. Four attenuator modules are shown with attenuation values of about 16, 55, 140, 256. All four acting together provide attenuation of 32,000,000.

Calibration

As mentioned earlier in this section and also in Appendix D1, calibration of very low infrared signals is one of the most difficult of all measurement problems. Most calibration procedures currently in use establish or assume the linearity of some process over a limited attenuation range and then cascade several attenuators or attenuation steps to achieve calibrated attenuation over large ranges. One example of present methods is the use of a readout system consisting of a detector and a preamplifier-amplifier combination that is tested for linearity over several decades. Another example is neutral density filters which are calibrated individually and then used in combination. Another example of present techniques is the calculation of attenuated levels from integrating spheres. All the present calibration methods yield questionable results when they are applied to six or more decades of attenuation. Problems involved include interaction phenomena when attenuators are combined, accounting for rejected energy, reliance on theories without adequate experimental verification, and extension
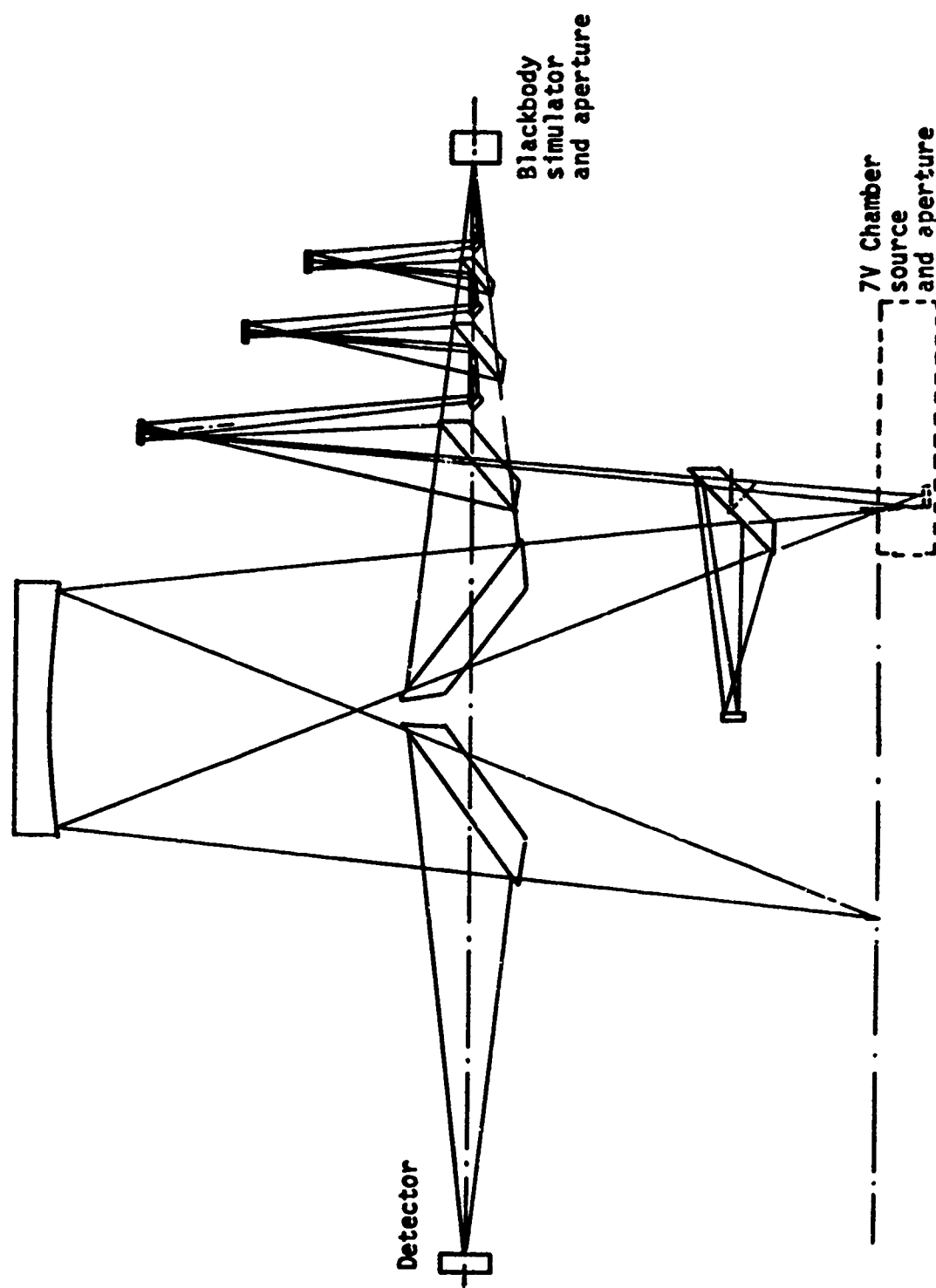
Fig. 14. Complete Attenuation-Calibration System.

of attenuation techniques beyond their linear regions. The calibration pro-
cedure recommended and described here minimizes or eliminates these problems.
This calibration procedure involves the following four items and techniques:

Direct Calibration

The first step in the calibration procedure is to remove mirrors 1, 3,
4, 6, 7, and 9 shown in Fig. 11. This will allow direct infrared radiation
from the blackbody simulator and aperture to fall on the detector. In this
way the direct calibration of the detector and readout electronics can be
made in terms of output signal per unit input infrared signal. The infrared
signal level at the detector, in W/cm^2, is calculable from blackbody theory
combined with distance, aperture, and temperature measurements.

Apertures

Aperture play a key role in the recommended attenuation-calibration
system. Varying aperture diameters provide a range of signal levels with
accurately known variations. Apertures from about 0.5 to 7.5 mm (0.020 to
0.300 in.) diameter are used. Aperture function, construction, and calibra-
tion (measurement of aperture diameters) were described on pp. 46-50.

Optical Attenuators

Optical attenuators play a key role in the recommended attenuation-
calibration system--in fact, their use, more than anything else, distinguishes
the present method from other methods of attempting to achieve very low in-
frared signals with accurate calibration. Design and operation of the opti-
cal attenuators were described on pp. 54-56. Attenuator modules should have
attenuations ranging from about 15:1 to about 250:1. Where aperture varia-
tions from about 0.5 to 7.5 mm diameter can provide for small-step variations
in signal levels, the optical attenuators, singly or in groups, can provide

for large-step variations in signal levels up to six decades or more. Calibration of the attenuators will be based on comparison measurements using the radiation monitor described on pp. 50-54. A special feature of these comparison measurements is the fact that they will be performed between two signals with nearly the same readout values. As an example, consider the calibration of an attenuator with a figure of merit of about 100:1. An aperture 0.625 mm in diameter can be used before the attenuator is introduced, and an aperture of 6.25 mm in diameter can be used after the attenuator is introduced. Then the two readout signals will be nearly the same, and thus it is not necessary to rely on detector-amplifier linearity over a range of more than just a few percent

Redundant Calibration

Redundant calibration should be employed to verify calibration accuracy. Most errors in calibration associated with very low level infrared signals cause anomalous results for redundant calibrations. The absence of anomalous readings indicates a properly calibrated system, and the presence of anomalous readings provides a powerful tool for troubleshooting to remove errors such as aperture heating, aperture diameter errors, scattered radiation problems, and unwanted sources. Redundant calibrations may be illustrated from the example just given of 0.625 and 6.25 mm diameter apertures used to calibrate a 100:1 attenuator. For redundant calibration, aperture pairs of 0.5 and 5.0 mm diameter and also 0.75 and 7.5 mm diameter can be used. If the system is operating properly, the attenuation value determined by all three calibrations will be the same within a fraction of a percent. If errors are present, the three values will not agree that closely.

Alternative Methods of Attenuation

It is believed that the recommended system based on demagnifying optical modules is the best for use in the AEDC 7V infrared simulator. A number of alternate attenuation-calibration techniques have been considered, but all have been judged inferior to the recommended system. There are three main problem areas where most alternate schemes perform poorly. The first has to do with calibration; the second is related to non-uniform variations with respect to wavelength; and the third involves stability with respect to time. These problem areas are especially severe for large amounts of attenuation such as six decades.

In general, techniques and systems for infrared attenuation involve the interaction of radiation with matter; and nearly all these interactions have some wavelength dependence, some changes over long time periods, and some measurement or calibration problems. There are three attenuation techniques where these problems are greatly reduced (1) Variations in aperture diameters (2) Variations in distances between sources and detectors or between conjugate image points (3) Mirror reflection. These three techniques are employed in the attenuation-calibration system just described.

Alternate methods of attenuation that have been considered are: Neutral density filters, integrating spheres, scatter plate attenuators, and crossed polarizers. We now consider each of these methods with special note given to calibration, time stability, wavelength dependence, and many decades of attenuation.

Neutral Density Filters

These devices perhaps represent the best attenuation-calibration method aside from the recommended method, however, they have some serious limitations.

Three types of neutral density filters have been considered: (a) absorption, (b) reflection, and (c) obscuration.

(a) Absorption Filter Attenuators

Dye absorption filters are commonly used in the visible for the attainment of simple absorption. They are, however, not the easiest sort of device to calibrate carefully from first principles. Their application to this problem requires first a material that has a constant transmittance over the spectral region of interest. For six decades of attenuation, the material must have a transmittance of 10^{-6}. Since to a reasonable approximation

$$\tau = (1-\rho)^2 e^{-\alpha x}$$

the maximum value of αx must be about 7. This can be accomplished either by a large value of α or of x.

The choice of materials seems to be either those that are almost opaque in the region, or those that are almost completely transparent. There do exist materials like CsI, KBr, and other alkali halides or heavy metal halides that show good transparency over a wide spectral band and a concomitant flat spectrum. These materials have their shortest resonant wavelength beyond 30μm, and therefore have no structure whatsoever in the region below 30μm. These materials typically have absorption coefficients of between $.01 cm^{-1}$ to $1 cm^{-1}$. This means that the thickness must be 7 cm to 700 cm for six decades of attenuation and that thickness is excessive. Further, care must be taken to insure that the tail of the resonance band does not interfere with the spectral flatness of the absorption. In a practical case, the reflectance must also be known. Actual measurements of reflectance and transmittance are usually in error by about one percent -- not one percent of the value, but one percent. Measurements of very low transmittances are especially difficult, requiring very special instrumentation.

Thus, it seems that one cannot depend upon the <u>calculation</u> of the properties of these absorbers. One could only <u>calibrate</u> them wavelength by wavelength, and this seems too formidable a job to do spectrally over a dynamic range of 10^6.

Errors can arise due to damage or deterioration of filters between the time of calibration and use. Other errors may be involved if calibration is performed in one operating environment and use is made in another environment e.g. conditions of temperature, atmospheric pressure, angle of the filter plane to the direction of radiation propagation etc.

The total attenuation should not be obtained by the use of several slabs of material because of the uncertainty of the effects of inter-reflection. Thus, separate calibrated slabs should be used for each attenuation value.

One can immediately eliminate the almost opaque samples for they all have spectral structure -- except the metals. Thin and relatively thin samples must be used at lower attenuations. Then the structure will show up. The metals, which are relatively flat, lose much of their transmission by reflection. A study of blacks (which are meant to be good emitters, but by that fact must be good absorbers) by Harris shows that over the spectral range of interest 91×10^{-6} g cm^{-2} of goldblack has a density of about 1 and a variation of about 20%. Twice as much goldblack provides twice the density and about twice as much variation. Lenham (JOSA <u>57</u>, 473) shows that the absorption coefficient varies about linearly with a slope of about $1cm^{-1}/\mu m$ between 1 and 20μm for the following metals: V, Cr, Mo, W, Ni, Pd, Pt, Fe, Hf, Ta, Nb.

This is all from the free electron contribution to the absorption. Thus, it should be a consistent property of all metals.

In review there are a number of serious problems for absorption type neutral density filters. There are strong spectral properties associated with every attempt to conceive an absorption filter for six decades of attenuation. Calibration and time stability pose further problems.

(b) Reflection Filter Attenuators

For reflection-type filter attenuators, one can use high or low reflectance arrangements in single and multiple passes. In this discussion, we consider only schemes that use the property of reflective attenuation and not the geometrical properties of curved mirror arrangements.

The simplest arrangement is a partially "silvered" plate that is inserted into the beam. For wavelengths of 1 μm and longer, gold and silver have very flat reflectivities (to within 1% or so) that are about 97% to 98% (Hass and Turner). Shulz (J. Opt. Soc. Am. **44**, 357) shows that, from 0.4 to 1.0 μm, silver has the same absorption relation as the other metals. Thus, even if 98% of the energy is reflected, the transmissions will be given (to a first order) by

$$(1 - r)^2 e^{-\alpha x} \qquad 4 \times 10^{-4} e^{-\alpha x}.$$

The free electron contribution should have a λ^2 dependence, so silver, which has an α of 7 cm^{-1} at 1 μm, would have an α of 21 at 10 μm and 35 at 25 μm. Thus, if we want a transmittance of 10^{-6} for this filter,

$$e^{-\alpha x} = 10^{-6}/(4 \times 10^{-4}) = 1/(4 \times 10^2)$$
$$\alpha x = 6.$$

Then, to obtain 10^{-6} attenuation at 1 μm, x must be 6/7 cm. At 10 μm, this is 6/21 cm, and at 25 μm it is 6/35 cm. Inversely, this will result in factors of 20 variation in transmission, and that is completely unsatisfactory for a neutral density filter. However, when the films are very thin, a different phenomenon applies. Then

$$e^{-\alpha x} = 1 - \alpha x + (\alpha x)^2/2 - \dots .$$

If αx is small, $e^{-\alpha x} \approx 1$. Then

$$\tau = (1-\rho)^2 \, e^{-\alpha x} \simeq (1-\rho)^2 = \text{constant},$$

but the exponent αx must be no more than about 0.01 to keep the error within reason, and then reflectivity cannot give the required attenuation.

The only way to attenuate reflectively is with low reflectivity and multiple passes. Thus, $\tau = \rho^n$. Since we require a transmittance of 10^{-6}, $\rho = 10^{-6/n}$. Thus, with a reflectance of 0.1, six specular reflections will do the job. With a reflectance of 0.05, five reflections are necessary (five gives a τ of 0.3×10^{-6}). With this system one needs a good specular black for control. A diffuse black would give greater attenuation but less control over the radiation.

The best specular black seems to be Cat-A-List gloss black paint available from the Finch Paint Company, Los Angeles, California, or Dark Mirror Coating available from Optical Coating Laboratories, Santa Rosa, California, but the data on such materials are sparse because of their relatively small demand.

A truly diffuse black system would have an attenuation governed by the reflectivity and the ratio of the solid angle of collection to a hemisphere. Thus, for each reflection the transmission is

$$(\rho \, \Omega/2\pi)^n$$

As an example, assume the collection angle is $30°$ or $\pi/6$; then the solid angle is $\sin^2(\pi/6)$, or $\frac{1}{4}$. Assume that ρ is 0.05. Then the transmission is given by the following:

n	τ
1	1/500
2	1/250,000
3	1/125,000,000
4	1/62,500,000,000

Thus, it can be seen that three reflections give the required attenuation--
and more. The diffuse approach gives more than an order of magnitude more
attenuation with only three reflections compared to five reflections with
the specular approach. For this example we assumed an intercept angle of
30°, about an $f/1$ cone. For smaller intercept angles, even more attenuation
can be obtained, as shown below:

n	ρ	θ	$1/\tau$ (approximate)
1	.05	$\pi/180$ (1°)	0.41×10^6
2	.05	$\pi/24$ (7.5°)	54×10^6
2	.05	$\pi/12$ (15°)	3.5×10^6
3	.05	$\pi/6$ (30°)	125×10^6

All these combinations, except the first, provide enough attenuation.
Therefore, consider the simplest in more detail. Very careful consideration
must be given to the baffles and to the temperature of the two reflecting
elements (which must be low enough to make any self-radiation negligible).

Attenuator Box
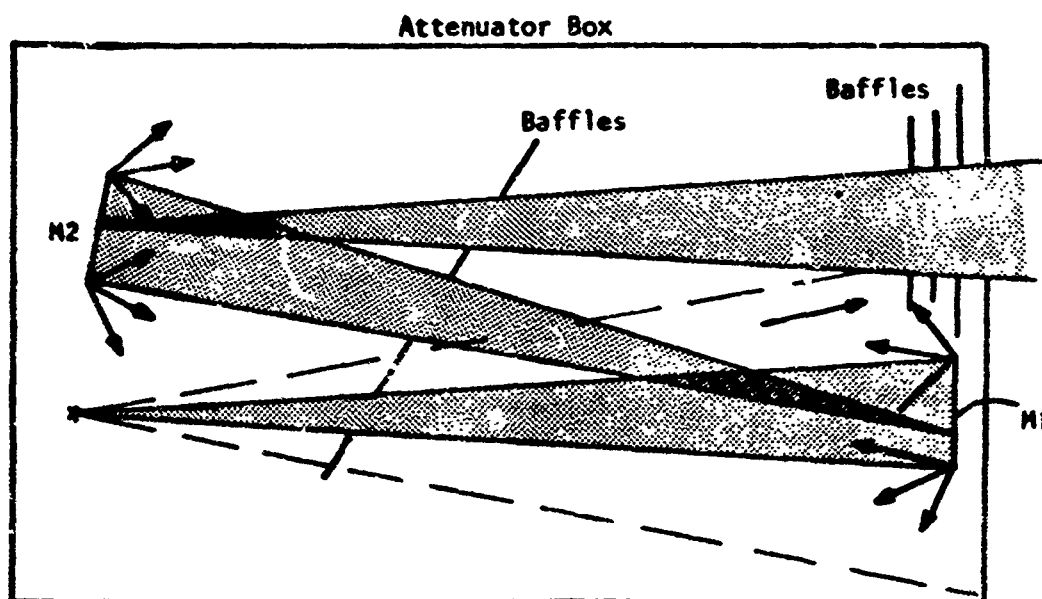
A more thorough design would include moving the source further away from M_1 and baffling near the source. Additional improvement could be made by moving M_1 further from the exit baffles to eliminate radiation into the back of the exit baffles. The entire question of reflection off the walls of the box must be considered. The problem is that attenuation was obtained by using as low a reflectivity surface as possible on M_1 and M_2, but this must also be used as the coating for the walls. Then the radiation geometry (configuration factor) was used as well, but the configuration factor between M_1 and M_2 is smaller than between either M_1 and the walls, or M_2 and the walls. Therefore the stray radiation problem is very severe.

In review, reflection type neutral density filters for six decades of attenuation have problems of calibration, wavelength dependence, and suppression of stray radiation.

(c) Obscuration Filter Attenuators

In a sense, of course, the foregoing example used a form of obscuration. In this section, though, we specifically mean some arrangement of apertures, combs, or other completely opaque material that is inserted in the beam.

The most basic thought here is that the beam must be obscured by a factor of 10^6. To a good approximation, the diffraction angular spread is given (even for this unplane wave) as $\frac{2\lambda}{d}$. This is the diameter of the Airy disc and d is the diameter of the obscuring aperture. The linear spread will be $\frac{2\lambda L}{d}$. If we assume 20μm for the wavelength and a diameter D for the primary mirror of the simulator, then the hole diameter d is given by

$$d = \frac{2\lambda L}{D} = 2\lambda F$$

where F is the F number of the primary. We take this as 4. Then

$$d = 8\lambda = 160\mu m = 0.16mm.$$

This (circular) aperture size is the one that fills the simulator primary mirror with the Airy disc. Notice, however, that 10-μm radiation will have both its Airy disc and the first sidelobe on the mirror. For 5-μm radiation, two sidelobes will be there. Now, if the hole is opened to obtain a factor of 10^6, the diameter must be 160 mm. The beam has to be 16 cm in diameter. It is expensive, cumbersome, and impractical to have such a large beam in the source box. If it is made smaller, then additional attenuation will accrue in which the primary mirror is acting as a stop. This kind of operation can only be checked at the test plane and is very critical as you move in from the first zero. The different wavelengths will all be affected differently. This looks like real multi-color multi-aperture trouble.

The problem is certainly the same in general for other shaped apertures, but usually more complicated in detail. These include squares, triangles, combs, and shades. The first three represent more complicated diffraction patterns and requirs smaller linear dimensions. The last one involves an even smaller dimension because the change in transmittance varies linearly with the opening instead of quadratically.

Simple obscuration of the beam for these wavelength and transmission ranges does not seem practical.

In summary, all three types of neutral density filters have serious flaws even though they are among the best alternatives to the recommended system of attenuators.

Integrating Spheres

The AEDC 7V Infrared Simulator has been equipped with an integrating sphere-type infrared signal attenuator. This equipment has proved to be of competent quality and performance under the operating conditions of the 7V chamber. The serious problem that has been encountered with this equipment involves not attenuation, but rather calibration. Integrating sphere analysis gives a performance equation with the term $(1 - \rho_w A/A_0)$ in the denominator, where c_w is the wall reflectivity, A is the interior area of the sphere minus the area of the ports, and A_0 is the geometrical area of the sphere. Typically A/A_0 will be about 0.99 ± 0.01 and ρ_w will be about 0.96 ± 0.03. For such values, it is clear that a change of 1% in ρ_w--say, from 0.96 to 0.95--would cause a change in system performance from $1/(1 - .96 \times .99)$ to $1/(1 - .95 \times .99)$, or a change from 20 to 16.7--and this is a change of about 3.3 in 18.3, or 18%.

Calibration of integrating sphere attenuator systems is difficult because of this problem: the magnified dependence of system performance on the wall reflectivity. The problem is made more difficult by the need for wall reflectivity calibration measurements over a broad wavelength region and on a periodic time basis.

Scatterplate Attenuators

For scatterplate attenuators, energy from a source is directed to a scattering surface, which then acts as a new source for a following optical system. Several decades of attenuation can be switched in and out of the system by moving mirrors to achieve large dynamic ranges. However, these attenuator systems suffer from most of the problems that are involved with neutral density filters, and they also have some additional problems.

A collimated beam can be rendered diffuse by a transmitting plate that has many scattering centers. A piece of Irtran-6 (CdTe) with sandblasted faces might accomplish this with no absorption.

The first question is the arrangement by which the attenuation might be generated. We will assume that the plate is a nonattenuation uniform (Lambertian) scatterer. Then the radiation geometry is as follows:
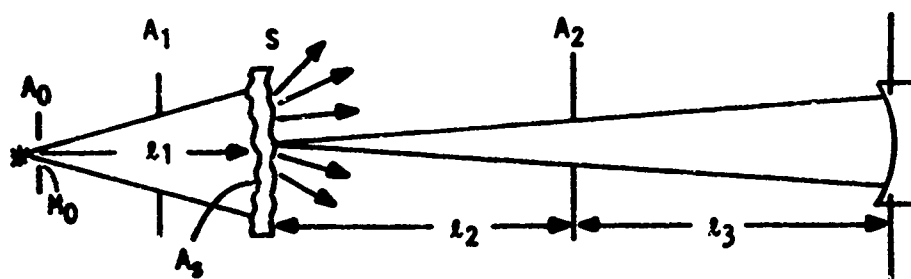
The blackbody simulator is Lambertian, so the irradiance on S is $M_0\Omega/\pi$ where Ω is the area of A_0 divided by $\ell_1{}^2$. The perfect scatterplate then creates another Lambert radiator. The irradiance on the mirror will then be

$$\frac{M_0\Omega_1}{\pi}\frac{\Omega_2}{\pi} \quad = \quad \frac{M}{\pi^2}\frac{A_0}{\ell_1{}^2}\frac{A_S}{(\ell_2 + \ell_3)^2} \ .$$

The transmittance (reciprocal of attenuation) can be defined as this value divided by $M_0 A_0/\pi(\ell_2+\ell_3)^2$ because this is what the irradiance on the mirror would be if A_0 were at S and there were no scatterplates. Then

$$\tau_1 \quad = \quad \frac{A_S}{\pi\ell_1{}^2} \ .$$

A second scatterplate interposed would make the

$$\tau_2 \quad = \quad \frac{A_S{}^2}{\pi^2\ell_1{}^2\ell_2{}^2} \ .$$

For n scatterplates

$$\tau_n = \frac{A_o^n}{\pi^n \ell^{2n}} = \left(\frac{\Omega}{\pi}\right)^n.$$

The assumption was made that all ℓ are the same value, and this is reasonable. Consider the following examples:

n	α	Ω	τ
1	0.1	10^{-2}	3.2×10^{-3}
1	0.01	10^{-4}	3.2×10^{-5}
2	0.1	10^{-2}	1.0×10^{-5}
2	0.01	10^{-4}	1.0×10^{-9}

Thus, varying the linear angle from 0.1 rad (6°) to .01 rad (0.6°) provides two decades of attenuation for one scatterplate and four decades for two scatterplates.

The problem is that the scatter will not be uniform with wavelength or angle. The degree to which these variations occur is principally a function of λ/d, the wavelength of the light and the diameter of the scattering particle. Scattering clearly is a wavelength-dependent process. Can one arrange the physical parameters so that this variation is negligible?

In the region for which λ/d is small, so that the particles or roughness of the plate have characteristic dimensions of about 50 μm (0.05 mm) or larger, the scattering is proportional to $1/\lambda^4$. This means, for instance, that radiation at 25 μm will be scattered out of the beam 625 times less effectively than 5 μm radiation. This will be true even if scattering is made small for 25 μm radiation. Of course, if this is true the scatterplate is not very effective anyway.

If the scattering particles are of the order of the wavelength, Mie scattering rather than Rayleigh scattering prevails. In this case, the dependence is not λ^{-4}, but oscillates with λ/d and varies with refractive index. These variations on the order of 5 to 10% also rule out this type of scatterplate. Additional problems are the directionality of Mie scattering and the difficulty of generating a plate with proper small-particle characteristics.

Scatter plates must be calibrated in an environment that is as near as possible to the environment of final usage. Like neutral density filters, scatter plates have serious problems concerning possible damage or deterioration between calibration and use.

In addition to these problems which are similar to filter problems there are additional attenuator system problems. While neutral density filters can be added or removed from an optical system with little of no adjustment for the extra component, scatter plates can only be entered or withdrawn by performing significant changes in the optical systems employed. Thus the introduction of a scatter plate requires calibration of the scatter plate itself plus proper accounting for the changes that are made in the optical system. A final problem is the baffling of unwanted scattered radiation.

Crossed Polarizers

The use of crossed polarizers in concept is a viable attenuation device. One polarizer produces linear (or another sort of) polarized infrared radiation and a second polarizer is placed either in the same sense or some degree of opposite sense, so that varying degrees of attenuation can be obtained. The least attenuation is the simple transmission of the two polarizers. This attenuation for randomly polarized blackbody radiation will be 50%. Then, hopefully, the attenuation will increase to some very large number like 10^6 when the polarizers are exactly crossed.

The three useful polarizers for the infrared region have been piles of plates like salt of AgBr, reflection at Brewster's angle off a piece of germanium or equivalent, and wire grids, whether they be real wires or evaporated metallic lines on some substrate. Brewster's angle is determined by

$$\theta_i = \tan^{-1} n$$

The polarization degree is normally determined by

$$P = \frac{R_p - R_s}{R_p + R_s}$$

We take here just the ratio of the two polarization components:

$$\text{Ratio} = \frac{R_p}{R_s} = \frac{\tan^2(\theta_i - \theta_t) \quad \sin^2(\theta_i + \theta_t)}{\tan^2(\theta_i + \theta_t) \quad \sin^2(\theta_i - \theta_t)}$$

$$= \frac{\tan^2\Delta}{\tan^2\sigma} \frac{\sin^2\sigma}{\sin^2\Delta} = \frac{\cos^2(\theta_i + \theta_t)}{\cos^2(\theta_i - \theta_t)} .$$

This, of course, is the Fresnel relationship. We see that when

$$\theta_i + \theta_t = \pi/2:$$

$$\text{Ratio} = \cos^{-2}(\theta_i - \theta_t) \qquad 0(o).$$

Near Brewster's angle the variation of polarization ratio from zero is a cosine squared dependence. From Snell's law we know

$$\sin\theta_i = n \sin\theta_t .$$

The index of air is taken as 1. The index of germanium is about 4. Thus,

$$\sin\theta_i = 4 \sin\theta_t$$

$$\tan\theta_i = n = 4$$

$$\theta_i = \tan^{-1} 4 = 76°$$

$$\theta_t = 14°$$

Note: $\theta_i + \theta_t = \pi/2$, and $\theta_i - \theta_t = 62°$. Thus,

$$\text{Ratio} = \cos^{-2} 62° \quad 0(\circ)$$

The variation goes as

$$\frac{d\,\text{Ratio}}{d\lambda} = \frac{d\,\cos^{-2}(\theta_i - \theta_t)}{d\,(\theta_i - \theta_t)} \quad \frac{d(\theta_i - \theta_t)}{dn} \quad \frac{dn}{d\lambda}$$

$$= 2\cos^{-3}(\theta_i - \theta_t)\sin(\theta_i - \theta_t)\frac{d}{dn}\left[\tan^{-1}n - (\frac{\pi}{2} - \tan^{-1}n)\right]\frac{dn}{d\lambda}$$

$$= 2\cos^{-3}62°\,\sin62°\frac{d}{dn}\,(2\tan^{-1}n - \pi/2)\frac{dn}{d\lambda}$$

$$= 2(.47)^{-3}(.88)\,2(1 + n^2)^{-1}\frac{dn}{d\lambda}$$

$$\approx 2\quad\frac{dn}{d\lambda}$$

Note that the relative change is this value divided by $(.47)^{-2}$. The expression is

$$\frac{1}{\text{Ratio}}\quad\frac{d\,\text{Ratio}}{d\lambda} = 4\tan62°\,(1 + n^2)^{-1}\frac{dn}{d\lambda}$$

$$\approx 0.44\frac{dn}{d\lambda}$$

Valu s for $dn/d\lambda$ were obtained from the work of Platt, Wolfe, et al. on their recent measurements. Among the infrared materials for which there are adequate index data, germanium has one of the highest indexes and the lowest dispersion. It is hard to do better than this. Note that the beam must be collimated, tne incidence angle must be well known, and the system must be calibrated. The geometry shoulu be about as shown below:
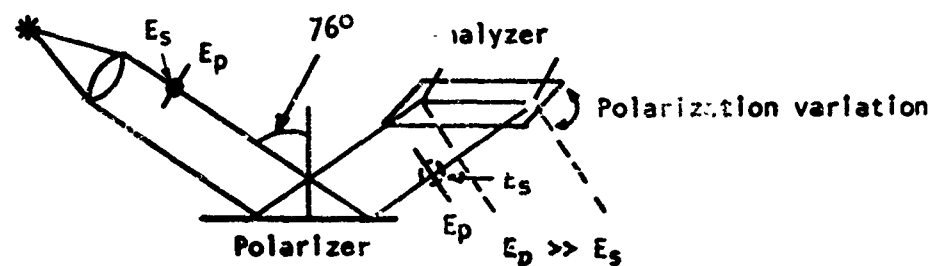
The second reflection goes out of th plane of the paper. One can repeat the reflections for the polarizers, in which case

$$\text{ratio} = (R_p/R_8)^m = \cos^{2m}\Delta \; 0^m(o)$$

$$\frac{d \text{ ratio}}{d\lambda} = 2m \cos^{-2m-1}\Delta \; \sin\Delta \; 2(1+n^2)^{-1} \frac{dn}{d\lambda} .$$

The relative change is

$$\frac{1}{\text{ratio}} \frac{d \text{ ratio}}{d\lambda} = 2m \tan\Delta \; 2(1+n^2)^{-1} \frac{dn}{d\lambda}$$

$$= m \left(\frac{1}{\text{ratio}} \frac{d \text{ ratio}}{d\lambda} \right)_{\text{single reflection}}$$

The wavelength variation is larger for a larger number of reflections.

The use of successive plane parallel plates is in a sense very similar to that just discussed. In this case the transmitted beam is used thus:
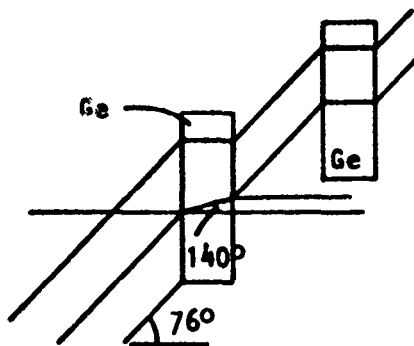
By this technique additional polarization is accomplished. One could do it
also by additional reflections, as above. A repeat analysis could be done,
but it seems clear that the transmission will be just that lost by reflection,
plus the effects of absorption. It just cannot be better; it must be worse
including some rather important absorption around 20 μm.

Thus, we must conclude that wavelength variations rule out this
technique.

Source Temperature Changes

A final method of attenuation should be mentioned, and that involves
changing the temperature of the blackbody simulator. This technique repre-
sents a change in the physics of the source itself rather than an operation on
the radiation from the source, and so the discussion of this technique does
not follow the framework of the arguments listed above.

This is a very poor way to perform attenuation. The process and pit-
falls are best described by Nicodemus (F. E. Nicodemus, "Normalization in
Radiometry," Appl. Opt. 12(12):2960-2973, 1973). Part of p. 2964 of that
paper is repeated as Appendix D3, and Fig. 2 on that page shows the way
that spectrally mismatched sources and detectors can lead to uncertain
readings. Equation (21) on that page gives a true radiance value 109 times

the peak normalized value. It is not suggested that errors of a factor of 109 will be made by using a source-temperature-change technique for attenuation, but errors of several hundred percent are sometimes experienced.

A 1500:1 Attenuator

A special 1500:1 attenuator has been delivered to AEDC as part of the present contract. This attenuator is a simple two-fixed-mirror version of the complete attenuation system described in the first part of this section and illustrated by Fig. 11. The earlier discussion should be referred to for background information concerning this type of attenuator.

The 1500:1 attenuator is shown in Fig. 15, and one arrangement in the 7 V chamber is illustrated in Fig. 16. The Improved Blackbody Simulator is shown with the 1500:1 attenuator in both figures. An image of the aperture of the Improved Blackbody Simulator is formed by the first mirror with a ratio of distances of 14 in.:2.3 in. An image of that image is formed by the second mirror, and again the ratio of image distances is 14 in.:2.3 in. Thus the geometrical magnification is $(2.3/14)^2 = 1/37$, and the corresponding signal level attenuation is $37^2:1 = 1370:1$. The mirrors have gold reflecting surfaces, and if their reflectivity is 0.95, then the system attenuation is $1370/0.95^2 = 1518$, or approximately 1500:1.
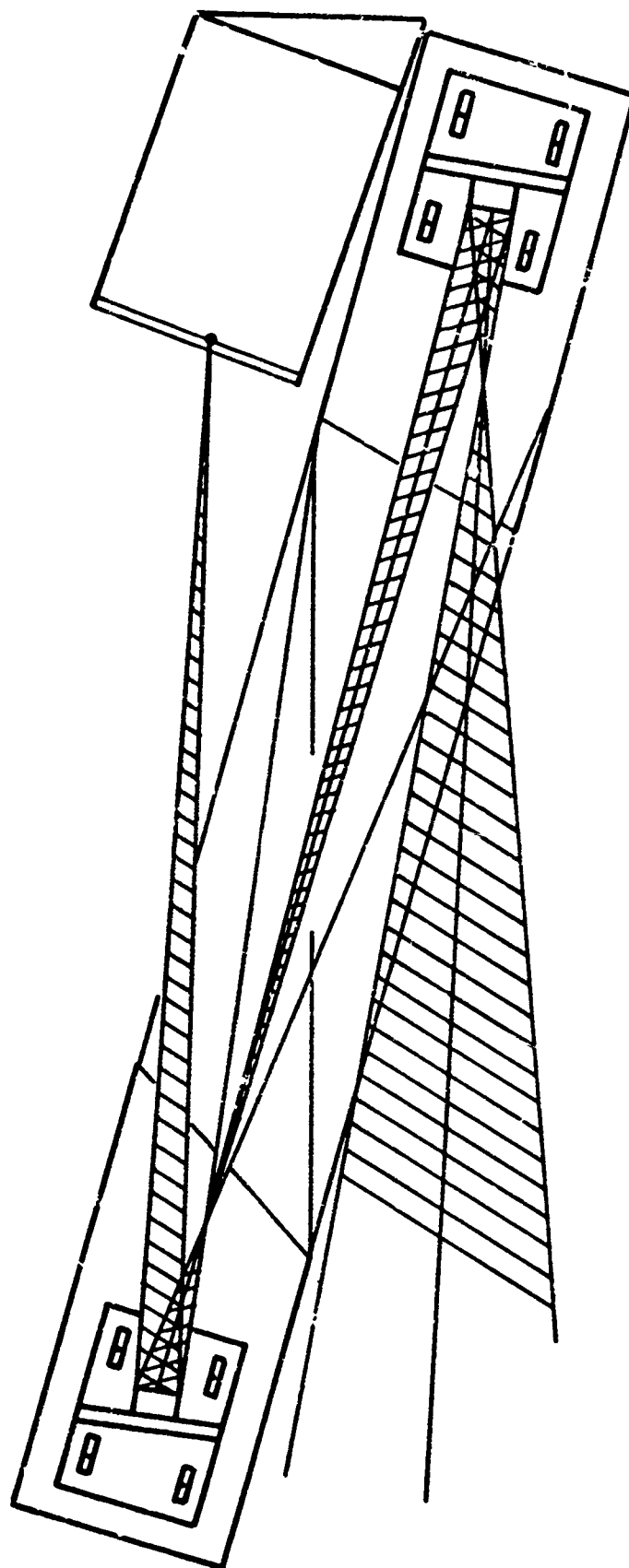
Fig. 15. 1500:1 Attenuator.

Fig. 16. 1500:1 Attenuator in TV Chamber.

OPTICAL ANALYSIS

Our study of the optical system has been in two parts: (1) an analysis of the existing 27-in.-diameter tilted sphere arrangement and (2) the design and analysis of a three-mirror system that will provide improved optical quality (with special emphasis on an optimum blur circle size at larger off-axis angles between simulated target sources and chamber optical equipment center line).

Existing 27-In.-Diameter Tilted Sphere

The general arrangement of the existing 27-in.-diameter tilted sphere is shown in Fig. 17. Specifications are as follows:

Mirror clear aperture	685.8 mm	(27 in.)
Distance from mirror to detector or sensor plane	3251.2 mm	(128 in.)
Radius of curvature (concave spherical)	5346.7 mm	(210.5 in.)

The image quality of the existing system is shown in Figs. 18, 19, and 20. Figure 18 gives the radius of the blur image in milliradians, both for the total blur image and for the rms blur image. Note that the horizontal scale (mirror tilt) is the half angle. Figure 19 is a spot diagram for the full aperture at 5° tilt (half angle). Figure 20 is the ray fan aberration plot, which shows details of the system aberrations and from which the aberrations for smaller aperture devices can be predicted. This figure has been prepared for operations at a tilt half angle of 5°; the solid curve labeled y' is for the meridional or tangential plane, the dotted curve labeled x' is for the perpendicular or sagittal plane, and the curve labeled y'_x is the sagittal coma measured in the meridional plane. Appendix E1 gives a detailed
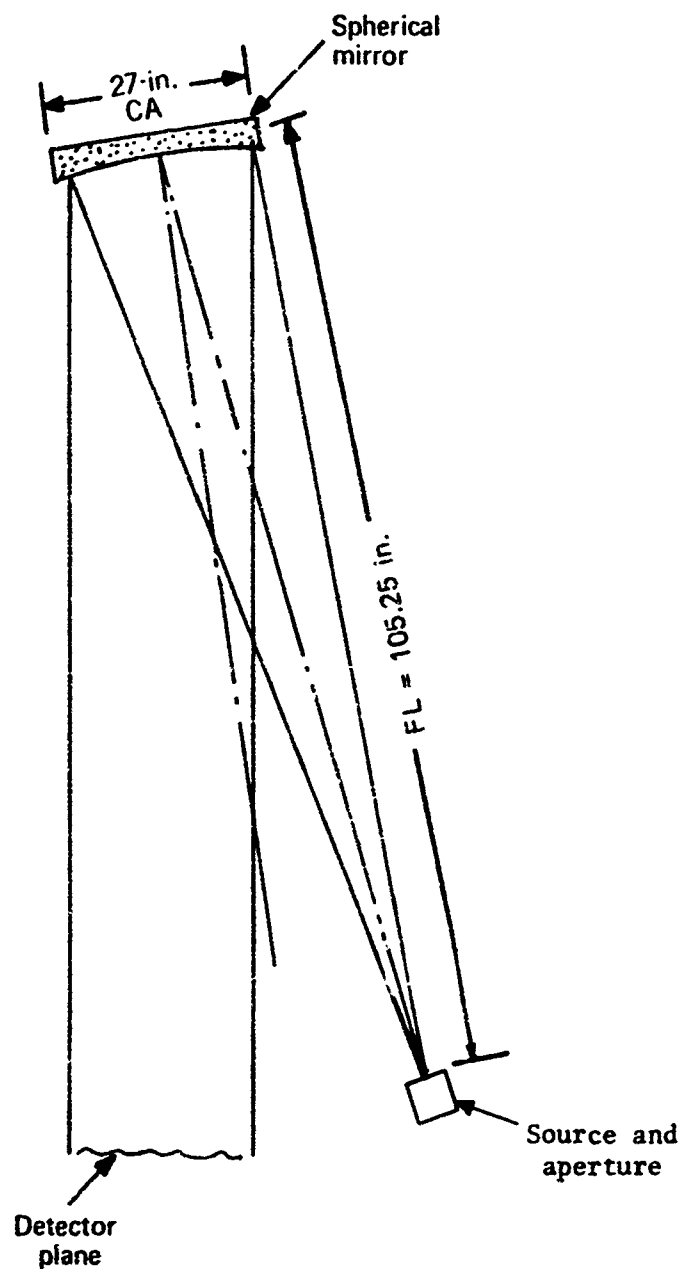
79

Fig. 17. System Drawing, Existing
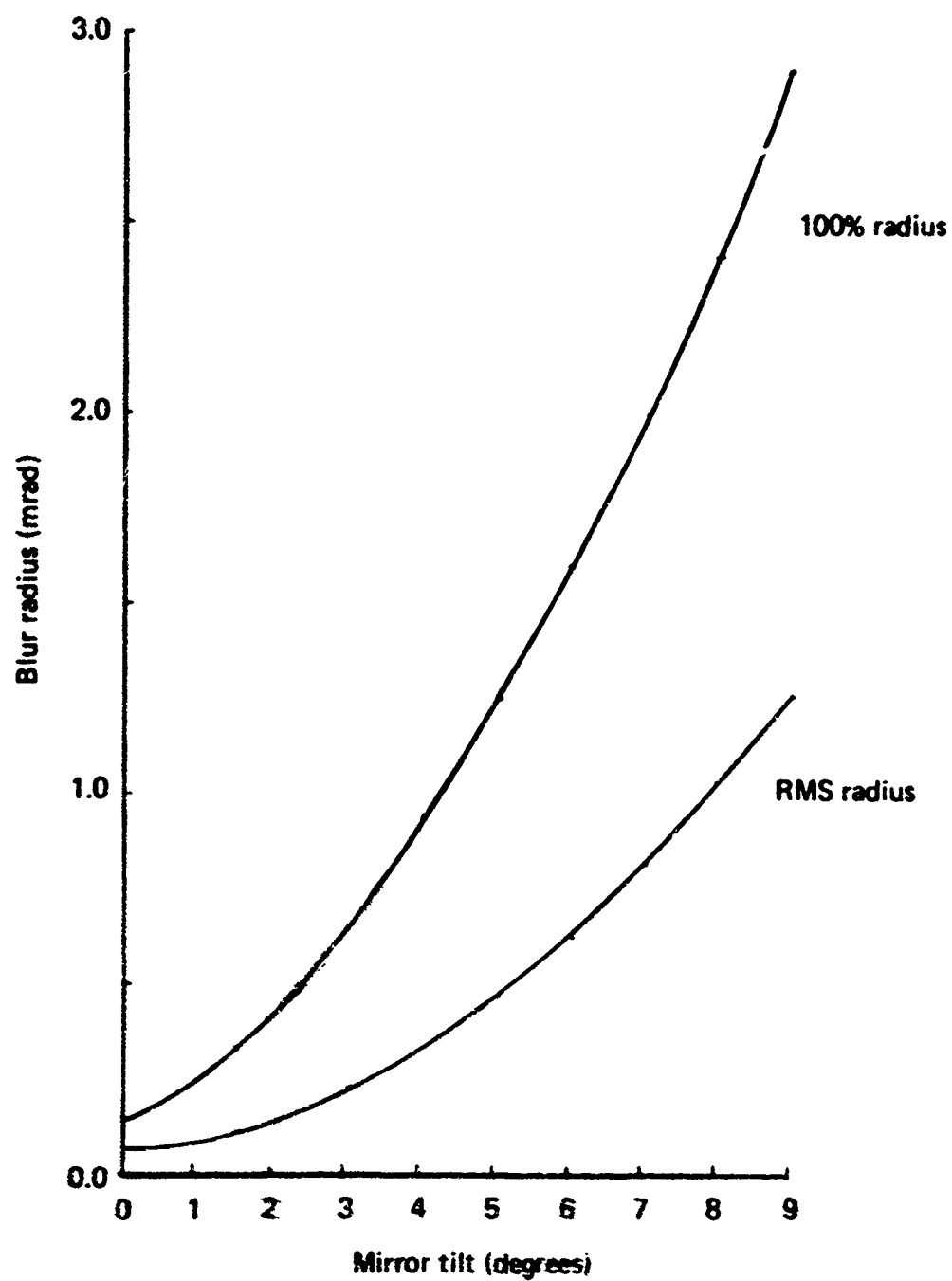27-in. Tilted Sphere.

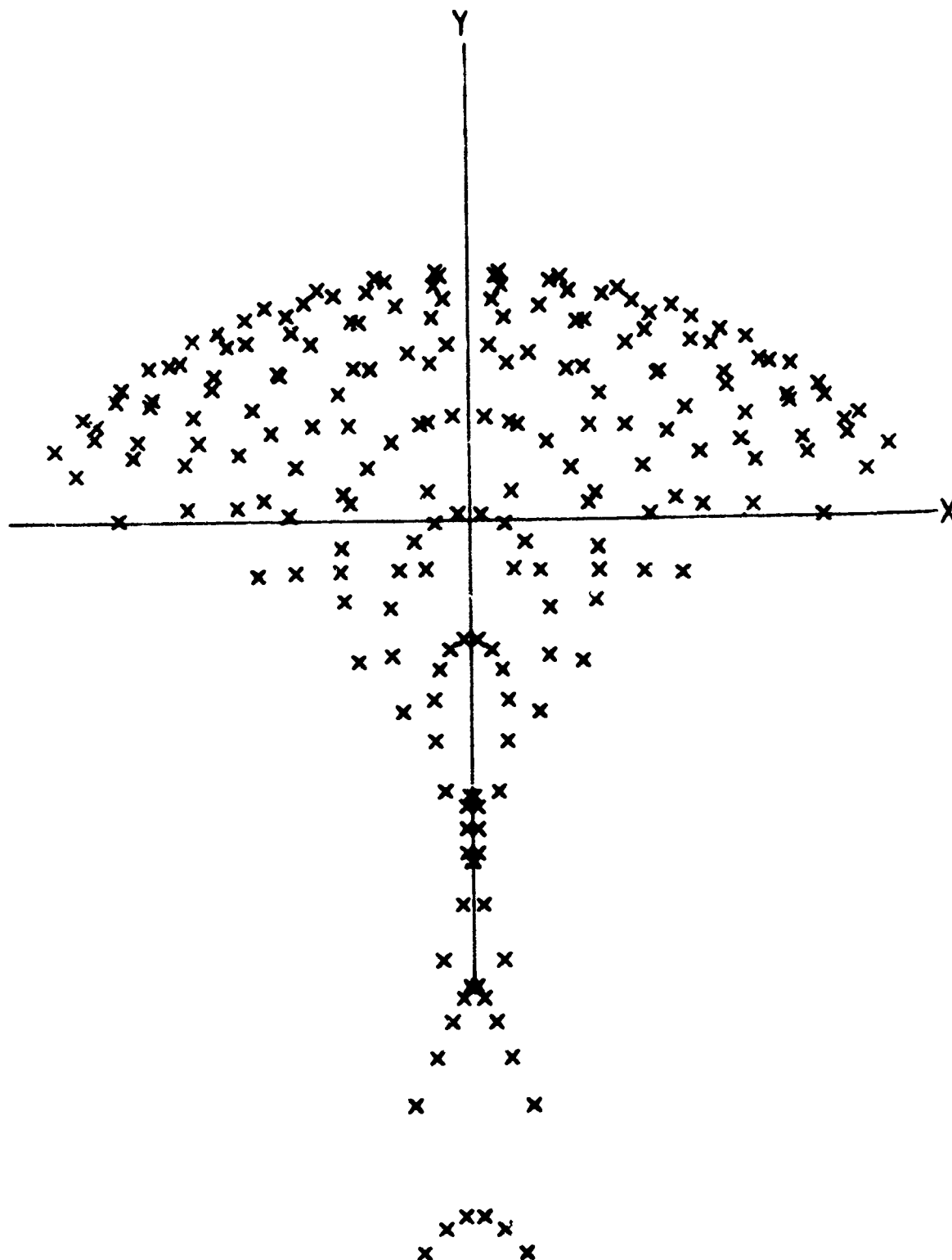Fig. 18. Size of Blur Image: 27-in. $f/3.9$ Spherical Mirror.

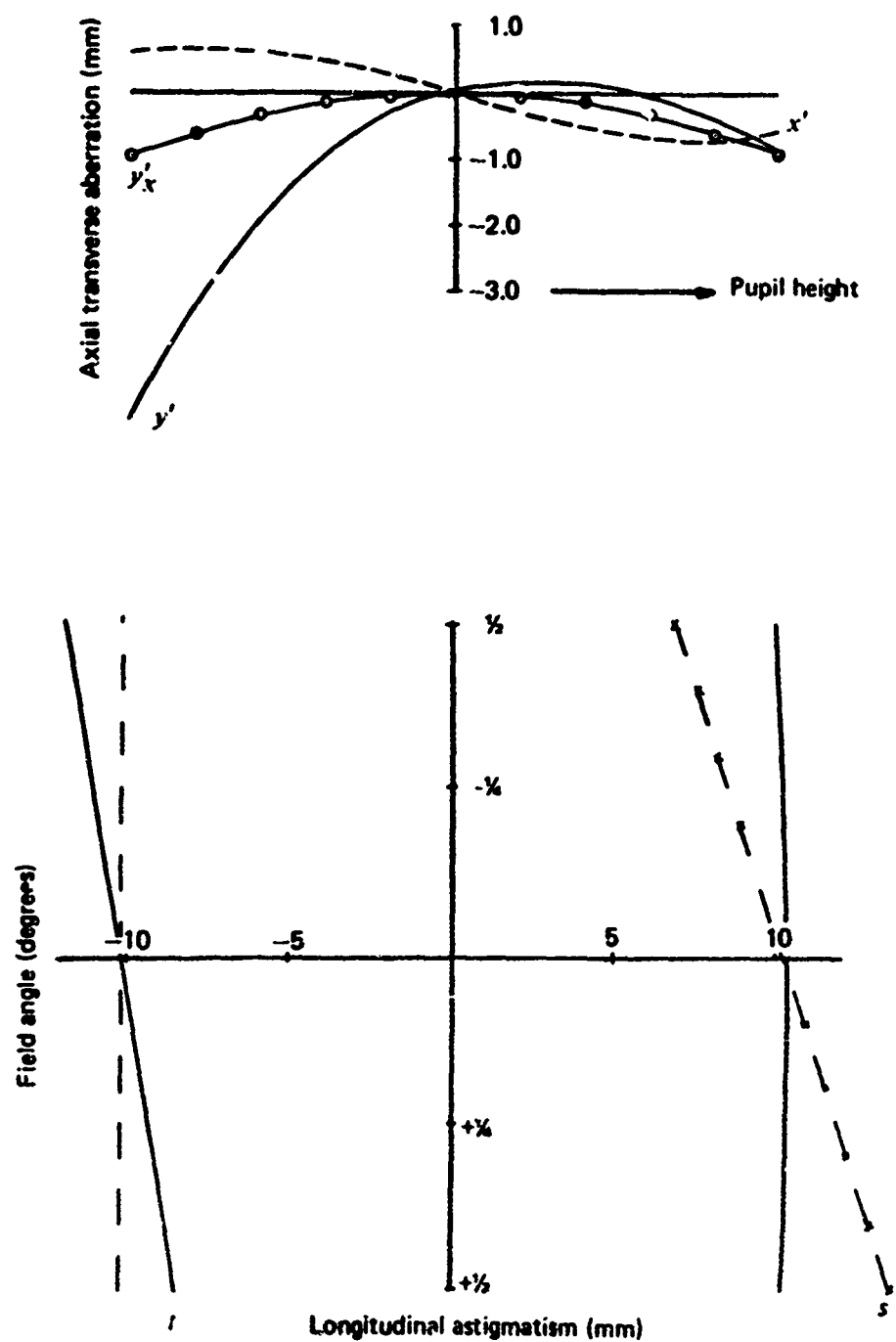Fig. 19. Spot Diagram: 27-in. $f/3.9$ Spherical Mirror.

Fig. 20.   Ray Fans: 27-in. $f/3.9$ Sphere with 5° Tilt.

explanation of these ray fan aberration plots. An additional aberration problem is an apparent position error; this distortion, which is like "dynamic distortion" in biocular (not binocular) viewers, arises from the fact that an image is located where the energy centroid seems to lie. This can cause as much as 0.75 mrad error in the present system.

Interpreting these figures, we note that, for larger tilt angles, the image deteriorates almost quadratically with tilt angle. This effect is due to astigmatism. At smaller tilt angles the main aberration is coma; however, for most operations the tilt angle is more than 2^O and in these cases astigmatism dominates. At 5° half-angle tilt, the blur image is more than 2 mrad.

A New Three-Mirror System

In the development of the new three-mirror system, considerable study was given to the existing system and to possible simple variations on that system. An analysis of that system is given above.

The first, simple variation considered was replacement of the 27-in.-diameter spherical mirror by an off-axis paraboloidal mirror. An off-axis paraboloid, more correctly called an eccentric pupil paraboloid, gives a perfectly stigmatic axial image, and for small fields of view it can give much superior images compared with a tilted sphere. For a field of view of $\pm0.5^O$, the full field resolution is remarkably uniform at about 1/3 mrad and the image is not tilted significantly (less than 1^O), also, field distortion is small (about 1%). The image improvement with an off-axis paraboloid would be dramatic. However, it is difficult to make the large off-axis paraboloid required here. Furthermore, an off-axis paraboloid mirror can be used at only one tilt angle, and that is contrary to the variable tilt

operation of the 7V Chamber Infrared Simulator. For even 1° difference from the design off-axis angle, coma aberration amounts to 5 mrad and it increases linearly with larger angles from the design axis.

Our new design of a three-mirror system is in a class called "tilted component optics." An informative introduction to this type of optics design is given by R. A. Buchroeder, "Design Examples of Tilted-Component Telescopes (TCT's) (a Class of Unobscured Reflectors," Optical Sciences Center Tech. Rept. 68, May 1971. The introduction to that report is reprinted as Appendix E2 of this report.

Two design objectives were considered of special importance. First, the axial image quality had to be substantially improved, with a goal of 30X reduction in blur size compared to the existing tilted sphere design. Second, the off-axis imagery should be as good as possible so that moderately large targets and/or target motion could be employed. Another consideration was that optical design problems had to be weighed against practical problems so that a simple, useful system would be obtained.

To achieve an axially correct image there are several alternative solutions. One is to turn the primary into an off-axis paraboloid--a solution rejected for reasons already mentioned. Another alternative is to turn the primary into a toroid, which eliminates its astigmatism, making it particularly useful for smaller aperture apparatus. The problem with this approach is that making a large toroid is almost as difficult as making a large off-axis paraboloid. Although it might be a trifle easier to make, the toroid at full aperture is considerably inferior in optical quality relative to an off-axis paraboloid. A third alternative is to use a toroidal secondary and leave the primary symmetric, but turn it into a hyperboloid. Small toroids are not hard to make, and this solution gives an axial image of 0.02 mrad.

However, this image is quite tilted and afflicted with serious assymetric distortions. A similar solution, leaving the primary spherical and adding an aspheric plate reflector, has the same distortion problem, and so is rejected. This survey of possible alternative designs leads to the solution that was selected as most practical.

It was decided to use concave rather than convex mirrors becaus: the former are easier to test. Image tilt in the earlier concepts was caused by the second mirror working at high magnification to extract the image from the light beam. Thus, image tilt could be eliminated by using another mirror similar to the other small one, tipped oppositely to correct image tilt. For convenience of calculation, it was desirable that the light between these two small mirrors be parallel in the tangential plane. For a simplification in the calculation of coma and tilt, the radii of the two small mirrors were chosen to be the same. Spacings were chosen for a condition of parallel light and so that the reimaged pupil would fall on the last concave mirror. Thus, the first small concave mirror is toroidal to correct over-all astigmatism, and the second is hyperbolic to correct the over-all spherical aberration. Tilts were chosen to correct the coma of the system and to reduce image tilt. The image is not perfectly squared on. Some anamorphic compression in the meridional plane is compensated for by residual image tilt, with a net image distortion of about 2.5%. Target shape can be either distorted by this amount or calibrated by calculation. The distortion is essentially cartesian or linear, not cubic.

The optical prescription is given in Table IV. Dimensions are in millimeters. Tilts are with respect to the effective axis or centerline. The layout, drawn with reasonable care to convey true proportions, is shown

in Fig. 21. Note the direction of target tilt. For better fit into the 7V
Chamber, a flat mirror may be added between M2 and M3.

Table IV. Optical Prescription.

Primary mirror (M1 in Fig. 21)	No change from existing mirror specified at the beginning of this section	
Secondary mirror (M2 in Fig. 21)	Type:	Flat
	Size:	127 mm by 77 mm
	Configuration:	Tilted 55° to optical axis
	Location:	2570 mm from primary mirror; 696.19 mm from tertiary
Tertiary mirror (M3 in Fig. 21)	Type:	Concave circular toroid
	Diameter:	210 mm
	Tilt:	10.9°
	Vertical or tangential radius of curvature:	1228.4456 mm
	Horizontal or sagittal radius of curvature:	1109.77 mm
Quaternary mirror (M4 in Fig. 21)	Type:	Concave hyperboloid
	Diameter:	160 mm
	Tilt:	10.9°
	Radius of curvature:	1228.4456 mm
	Aspheric K:	-7.5
	Location:	575.31 mm from tertiary
Focal or target surface	Type of surface:	Flat
	Size:	1° or 50 mm
	Tilt:	17.6°
	Location:	604.112 mm from quaternary
	Effective system efl:	2850 mm

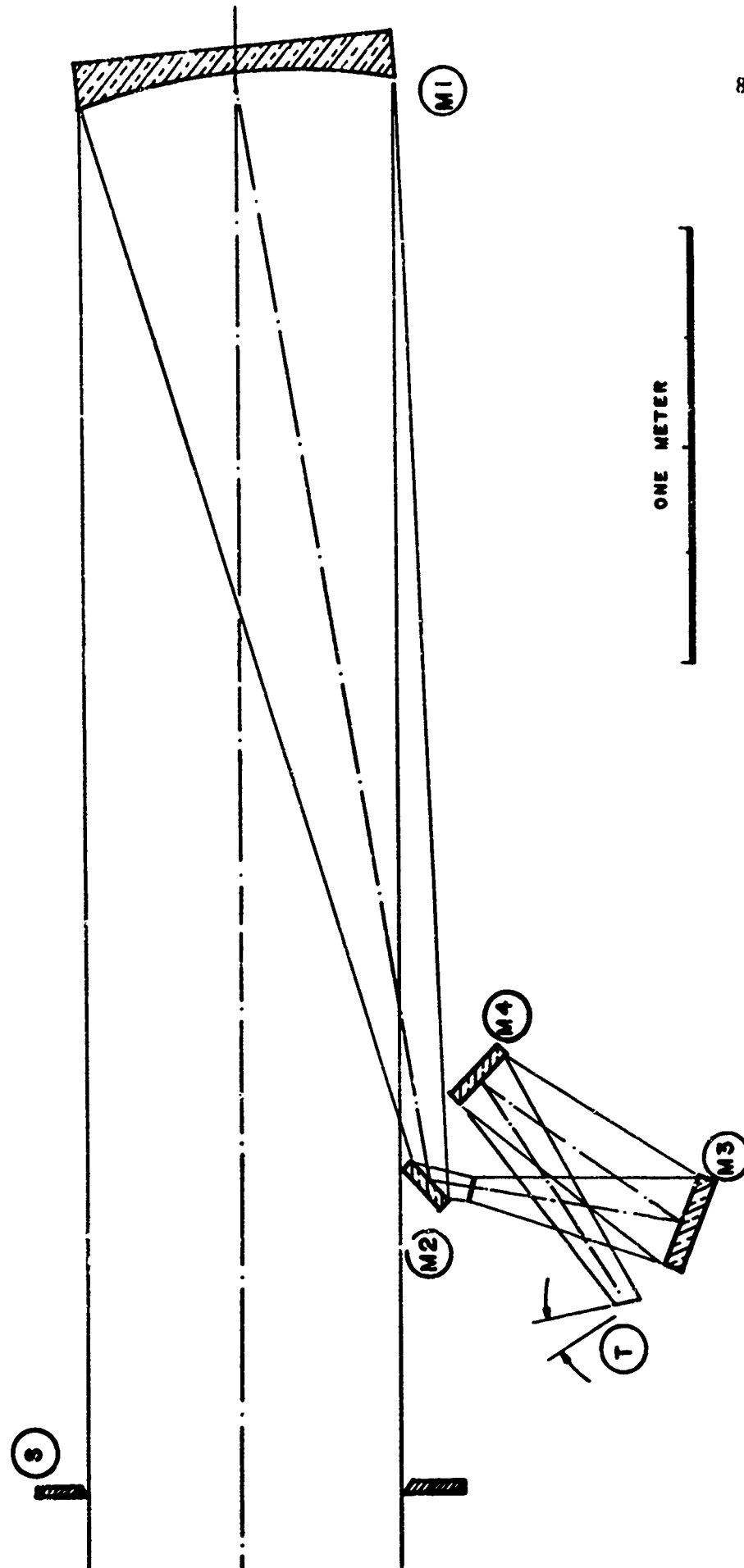T = Target Plane

S = Stop

M1,M2,M3,M4 = Mirrors

ONE METER

Fig. 21. New Optical System Layout.

88

The optical performance of the new design is illustrated in Fig. 22, which is a computer montage of spot diagrams for the field of view. The plot scale is not the same for the spot diagrams as it is for the radial image distances. The image distances are 0.5° off axis for the outer half circle and 0.25° for the inner half circle. The plot scale for the spot diagrams is indicated by the 0.1-mrad-diameter circle. The outermost blur is on the order of 0.2 mrad, which incidentally is superior to what an off-axis paraboloid would offer for a comparable field of view. Figure 23 is the same as Fig. 19 but the spot diagram of the new system has been added at the right side. Comparison of the two spot diagrams shows the image improvement attained by the new system. Even better imagery is possible with a much more elaborate set of asphericities including one on the primary mirror. Also, the image, which is tipped about 17.5°, can be rectified if that should be required, by a more complicated design.

The 2.5% distortion may be expressed as a difference between tangential and sagittal focal scales. The tangential focal scale is about 49.1 mm/deg of field, and the sagittal focal scale is about 50.3 mm/deg of field. Exact experimental calibration will be needed to compensate fabrication and alignment errors. To a certain extent, the calibration will be affected by the type and size of devices being tested, for the distortion depends both on the field and on the aperture size.

Ray fans in Fig. 24 show the nature of the axial correction of this system. Figure 24 should be compared with Fig. 20 for the existing system. We predict less than 0.02 mrad of dynamic distortion, and an axial resolution on the order of 0.03 mrad.

Tolerances were not studied, but owing to the nature of tilted component optics, considerable fabrication errors can be corrected by small changes in
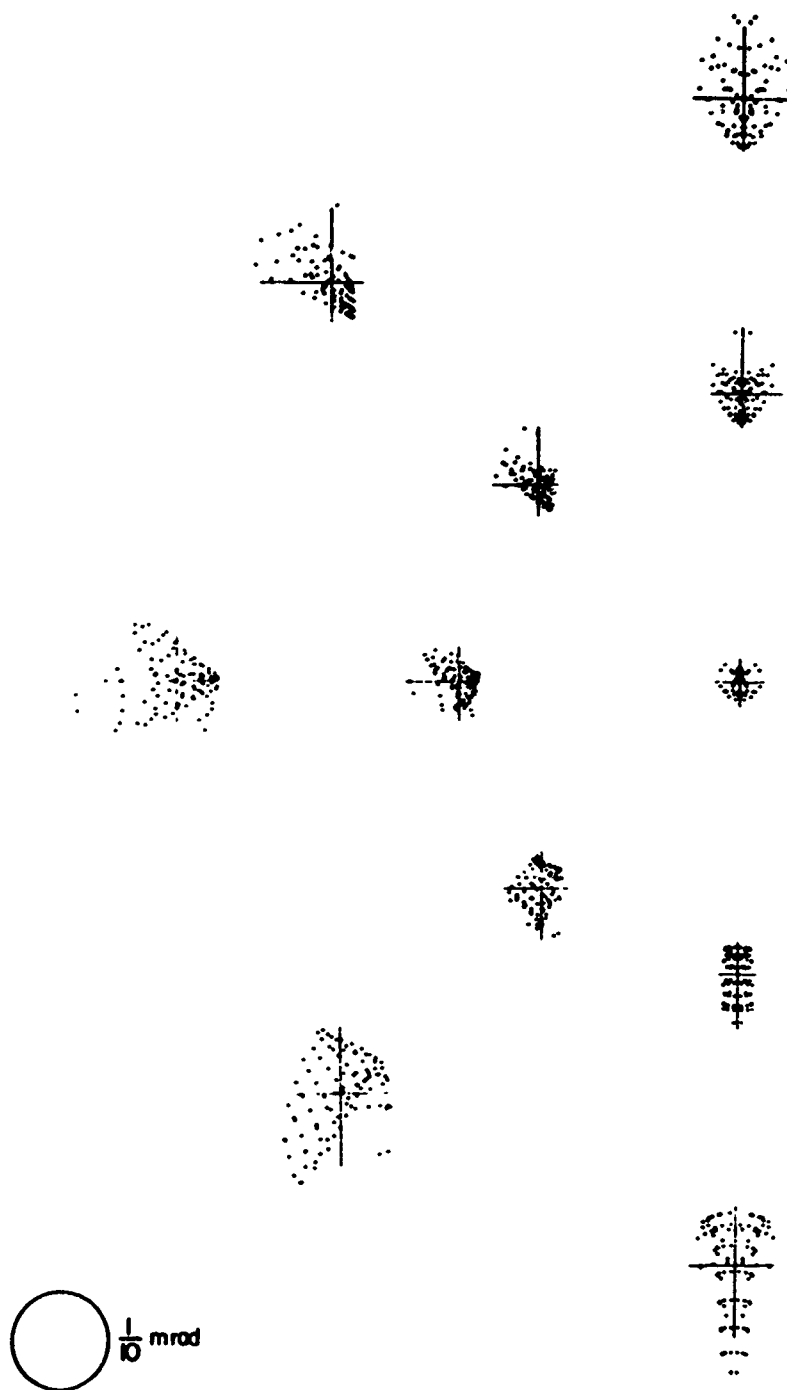
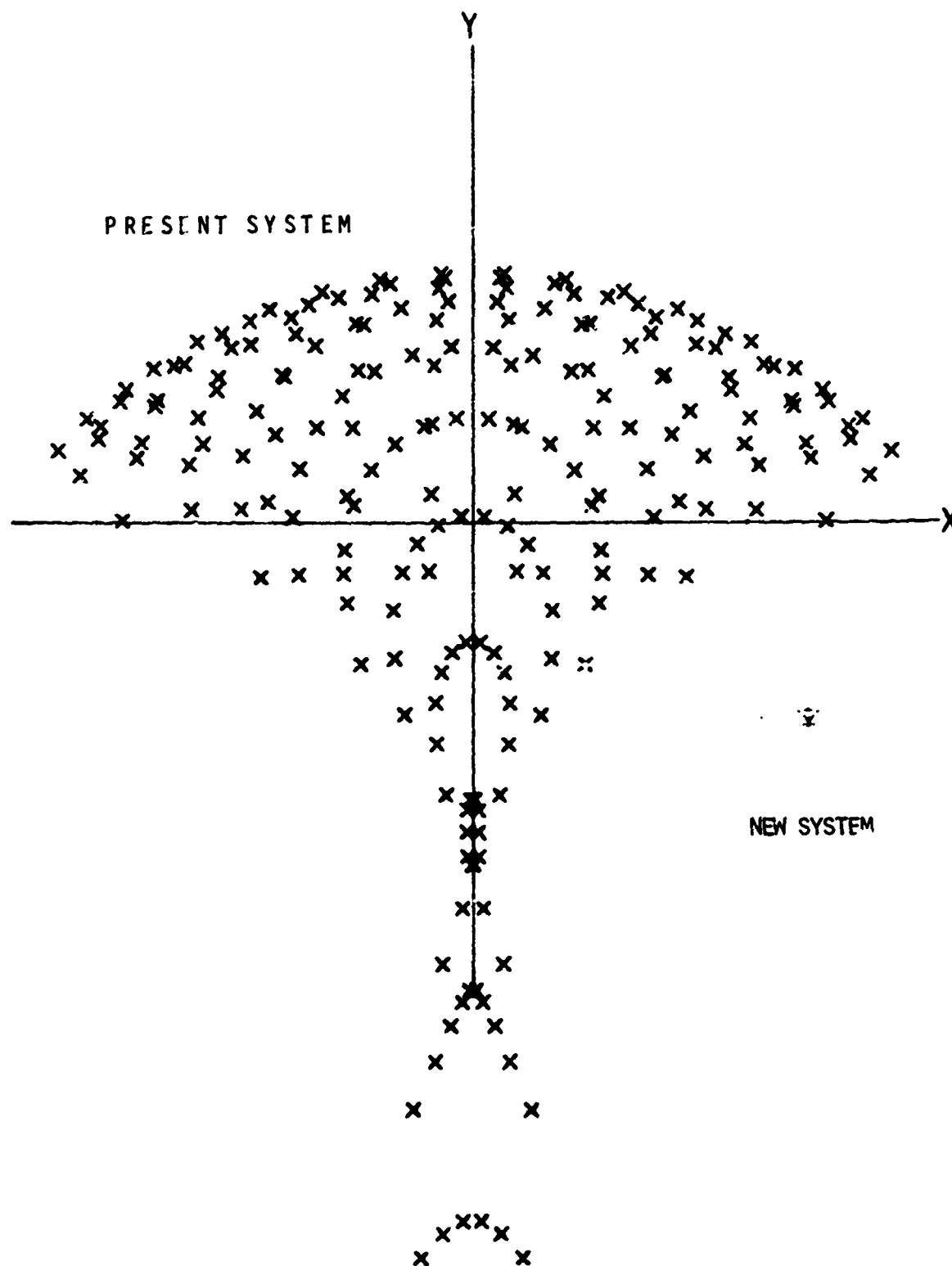Fig. 22. Montage of Spot Diagrams: New Optical System.

Fig. 23. Spot Diagrams: Present System and New System.
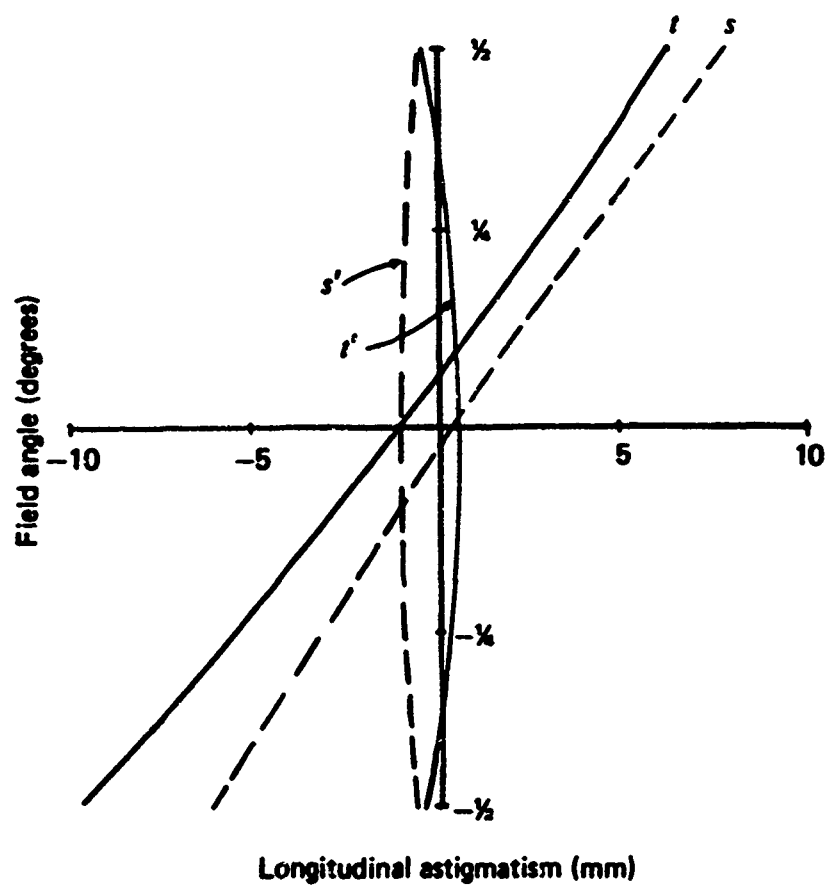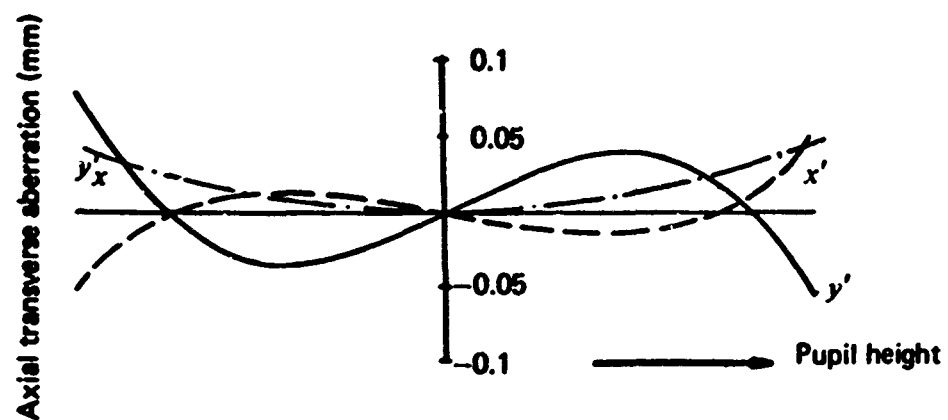
Fig. 24. Ray Fans: New Optical System.

spacings and tilt angles. A subsequent study of tolerances is suggested before optics and fixtures are fabricated for alignment.

The second small concave mirror is hyperboloidal and can be tested with an Offner null lens as well as with other standard test methods. We would consider its fabrication to be routine for any shop capable of designing test apparatus for astronomical mirrors.

The toroidal mirror will be more difficult to make. Its curvatures differ by about 10%, requiring a differential removal of about 0.5 mm of glass, and that is more than one would usually attempt to polish away. There are several ways in which such a mirror might be made; the most practical way is to grind a spherical surface in the customary fashion, then employ directional grinding to wear down one radius to a shorter value.

Testing would be performed by interference tests against test plates with two sets of test plates required, one for each direction. This testing technique provides both curvature and figure information. The making of a toroid is too difficult for an average optical shop, yet it would be a reasonable task for a skilled specialty shop such as that of the Optical Sciences Center.

In conclusion, the new mirror design provides a tilted-component, all-reflective, unobscured collimator with axial imagery about 40 times better than a tilted sphere. The off-axis imagery is 10 times better than the on-axis quality of the sphere. Distortions caused by moving instrumentation around the pupil position are less than .02 mrad. For a field angle of about 1° (17.5 mrad) the image resolution is better than 0.2 mrad on a flat, but inclined, target. The amount of target distortion is cartesian, requiring a 2.5% compression in the meridional (vertical) direction for a true image in the sensor space. These values are nominal. For an optical design of this type, experimental calibration should be performed.

SECTION 8

BLACKBODY SIMULATOR CALIBRATION

Calibration of the Improved Blackbody Simulator is performed in three stages:

Stage I: Calibration prior to delivery to AEDC

Stage II: Calibration at the National Bureau of Standards

Stage III: Continuing calibration

Stage I: Calibration Prior to Delivery to AEDC

Initial calibration with NBS traceability was performed on the Improved Blackbody Simulator at the University of Arizona. This operation consisted of aperture and temperature calibrations.

Aperture Calibrations

Aperture calibration was performed on a Gaertner Scientific Corporation Toolmakers microscope Model 6201-ARS. The smallest division for translation measurement is 0.0001 in., and readings were estimated to 0.00001 in. (10 µin. = 0.254 µm, or about half the wavelength of visible light). NBS traceable calibration was performed by using a calibrated standard of length on the microscope before and after measuring the aperture. The standard consists of a small steel plate with two scribe lines approximately 0.025 in. apart. This standard was calibrated with NBS traceability by Dial Indicator Laboratories, 7844 Lankershim Blvd., North Hollywood, Calif. 91605. The calibrated distance is:

0.02445 ± 0.00001 in.

A copy of the NBS traceable certification by Dial Indicator Laboratories is given in Appendix F.

Measurement of the aperture itself was performed by a series of readings taken 45° apart. These data give an average of

0.02737 ± 0.00004 in. diameter

where the 0.00004 value is the standard deviation calculated from the data. It is our experience that aperture diameter readings are not reliable to better than 0.0001 in., so a better expression of the aperture diameter is

0.0274 ± 0.0001 in.

Temperature Calibration

Temperature calibration was performed with Rosemount Engineering Company platinum resistance thermometers (PRT's) Model 146MA100F. Three of these units are imbedded in the core of the Improved Blackbody Simulator, and all three have been calibrated with NBS traceable calibration. Copies of the calibration data and certificates of NBS traceability are provided in Appendix F. The studies reported on in Section 2, Cavity Temperature Uniformity, verify that the PRT temperature agrees with the effective cavity temperature to within 1.0 K at 600 K and to within 0.5 K at 500 K and lower temperatures.

Stage II: Calibration at the National Bureau of Standards

It is not appropriate that the University of Arizona should instruct NBS as to how an NBS calibration should be performed. However, it seems appropriate that certain points concerning the University of Arizona Improved Blackbody Simulator should be mentioned at this place in the present report

--For radiometric performan e calibrations of the Improved Blackbody Simulator, it is recommended that the unit be arranged as nearly as possible in the same way that it will be used in the AEDC 7V Chamber.

--When radiometric performance readings are being recorded, it is recommended that one or both of the PRT's Nos. 7760 and 7761 have their resistance values recorded using a four-terminal resistance monitor as described in Section 5. It will be possible later to duplicate the calibrated radiometric output by duplicating the PRT resistance values.

--If the outer shield cylinder and the aperture plate are removed for aperture calibration, it is important to use new lengths of 0.090-in.-diameter indium wire for thermal contact gaskets when the unit is reassembled.

Stage III: Continuing Calibration

It is recommended that the calibration of Stage II for the Improved Blackbody Simulator at NBS be repeated on a periodic basis with a recalibration period of two years. During these periodic recalibrations at NBS, and also during normal use at AEDC, it is important to maintain a calibration-and-use log of resistance values of PRT's 7760 and 7761. This log will provide a continuing monitor of the performance of the Improved Blackbody Simulator. When the resistance values of PRT's 7760 and 7761 bear the same relationship to one another as shown in the log, this will be an indication that the unit is performing correctly and the calibration is still valid. If, on the other hand, the relationship between these two resistance values should change, that would be an indication of failure of one of the PRT's so that repair and recalibration would be called for.

SECTION 9

BLACKBODY SIMULATOR DESIGN AND FABRICATION

Our study has shown the best design and fabrication methods for the Improved Blackbody Simulator, and these design and fabrication methods have been incorporated into the unit delivered to AEDC.

Cavity Shape

The initial decision that was made in the design of the Improved Black-body Simulator concerned the cavity shape. Sections 1, 2, and 3 or this report show that a spherical shape is best. In order to prevent rays from the optical system from striking the back wall of the cavity and subsequently exiting by specular reflection, it is necessary to employ the spherical cavity in an off-axis configuration.

Off-Axis Designs

Two types of off-axis designs were considered. The first, which was ultimately selected, has an axially symmetric core. The core has a cylindrical shape with the spherical cavity centered on the axis near one end of the cylinder and the cavity opening centered on one end of the cylinder on the cylinder axis. The off-axis action is achieved by tilting the core so that the system optical axis enters the cavity opening at an angle to the cylincer axis and strikes the back wall of the spherical cavity at a point away from the cylinder axis. The tilt is given to the core by a wedge-shaped base plate. Details of this design can be seen from the drawings in Appendix G.

The second possible type of off-axis design has an off-center cavity opening. Again the core is cylindrical and again the spherical cavity is

centered on the cylinder axis near one end of the cylinder. However, for this alternative design the avity opening is not centered on one end of the cylinder axis; instead the cavity opening is on one end of the cylinder centered about halfway between the cylinder axis and edge. For this design the core is mounted with the cylinder axis parallel to the system optical axis. Then the system optical axis passes through the center of the cavity opening, which is displaced from the cylinder axis, and strikes the back wall of the spherical cavity at a point away from the cylinder axis.

The tilt design was selected instead of the off-center design because the cavity opening of the off-center design extended too far down the side of the spherical cavity, and because the tilt design allowed the core assembly to be symmetrical and more simple.

Radiation Shields

Two concentric cylinders of aluminum act as radiation shields. The inner cylinder includes the precision aperture and has three adjusting screws that feed through to the core. The outer shield contains a clearance aperture for radiation leaving the cavity. The purpose of the outer shield is to limit the exposed area of the inner aperture and thus minimize effects due to aperture heating. These radiation shields (with the precision aperture) must be connected to the base plate by a high conductivity heat path. This function is performed by using indium gaskets, one between the base plate and the outer shield, one between the base plate and the inner shield, and one between the inner shield cylinder and the aperture plate. All three indium gaskets are made of 0.090-in.-diameter indium wire placed in a slightly undersized groove.

Core

The core assembly is an aluminum cylinder with a spherical cavity, cavity aperture, heating coils, insulation, and temperature transducers. The core was constructed as a cylindrical slug with the cavity near one end and the cavity opening centered on the cylinder's axis. The core was made in two parts with hemispherical cavities drilled in each part using a ball end mill. Complementary male and female shoulders were milled on the two facing surfaces with a few thousandths of an inch interference fit; the male shoulder was slightly oversize and the female shoulder was slightly undersize. Then the female part was heated and the male part was cooled with liquid nitrogen. This allowed the two parts to be fitted together, and when thermal equilibrium was established the two parts were permanently bonded together to provide the spherical cavity.

Before assembling the sphere, the inside surface was blackened with a hard black anodized coating as described in Section 4. The end of the cylinder opposite the cavity was made long enough to properly accommodate temperature transducers. Sufficient length was provided so that the sensitive elements would accurately represent the temperature of the cavity and not be cooled by conduction through the temperature sensor leads.

Heater

Two alternative designs were considered for the heater: spiral wrapped heater wires and cartridge heaters. The spiral wrapped design was selected because tests on cavity temperature uniformity like those described in Section 2(2) showed much better results for the spiral wrapped arrangement. Cartridge heaters are better from a maintenance point of view because they can be replaced much more easily than spiral wrapped heaters, but in addition

to the measured deficiency concerning temperature uniformity there is the possibility that cartridge heaters operated between 100 K and 200 K might be deficient in heat conduction through the cartridge insulation from the heater wire to the cartridge shell.

The heater design selected consists of a spiral wrapping of AWG-25 nichrome wire with the wire spaced 24 turns per inch. An anodized coating on the core combined with a braided fiberglass sheath electrically insulates the heater coil. Several coatings of Rust-Oleum, type 4272 black paint increases thermal conduction between the core and heater while at the same time providing mechanical stabilization for the heater wires.

Insulation

Several different insulation schemes were considered. The two most promising were (1) alternate layers of fiberglass cloth and aluminum foil and (2) concentric containers of highly polished metal. The layered insulation promised easier fabrication and a more rugged product; the concentric containers promised radiometric insulation characteristics that more closely followed simple theory. Heat loss tests were run in a vacuum bell jar and the layered insulation gave better results. Since the design consisting of alternate layers of aluminum foil and fiberglass cloth was the less costly and the more reliable, it was selected. There are 15 layers of both materials on the sides, four layers on the front, and eight layers at the rear of the cylindrical core.

Temperature Transducers

The temperature transducers are platinum resistance thermometers (PRT's). A four-wire design is used to eliminate errors due to lead wire resistance. (See Section 5 of this report for more information about the PRT's.)

Core Supports

The core is supported at the top by three adjustment screws that are threaded through the inner shell and at the bottom by a single thin-walled stainless steel tube. This design provides a minimum of thermal conductivity between the core and the low-temperature surroundings and it also provides precision adjustments for the cavity opening relative to the aperture in the inner shell. The three adjustment screws have been machined to provide narrow studs on their ends. These studs fit into cups machined on the ends of three stainless steel locator pins inserted in the core.

Vertical Core Alignment

Special techniques have been used to ensure that the spherical cavity is in proper alignment with the aperture. Vertical positioning of the core is permitted by a collet on the steel tube supporting the bottom of the core. The collet is secured to the base plate, and it can be loosened or tightened to permit vertical adjustments.

The support pins in the core allow for motion in two dimensions while still restraining the over-all cavity position. This is accomplished by a cup-shaped cavity .090 in. in diameter and .080 in. deep. Complementing this cup-shaped pin design, the end of the screws have been machined to be studs .040 in. in diameter and .100 in. long. The result is a play of .025 in. up and down between the stud and the retaining pin.

Alignment is accomplished by loosening the collet that retains the stainless steel tubing and allowing the core to drop to its farthest position from the aperture plate. The collet should be loosened by using the spanner wrench provided in the tool kit that accompanies the Improved Blackbody Simulator. Note that the tool kit also has a small brass bolt that

may be used to position a small cylinder located inside the stainless steel tube. This small cylinder strengthens the tube inside the collet, and it has been drilled and tapped to accept the small brass bolt. At this point the studs on the ends of the adjustment screws are in contact with the upper surfaces of the cups in the pins. The collet is now tightened to clamp the support tube. When the system is brought from the laboratory temperature (assumed to be 77°F = 25°C = 298 K) to the temperatures they will have in use, the following temperature expansions and contractions will take place. The shell will be kept at 20 K, and the temperature of the core will range from 100 K to 600 K with a median temperature of 350 K. The top of the 1-in. tube will have the same temperature as the core, and the bottom, in contact with the outer shell, will be at 20 K. Assuming a linear thermal relation, the tube will have an average temperature of 185 K. Thus, compared to the laboratory temperature in the first step, the shell will be cooled 278 K (from 298 K to 20 K), the core will be heated 52 K (from 298 K to 350 K), and the tube will be cooled 113 K (from 298 K to 185 K). The thin-walled stainless steel tube (Type 321) has a coefficient of thermal expansion of 9.3×10^{-6} in./in.°F. The core and the shell of aluminum have a coefficient of thermal expansion of 12.7×10^{-6} in./in.°F. The above-described temperature changes and coefficients of expansion give the following changes in length: The shell will decrease by 0.023 in., the core will expand 0.003 in., and the steel tube will shrink 0.002 in. These changes in length will also change the relative position of the adjustment screws with their studs in the cups of the pins. As the core expands, the pins move up .003 in. relative to the adjustment screws. However, the steel tube is shrinking at the same time, tending to lower the core and screws .002 in. Finally, the shrinkage of the shell to which the adjustment screws are attached lowers

the screws .023 in. relative to the pins. The net result is that the separation between the studs on the adjustment screws and the top of the pins increases to .024 in., placing the studs within .001 in. of the desired center position in the cups in the pins.

Thus, for the proper alignment of the core slug, the only adjustments necessary are the transverse adjustments and the vertical lowering of the core. Thermal expansion will then take care of the desired centering at the median temperature. As the core varies 250 K above and below the median temperature (from 100 K to 600 K), the aluminum will expand or contract .015 in. while the steel changes .002 in., and these variations are accommodated by the ±0.025-in. spacing between the adjustment screw studs and the cups of the locator pins.

Horizontal Core Alignment

To perform horizontal alignment of the core, the outer radiation shield and the aperture plate must be removed. Two long-handled Allen wrenches have been provided in the tool kit to aid in the removal (and later reassembly) of these items. (Note: When these items are reassembled, indium gaskets should be provided as described in the paragraph on "Radiation Shields" on page 98.) Then the cavity-aperture-plug provided in the tool kit is placed into the cavity aperture. This must be done carefully to avoid misalignment of the plug and to prevent damage to the aluminum foil heat insulation. The plug should be placed with the small stud pointing outward. The large disk in the tool kit is then positioned in place of the aperture plate. Following these steps, the stud of the cavity-aperture-plug should be visible inside the hole in this disk.

The axial distance from the 0.0274-in.-diam. aperture in the aperture plate to the 0.200-in.-diam. aperture in the cavity is 0.431 in. Thus the core must be centered 0.431 in. $\times \tan(17.5^\circ) = 0.136$ in. horizontally away from the 0.0274-in.-diam. aperture; this displacement must be in the direction of the off-axis tilt of the core. Furthermore, the 0.0274-in.-diam. aperture is 0.153 in. off center on the aperture plate. Therefore the aperture in the core must be centered $(0.153 - 0.136)$ in. $= 0.017$ in. away from the axis of the cylindrical radiation shield. This 0.017-in. adjustment of the core is off center in the same direction that the aperture is off center on the aperture plate.

Horizontal core alignment is done with the three support-adjustment screws that are threaded through the inner radiation shield cylinder and that have studs on their ends. These studs fit into cups on the ends of pins that have been driven into the core. Each adjustment screw is fitted with a lock nut. A special Allen wrench is provided in the tool kit for turning these screws. The tool kit also provides a pierced socket wrench for the lock nuts; this wrench is pierced to accept the Allen wrench so that each adjustment screw and its lock nut can be controlled in one operation.

When performing horizontal alignment of the core, the three support-adjustment screws should be worked together, maintaining a minimum gap between the core and the screws. When the 0.017-in. off-center alignment is attained, the three screws should be snug against the core. Then, to allow for differential thermal expansion, each screw should be backed off 0.015 in. Since these are 4-40 threads with 0.025 in. per turn, this amounts to about 210° rotation of the screws. After the 0.015-in. corrections are made, the support-adjustment screws should be locked into place with the lock nuts using the wrenches provided.

Core-PRT Bonding

A critical problem in the design and fabrication of a blackbody simulator concerns the physical and thermal bonding of the temperature transducers to the core. The platinum resistance thermometers (PRT's) are 0.600 in. long by 0.060 to 0.070 in. in diameter. The PRT wells drilled in the core are about 0.010 in. larger in diameter than the PRT.

Several mechanical designs were considered. The first was a simple set screw. This idea was not used because differential thermal expansion would provide inadequate contact pressure at one temperature extreme and excessive contact pressure at the other temperature extreme. There was a risk of incorrect temperature readings when the contact pressure was low and a risk of PRT damage when the contact pressure was high.

A second mechanical design involved a spring-wall cylindrical insert. The cylinder was to be made with an ID 0.020 in. larger than the PRT OD, and the cylinder wall was to be 0.020 in. thick. Slots lengthwise on the cylinder would allow strips of the cylinder to be pressed in and out for spring contact to the PRT inside and the PRT well in the core on the outside of the cylinder. This design was not used because of problems with the metal cylinder. Aluminum would probably not retain sufficient spring action after numerous temperature cycles, and a better spring metal such as phosphor bronze would have problems with differential thermal expansion.

Several cements were tested and Sermetel PBX was selected for use with the Improved Blackbody Simulator. Technical data on Sermetel PBX is given in Appendix H. More information about Sermetel PBX can be obtained from

> Teleflex Inc., Sermetel Division
> P.O. Box 187
> North Wales, Pennsylvania 19454
> 215-699-4861

Other cements that were tested include the following:

Omega CC Cement and Omega HT Cement, obtained from

Omega Engineering, Inc.
P.O. Box 4047
Stamford, Connecticut   06907

203-359-1660

Eccobond Solder 58C, obtained from

Emerson and Cuming, Inc.
Gardena, California   90247

213-329-1147

Rosemount Cement 531, obtained from

Rosemount Engineering Company
P.O. Box 35129
Minneapolis, Minnesota   55435

612-941-5560

APPENDIX A

SHAPE THEORY FOR BLACKBODY SIMULATOR CAVITIES

A1. General Theory

The following theory for blackbody simulator cavities expresses all cavity geometry effects in terms of $\int_a d\Omega$, the projected solid angle of the aperture as seen from points on the wall of the cavity. The analysis continues with the development of a simple method for finding approximate values for $\int_a d\Omega$ for different cavity shapes. As a result, this theory provides a valuable tool for the comparison of various candidate cavity shapes for the design of blackbody simulators.

Most previous theories deal with hemispherical cavity emissivity (the ratio of radiant exitance to that of a blackbody). The present theory considers the directional cavity emissivity (the ratio of radiance, or radiant sterance, to that of a blackbody). This is especially important when the blackbody simulator is to be used to fill a wide-angle optical system like a collimator or an integrating sphere. Most previous theories either assume isothermal cavities or make total energy output corrections for temperature gradients; and these corrections are usually expressed as corrections to a calculated effective cavity emissivity. The present theory, on the other hand, shows how cavity temperature variations develop and shows how such temperature variations lead to variations in output energy in different parts of the beam of a wide-angle optical system (e.g., the $f/4$ collimator of the AEDC 7V chamber).

The new theory is illustrated by the particular arrangement shown in Fig. A1.
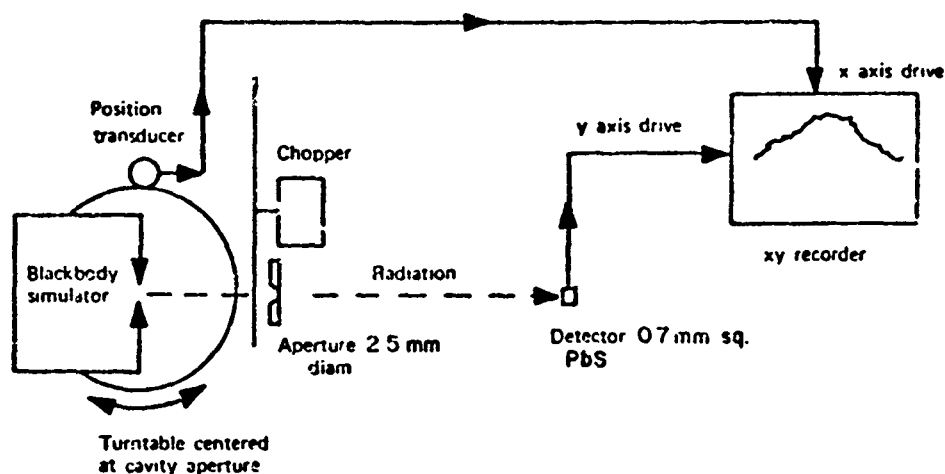
Fig. A1. Experimental arrangement.

107

In this setup, only a narrow pencil of radiation from a small area on the back wall of the cavity is allowed to fall on the detector. As the turntable is rotated, a large part of the cavity wall is sampled sequentially.

Figure A2 shows the geometrical properties of the experimental arrangement.
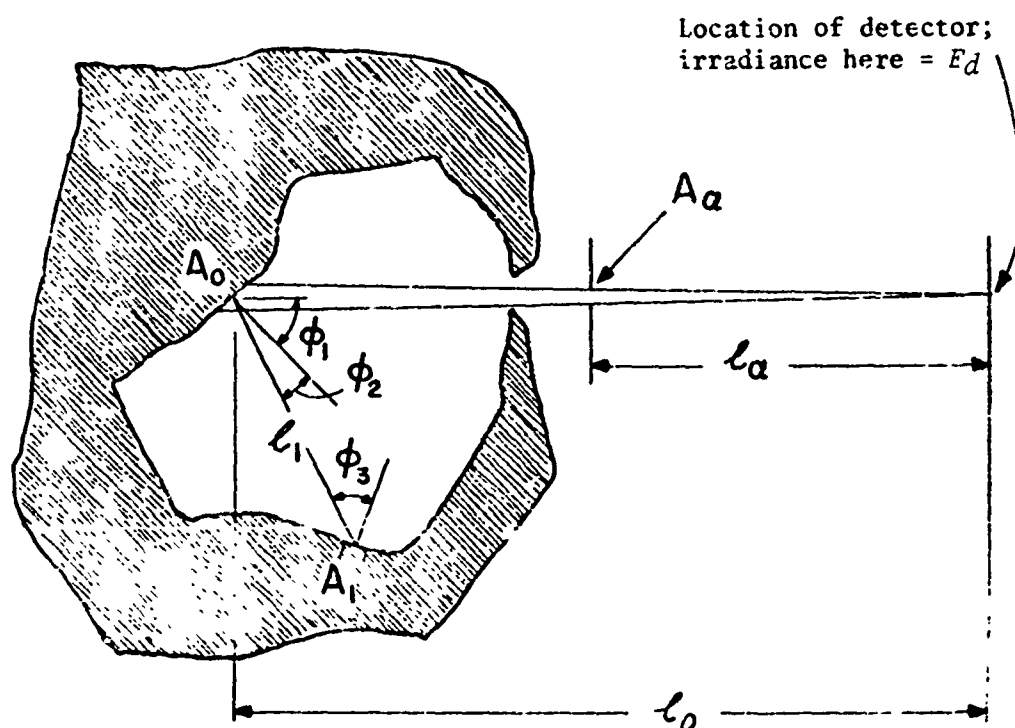
Fig. A2. Geometrical properties of experimental arrangement.

The power at the detector, P_d, is

$$P_d = \int_{A_0}\int_{A_d} L_0\cos\phi_1\cos\phi_d \; \ell_0^{-2} \; dA_d dA_0$$

where

ϕ_d = angle between normal to detector and line from detector to A_0. Here $\phi_d = 0$, so $\cos\phi_d = 1$.

A_d = area of detector

A_0 = area of cavity wall viewed by a point on the detector

L_0 = total radiance (radiant sterance) from A_0 toward detector.

Thus

$$E_d = dP_d/dA_d = \int_{A_0} L_0 \cos\phi_1 \; \ell_0^{-2} \; dA_0$$

= irradiance on detector.

Note in Fig. A2 that

$$\int_{A_0} \cos\phi_1 \; \ell_0^{-2} \; dA_0 = A_\alpha \; \ell_\alpha^{-2}$$

where

A_α = area of system aperture

ℓ_α = distance from system aperture to detector

ℓ_0 = distance from A_0 to detector

ϕ_1 = angle between normal to surface A_0 and line from detector to A_0.

At this point we assume that A_α is so small that L_0 is approximately constant over A_0. If this were not true, we would be required to use a new and and smaller A_α. If a discontinuity in L_0 occurred in A_0 (such as might occur at a cone apex or a cylinder side-back seam), then it would be necessary to divide A_0 into two or more parts such that L_0 would be constant for each part. Thus

$$E_d = L_0 A_\alpha \ell_\alpha^{-2}. \tag{A1}$$

L_0 is the sum of two components,

$$L_0 = L_{00d} + L_{10d} , \qquad (A2)$$

where

L_{00d} = radiance emitted from A_0

= radiance along path from A_0 to detector

= radiance at detector due to emission from A_0

L_{10d} = radiance at the detector due to reflection at A_0 from all the other parts of the cavity and the aperture.

If A_0 is an ideal black surface, then

$$L_{00d} = L^{bb} = M_0 \pi^{-1} = \sigma T_0{}^4 \pi^{-1}$$

where

M_0 = radiant exitance from A_0

σ = Stefan-Boltzmann constant

T_0 = temperature of A_0.

If A_0 is a perfectly diffuse radiator with hemispherical emissivity ϵ, then

$$L_{00d} = \epsilon L^{bb} = \epsilon \sigma T_0{}^4 \pi^{-1}.$$

If A_0 is a real radiator with directional characteristics, then

$$L_{00d} = \epsilon_0(\theta,\phi) L^{bb} = \epsilon_0(\theta,\phi) \sigma T_0{}^4 \pi^{-1}. \qquad (A3)$$

Equations (A1), (A2), (A3) give

$$E_d = \left[\epsilon_0(\theta,\phi) \sigma T_0{}^4 \pi^{-1} + L_{10d} \right] A_\alpha \ell_\alpha{}^{-2}.$$

Recall that

L_{10d} = radiance at the detector due to reflection at A_0 from all other parts of the cavity and the aperture.

Let

f_{10d} = the bidirectional reflectance-distribution function defined in Nicodemus, F. E., Appl. Opt. 4:767, 1965, Eq. (5), with current nomenclature per Nicodemus, F. E., Appl. Opt. 9:1474, 1970.

L_{10} = radiance along the path from dA_1 to A_0

$d\Omega_{10}$ = projected solid angle at A_0 subtended by dA_1.

Then

$$L_{10d} = \int_{2\pi \text{ ster}} f_{10d}\, L_{10}\, d\Omega_{10},$$

in agreement with Eq. (7) of Nicodemus, F. E., Appl. Opt. 4:767, 1965, with nomenclature per Nicodemus, F. E., Appl. Opt. 9:1474, 1970. Note that $d\Omega_{10}$ here corresponds to $d\Omega'$ of the Eq. (7) just cited. Therefore

$$E_d = \left[\epsilon_0(\theta,\phi)\sigma T_0^4 \pi^{-1} + \int_{2\pi \text{ ster}} f_{10d}\, L_{10}\, d\Omega_{10}\right] A_\alpha \ell_\alpha^{-2}.$$

Like L_0, L_{10} is the sum of two components:

L_{10} = $L_{110} + L_{210}$

L_{110} = emission from dA_1 toward A_0

L_{210} = reflection at dA_1 from other parts of the cavity and aperture toward A_0.

We had

$$L_{00d} = \epsilon_0(\theta,\phi)\sigma T_0^4 \pi^{-1},$$

so here

$$L_{110} = \epsilon_1(\theta,\phi)\sigma T_1^4 \pi^{-1};$$

and we had

$$L_{10d} = \int_{2\pi \text{ ster}} f_{10d} L_{10} d\Omega_{10} \, ,$$

so now

$$L_{210} = \int_{2\pi \text{ ster}} f_{210} L_{21} d\Omega_{21} \, .$$

The preceding analysis can be extended to an infinite number of terms by induction. Summarizing all these steps, we have

$$E_d = \left[\varepsilon_0(\theta,\phi)\sigma T_0{}^4\pi^{-1} + \int_{2\pi \text{ ster}} f_{10d} L_{10} d\Omega_{10} \right] A_\alpha \ell_\alpha{}^{-2}$$

$$L_{10} = \left[\varepsilon_1(\theta,\phi)\sigma T_1{}^4\pi^{-1} + \int_{2\pi \text{ ster}} f_{210} L_{21} d\Omega_{21} \right]$$

$$L_{21} = \left[\varepsilon_2(\theta,\phi)\sigma T_2{}^4\pi^{-1} + \int_{2\pi \text{ ster}} f_{321} L_{32} d\Omega_{32} \right]$$

$$\cdot \qquad\qquad \cdot \qquad\qquad \cdot$$
$$\cdot \qquad\qquad \cdot \qquad\qquad \cdot$$
$$\cdot \qquad\qquad \cdot \qquad\qquad \cdot$$

$$L_{(n)(n-1)} = \left[\varepsilon_n(\theta,\phi)\sigma T_n{}^4\pi^{-1} + \int_{2\pi \text{ s er}} f_{(n+1)(n)(n-1)} L_{(n+1)(n)} d\Omega_{(n+1)(n)} \right]$$

$$\cdot \qquad\qquad \cdot \qquad\qquad \cdot$$
$$\cdot \qquad\qquad \cdot \qquad\qquad \cdot$$
$$\cdot \qquad\qquad \cdot \qquad\qquad \cdot \qquad\qquad\qquad \text{(A·4)}$$

A2. A Special Case

The preceding analysis is very general, and should be applicable for any black-body simulator cavity problem. However, use of Eq. (A4) requires detailed information about $\varepsilon(\theta,\phi)$ and $f(\theta,\phi;\theta,\phi)$, and the integrals require a considerable amount of computer time. Therefore, for most practical cases it seems likely that simplifying assumptions will be employed. One special case is of very great importance. We assume

$$\varepsilon_0(\theta,\phi) = \varepsilon_1(\theta,\phi) = \ldots = \varepsilon_n(\theta,\phi) = \varepsilon \tag{A5}$$

$$f_{10d} = f_{210} = \ldots = f_{(n+1)(n)(n-1)} \tag{A5a}$$

$$T_{\text{cavity}} >> T_{\text{outside}} \tag{A5b}$$

This case has the following properties:

(1) The wall surface is Lambertian.

(2) Equation (A4) reduces to a compact form, and it leads to simple solutions to many cavity problems.

(3) The approximations are comparable to those of the best known theories followed today.

(4) Conclusions are in surprising contrast to general practice today.

(5) Results have been verified experimentally.

Equation (A5a) above and Eq. (22) of Nicodemus (Appl. Opt. 4:767, 1965) lead to

$$f_{10d} = f_{210} = f_{(n+1)(n)(n-1)} = \rho\pi^{-1}$$

where

$\rho = 1 - \varepsilon$ (from Kirchhoff's law.)

ρ = hemispherical reflectivity

ε = hemispherical emissivity.

Since direction and hemispherical emissivities are the same for a perfectly diffuse surface, ε is also the constant ε of Eq. (A5).

Therefore,

$$f_{10d} = f_{210} = \ldots = f_{(n+1)(n)(n-1)} = \ldots = (1-\varepsilon)\pi^{-1}. \tag{A6}$$

Thus

$$E_d = A_\alpha \ell_\alpha^{-2} \epsilon \sigma T_0^4 \pi^{-1} + A_\alpha \ell_\alpha^{-2} (1-\epsilon) \pi^{-1} \int_{2\pi \text{ ster}} L_{10} \; d\Omega_{10}$$

but

$$\int_{2\pi \text{ ster}} = \int_{\text{cavit,}} + \int_{\text{aperture}} .$$

From Eq. (A5b) we have, for the <u>aperture</u>,

$$\int_{\text{aperture}} L_{10} \; d\Omega_{10} \simeq 0 .$$

Therefore

$$\int_{2\pi \text{ ster}} L_{10} \; d\Omega_{10} \simeq \int_{\text{cavity}} L_{10} \; d\Omega_{10}$$

and therefore

$$E_d = A_\alpha \ell_\alpha^{-2} \epsilon \sigma T_0^4 \pi^{-1} + A_\alpha \ell_\alpha^{-2} (1-\epsilon) \pi^{-1} \int_{\text{cavity}} L_{10} \; d\Omega_{10} .$$

Over the cavity wall surface, Eq. (A4) gives

$$L_{10} = \epsilon \sigma T_1^4 \pi^{-1} + \int_{\text{cavity}} (1-\epsilon) \pi^{-1} L_{21} \; d\Omega_{21} .$$

Therefore

$$E_d = A_\alpha \ell_\alpha^{-2} \epsilon \sigma T_0^4 \pi^{-1} + A_\alpha \ell_\alpha^{-2} (1-\epsilon) \pi^{-1} \epsilon \sigma \pi^{-1} \int_{\text{cavity}} T_1^4 \; d\Omega_{10}$$

$$+ A_\alpha \ell_\alpha^{-2} (1-\epsilon)^2 \pi^{-2} \int_{\text{cavity}} \int_{\text{cavity}} L_{21} \; d\Omega_{21} \; d\Omega_{10} .$$

From Eqs. (A4) and (A6) we have

$$L_{21} = \epsilon\sigma T_2{}^4\pi^{-1} + \int_{\text{cavity}} (1-\epsilon)\pi^{-1} L_{32} \, d\Omega_{32} \, .$$

Therefore

$$E_d = A_\alpha \ell_\alpha{}^{-2}\epsilon\sigma T_0{}^4\pi^{-1} + A_\alpha \ell_\alpha{}^{-2}(1-\epsilon)\pi^{-1}\epsilon\sigma\pi^{-1} \int_{\text{cavity}} T_1{}^4 \, d\Omega_{10}$$

$$+ A_\alpha \ell_\alpha{}^{-2}(1-\epsilon)^2\pi^{-2}\epsilon\sigma\pi^{-1} \int_{\text{cavity}} \int_{\text{cavity}} T_2{}^4 \, d\Omega_{21} \, d\Omega_{10}$$

$$+ A_\alpha \ell_\alpha{}^{-2}(1-\epsilon)^3\pi^{-3} \int_{\text{cavity}} \int_{\text{cavity}} \int_{\text{cavity}} L_{32}d\Omega_{32}d\Omega_{21}d\Omega_{10}.$$

By repeating the previous argument, we obtain an infinite series solution for E_d:

$$E_d = A_\alpha \ell_\alpha{}^{-2}\epsilon\sigma T_0{}^4\pi^{-1} + A_\alpha \ell_\alpha{}^{-2}(1-\epsilon)\pi^{-1}\epsilon\sigma\pi^{-1} \int_{\text{cavity}} T_1{}^4 \, d\Omega_{10}$$

$$+ A_\alpha \ell_\alpha{}^{-2}(1-\epsilon)^2\pi^{-2}\epsilon\sigma\pi^{-1} \int_{\text{cavity}} \int_{\text{cavity}} T_2{}^4 \, d\Omega_{21} \, d\Omega_{10}$$

$$+ A_\alpha \ell_\alpha{}^{-2}(1-\epsilon)^3\pi^{-3}\epsilon\sigma\pi^{-1} \int_{\text{cavity}} \int_{\text{cavity}} \int_{\text{cavity}} T_3{}^4 d\Omega_{32}d\Omega_{21}d\Omega_{10}$$

$$+ \ldots$$

$$+ A_\alpha \ell_\alpha{}^{-2}(1-\epsilon)^n\pi^{-n}\epsilon\sigma\pi^{-1}$$

$$\cdot \int_{\text{cavity}} \int_{\text{cavity}} \ldots \int_{\text{cavity}} T_n{}^4 d\Omega_{n(n-1)} d\Omega_{(n-1)(n-2)}$$

$$\ldots d\Omega_{21}d\Omega_{10}$$

$$+ \ldots \, .$$

According to one mean value theorem of integral calculus (G. A. Korn and T. M. Korn, *Mathematical Handbook for Scientists and Engineers*, New York, McGraw-Hill, 1968, p. 119), there are some $\overline{T}_1$ and some $\overline{T}_2$ such that

$$\int_{cavity} T_1^4 \, d\Omega_{10} = \overline{T}_1^4 \int_{cavity} d\Omega_{10}$$

and

$$\int_{cavity}\int_{cavity} T_2^4 d\Omega_{21}d\Omega_{10} = \int_{cavity} \overline{T}_2 \int_{cavity} d\Omega_{21}d\Omega_{10}$$

and, according to another mean value theorem (Korn and Korn, p. 119), there is some $\overline{T}_{21}$ such that

$$\int_{cavity} \overline{T}_2 \int_{cavity} d\Omega_{21}d\Omega_{10} = \overline{T}_{21} \int_{cavity}\int_{cavity} d\Omega_{21}d\Omega_{10}.$$

Therefore, there is some $\overline{T}_{n(n-1)\ldots(2)(1)}$ such that

$$\int_{cavity}\int_{cavity} \cdots \int_{cavity} T_n^4 d\Omega_{n(n-1)}d\Omega_{(n-1)(n-2)} \cdots d\Omega_{21}d\Omega_{10}$$

$$= \overline{T}_{n(n-1)\ldots(2)(1)} \int_{cavity}\int_{cavity} \cdots \int_{cavity} d\Omega_{n(n-1)}d\Omega_{(n-1)(n-2)}$$

$$\ldots d\Omega_{21}d\Omega_{10}.$$

$$(A7)$$

Therefore

$$E_d = A_\alpha \ell_\alpha^{-2}\epsilon\sigma T_0^4\pi^{-1} + A_\alpha \ell_\alpha^{-2}(1-\epsilon)\pi^{-1}\epsilon\sigma\overline{T}_1^4\pi^{-1} \int_{cavity} d\Omega_{10}$$

$$+ A_\alpha \ell_\alpha^{-2}(1-\epsilon)^2\pi^{-2}\epsilon\sigma\overline{T}_{21}^4\pi^{-1} \int_{cavity}\int_{cavity} d\Omega_{21}d\Omega_{10}$$

(cont.)

$$+ A_\alpha \ell_\alpha^{-2}(1-\epsilon)^3 \pi^{-3} \epsilon \sigma \overline{T}_{321}{}^4 \pi^{-1} \int_{cavity}\int_{cavity}\int_{cavity} d\Omega_{32}d\Omega_{21}d\Omega_{10}$$

$$+ \ldots$$

$$+ A_\alpha \ell_\alpha^{-2}(1-\epsilon)^n \pi^{-n} \epsilon \sigma \overline{T}_{n(n-1)\ldots(2)(1)}^4 \pi^{-1}$$

$$\cdot \int_{cavity}\int_{cavity}\ldots\int_{cavity} d\Omega_{n(n-1)}d\Omega_{(n-1)(n-2)}\ldots d\Omega_{21}d\Omega_{10}$$

$$+ \ldots . \tag{A8}$$

To evaluate $\int_{cavity}\int_{cavity}\int_{cavity}\ldots\int_{cavity} d\Omega_{n(n-1)}d\Omega_{(n-1)(n-2)}\ldots d\Omega_{21}d\Omega_{10}$,

we first consider the inner integral

$$\int_{cavity} d\Omega_{n(n-1)} = \int_{2\pi\ ster} d\Omega_{n(n-1)} - \int_{aperture} d\Omega_{n(n-1)}.$$

Recall that $d\Omega_{n(n-1)}$ is the projected solid angle at the point $(n-1)$ subtended by an element of area dA at point n. But

$$\int_{2\pi\ ster} d\Omega_{n(n-1)} = \int_0^{2\pi}\int_0^{\pi/2} \sin\theta \cos\theta\, d\theta d\phi$$

in agreement with Eq. (7) and the equations that follow it in Nicodemus (Appl. Opt. 4:767-773, 1965). (Recall that $d\Omega$ here corresponds to $d\Omega'$ of Nicodemus.) Therefore

$$\int_{2\pi\ ster} d\Omega_{n(n-1)} = \pi.$$

Let

$$\int_{\text{aperture}} d\Omega = \int_a d\Omega,$$

where the integration is performed over the <u>cavity</u> aperture. Then

$$\int_{\text{cavity}} d\Omega_{n(n-1)} = \pi - \int_a d\Omega_{n(n-1)}$$

Let

$$B = \int_{\text{cavity}} \int_{\text{cavity}} d\Omega_{n(n-1)} d\Omega_{(n-1)(n-2)}.$$

Then

$$B = \int_{\text{cavity}} \left[\pi - \int_a d\Omega_{n(n-1)} \right] d\Omega_{(n-1)(n-2)}$$

$$= \pi \int_{\text{cavity}} d\Omega_{(n-1)(n-2)} - \int_{\text{cavity}} \int_a d\Omega_{n(n-1)} d\Omega_{(n-1)(n-2)}.$$

The inner integral of the second term of B is the projected solid angle of the aperture as seen from a general point $n-1$. Then this integral becomes a weighting factor for the outer integral, which sums projected solid angles of all small area elements at points $n-1$ as seen from a general point $n-2$. The inner integral will have different values depending on where the point $n-1$ is located. However, as we perform the outer integration, a mean value theorem of integral calculus (Korn and Korn) provides that there is some average value of the inner integral such that

$$\int_{\text{cavity}} \int_a d\Omega_{n(n-1)} \Omega_{(n-1)(n-2)} = \overline{\int_a d\Omega_{n(n-1)}} \int_{\text{cavity}} d\Omega_{(n-1)(n-2)}.$$

Thus B becomes

$$B = \pi \int\limits_{\text{cavity}} d\Omega_{(n-1)(n-2)} - \overline{\int_a d\Omega_{n(n-1)}} \int\limits_{\text{cavity}} d\Omega_{(n-1)(n-2)}$$

$$= \left[\pi - \overline{\int_a d\Omega_{n(n-1)}} \right] \int\limits_{\text{cavity}} d\Omega_{(n-1)(n-2)} \cdot$$

The last integral is evaluated like

$$\int\limits_{\text{cavity}} d\Omega_{n(n-1)} \cdot$$

Therefore,

$$B = \left[\pi - \overline{\int_a d\Omega_{n(n-1)}} \right] \left[\pi - \int_a d\Omega_{(n-1)(n-2)} \right] \cdot$$

Let

$$C = \int\limits_{\text{cavity}} \int\limits_{\text{cavity}} \int\limits_{\text{cavity}} d\Omega_{n(n-1)} d\Omega_{(n-1)(n-2)} d\Omega_{(n-2)(n-3)}$$

$$= \int\limits_{\text{cavity}} B \, d\Omega_{(n-2)(n-3)}$$

$$= \int\limits_{\text{cavity}} \left[\pi - \overline{\int_a d\Omega_{n(n-1)}} \right] \left[\pi - \int d\Omega_{(n-1)(n-2)} \right] d\Omega_{(n-2)(n-3)}$$

by the second mean value theorem used to derive Eq. (A7):

$$C = \left[\pi - \overline{\int_a d\Omega_{n(n-1)(n-2)}}\right] \int_{cavity} \left[\pi - \int_a d\Omega_{(n-1)(n-2)}\right] d\Omega_{(n-2)(n-3)}$$

where

$$\overline{\int_a d\Omega_{n(n-1)(n-2)}}$$

is slightly different from

$$\overline{\int_a d\Omega_{n(n-1)}}$$

to account for the influence of

$$\int_a d\Omega_{(n-2)(n-3)} \cdot$$

Then

$$C = \left[\pi - \overline{\int_a d\Omega_{n(n-1)(n-2)}}\right] \int_{cavity} \int_{cavity} d\Omega_{(n-1)(n-2)} d\Omega_{(n-2)(n-3)} \cdot$$

The double integral can be solved the same way that B was solved. Then

$$C = \left[\pi - \overline{\int_a \Omega_{n(n-1)(n-2)}}\right]\left[\pi - \overline{\int_a d\Omega_{(n-1)(n-2)}}\right]$$

$$\cdot \left[\pi - \int_a d\Omega_{(n-2)(n-3)}\right] \cdot$$

In the same way,

$$\int_{cavity}\int_{cavity}\int_{cavity}\int_{cavity} d\Omega_{n(n-1)}d\Omega_{(n-1)(n-2)(n-3)}d\Omega_{(n-2)(n-3)}d\Omega_{(n-3)(n-4)}$$

$$= \left[\pi - \overline{\int_a d\Omega_{n(n-1)(n-2)(n-3)}}\right]\left[\pi - \overline{\int_a d\Omega_{(n-1)(n-2)(n-3)}}\right]$$

$$\cdot \left[\pi - \overline{\int_a d\Omega_{(n-2)(n-3)}}\right]\left[\pi - \overline{\int_a d\Omega_{(n-3)(n-4)}}\right]$$

and in general

$$\int_{cavity}\cdots\int_{cavity} d\Omega_{n(n-1)}\ldots d\Omega_{10}$$

$$= \left[\pi - \overline{\int_a d\Omega_{n(n-1)(n-2)(n-3)\ldots(2)(1)}}\right]$$

$$\cdot \left[\pi - \overline{\int_a d\Omega_{(n-1)(n-2)(n-3)\ldots(2)(1)}}\right]\cdots$$

$$\cdot \left[\pi - \overline{\int_a d\Omega_{321}}\right]\left[\pi - \overline{\int_a d\Omega_{21}}\right]\left[\pi - \overline{\int_a d\Omega_{10}}\right] \ .$$

Note that the average integrals are all approximately equal, and there is *some* average integral

$$\overline{\int_a d\Omega_n}$$

such that

$$\left[\pi - \overline{\int_a d\Omega_{n(n-1)(n-2)\ldots21}} \right] \left[\pi - \overline{\int_a d\Omega_{(n-1)(n-2)\ldots21}} \right] \cdots$$

$$\cdot \left[\pi - \overline{\int_a d\Omega_{21}} \right] = \left[\pi - \overline{\int_a d\Omega_n} \right]^{n-1} .$$

Therefore

$$\int_{cavity} \int_{cavity} \cdots \int_{cavity} d\Omega_{n(n-1)} d\Omega_{(n-1)(n-2)} \cdots d\Omega_{21} d\Omega_{10}$$

$$= \left[\pi - \overline{\int_a d\Omega_n} \right]^{n-1} \left[\pi - \int_a d\Omega_{10} \right] ,$$

where the first integral is an average integral evaluated over the aperture from some average point within the cavity and the second integral is the projected solid angle of the aperture as seen from point O in Fig. A2. Thus, Eq. (A8) becomes

$$E_d = A_\alpha \ell_\alpha^{-2} \epsilon\sigma T_0^4 \pi^{-1} + A_\alpha \ell_\alpha^{-2}(1-\epsilon)\pi^{-1}\epsilon\sigma\overline{T}_1^4 \pi^{-1} \left[\pi - \int_a d\Omega_{10} \right]$$

$$+ A_\alpha \ell_\alpha^{-2}(1-\epsilon)^2 \pi^{-2} \epsilon\sigma\overline{T}_{21}^4 \pi^{-1} \left[\pi - \overline{\int_a d\Omega_2} \right] \left[\pi - \int_a d\Omega_{10} \right]$$

$$+ A_\alpha \ell_x^{-2}(1-\epsilon)^3 \pi^{-3} \epsilon\sigma\overline{T}_{321}^4 \pi^{-1} \left[\pi - \overline{\int_a d\Omega_3} \right]^2 \left[\pi - \int_a d\Omega_{10} \right]$$

$$+ \ldots$$

$$+ A_\alpha \ell_\alpha^{-2}(1-\epsilon)^n \pi^{-n} \epsilon\sigma\overline{T}_{n(n-1)\ldots4321}^4 \pi^{-1} \left[\pi - \overline{\int_a d\Omega_n} \right]^{n-1} \left[\pi - \int_a d\Omega_{10} \right]$$

$$+ \ldots \ . \tag{A9}$$

The $\overline{T}_{n(n-1)\ldots21}$ are average temperatures selected so that Eq. (A7) would be true. Therefore the n different $\overline{T}_{n(n-1)\ldots21}$ of Eq. (A9) will be about the same value, but slightly different. However, for any set of values for all the quantities in Eq. (A9) there is some quantity T_m such that all the $\overline{T}_{n(n-1)\ldots21}$ can be replaced by T_m and Eq. (A9) will still be valid.

Similarly, the different $\overline{\int_a d\Omega_i}$ can all be replaced by a single new average integral $\overline{\int_a d\Omega}$.

Therefore,

$$E_d \;=\; A_\alpha \ell_\alpha^{-2} \epsilon\sigma T_0^{\,4} \pi^{-1}$$

$$+\; A_\alpha \ell_\alpha^{-2}(1-\epsilon)\pi^{-1}\epsilon\sigma T_m^{\,4}\pi^{-1}\left[\pi - \int_a d\Omega_{10}\right]\sum_{i=0}^{\infty}(1-\epsilon)^i\pi^{-i}$$

$$\cdot\left[\pi - \overline{\int_a d\Omega}\right]^i .$$

But

$$\sum_{i=0}^{\infty} x^i \;=\; 1 + x + x^2 + \ldots + x^n + \ldots \;=\; (1-x)^{-1}$$

when $-1 < x < 1$, and this is always true in the present case. Therefore,

$$E_d \;=\; A_\alpha \ell_\alpha^{-2}\epsilon\sigma T_0^{\,4}\pi^{-1}$$

$$+\; A_\alpha \ell_\alpha^{-2}(1-\epsilon)\pi^{-1}\epsilon\sigma T_m^{\,4}\pi^{-1}\left[\pi - \int_a d\Omega_{10}\right]$$

$$\cdot\left\{1 - (1-\epsilon)\pi^{-1}\left[\pi - \overline{\int_a d\Omega}\right]\right\}^{-1} .$$

The term within braces is equivalent to

$$\left[1 - 1 + \epsilon + (1-\epsilon)\pi^{-1}\overline{\int_a d\Omega}\right]^{-1} \;=\; \epsilon^{-1}\left[1 + \frac{1-\epsilon}{\pi\epsilon}\overline{\int_a d\Omega}\right]^{-1} .$$

Therefore

$$E_a = A_\alpha \ell_\alpha^{-2} \epsilon \sigma T_0^4 \pi^{-1}$$

$$+ A_\alpha \ell_\alpha^{-2} \sigma T_m^4 \pi^{-1} \left[1 - \pi^{-1} \int_a d\Omega_{10} \right] (1-\epsilon) \left[1 + \frac{1}{\pi\epsilon} \overline{\int_a d\Omega} \right]^{-1}.$$

$$(A10)$$

The second term has the form

$$\alpha(1-\beta)(1-\epsilon)(1+\gamma)^{-1}$$

but

$$(1+\gamma)^{-1} = \frac{1+\gamma-\gamma}{1+\gamma} = 1 - \gamma(1+\gamma)^{-1}.$$

Therefore the second term becomes

$$\alpha(1-\beta)(1-\epsilon) - \alpha(1-\beta)(1-\epsilon)\gamma(1+\gamma)^{-1}$$

$$= \alpha(1-\epsilon) - \alpha\beta(1-\epsilon) - \alpha(1-\beta)(1-\epsilon)\gamma(1+\gamma)^{-1}.$$

So Eq. (A10) becomes

$$E_d = A_\alpha \ell_\alpha^{-2} \epsilon \sigma T_0^4 \pi^{-1} + A_\alpha \ell_\alpha^{-2} \sigma T_m^4 \pi^{-1} (1-\epsilon)$$

$$- A_\alpha \ell_\alpha^{-2} \sigma T_m^4 \pi^{-1} (1-\epsilon) \pi^{-1} \int_a d\Omega$$

$$- A_\alpha \ell_\alpha^{-2} \sigma T_m^4 \pi^{-1} (1-\epsilon) \left[1 - \pi^{-1} \int_a d\Omega \right] \frac{1-\epsilon}{\pi\epsilon} \overline{\int_a d\Omega} \left[1 + \frac{1-\epsilon}{\pi\epsilon} \overline{\int_a d\Omega} \right]^{-1}.$$

$$(A11)$$

But it is difficult to measure different T_0 values over the cavity surface. So let us measure the temperature at some points within the cavity core such as T_t points illustrated in Fig. A3.
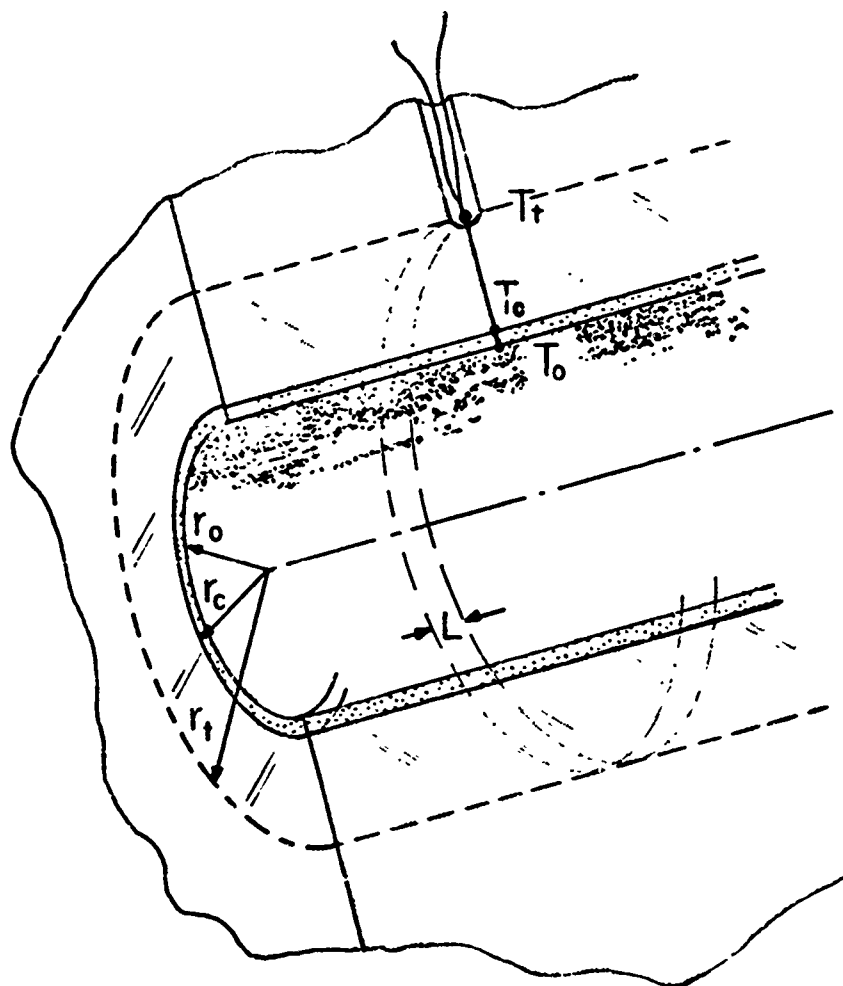
Fig. A3. T_0, T_t Geometry.

Then

$$T_0 = T_t + \Delta T.$$

Note that in most cases $\Delta T < 0$. Then the first term in Eq. (A11) becomes

$$A_\alpha \ell_\alpha^{-2} \epsilon \sigma (T_t + \Delta T)^4 \pi^{-1} = A_\alpha \ell_\alpha^{-2} \epsilon \sigma T_t^4 \pi^{-1} (1 + \Delta T/T_t)^4$$

$$= A_\alpha \ell_\alpha^{-2} \epsilon \sigma T_t^4 \pi^{-1} (1 + 4\Delta T/T_t). \qquad (A12)$$

We proceed to evaluate ΔT by a radiation-conduction heat balance technique. First, observe that for good blackbody simulator design the core material must have high thermal conductivity to minimize thermal gradients while the cavity wall surface must have high emissivity. In general, no single material has both these properties, so in general good cavity design calls for a metal core with an internal surface coating.

Note that most blackbody simulator cavities are symmetrical about a cavity axis. We will proceed with our analysis making this assumption, and recognize that the argument can be modified later to embrace most nonsymmetrical cavity shapes.

Assume that the most significant component of the thermal gradient is radial. This will be a fairly valid assumption for most blackbody simulator cavities. For thermal conductivity,

$$\frac{dQ}{dt} = P = -KA(dT/dx)$$

$\qquad\qquad$ = rate of transfer of heat energy

$\qquad\qquad$ = power

K = coefficient of thermal conductivity

A = a. · ⌐

T = temperature

x = displacement.

Here, since we assume only radial temperature gradients, we may write dT/dr.

Let L be a small finite axial distance and r be any radius such that

$$r_0 \leq r \leq r_t.$$

Then

$$A = 2\pi r L$$

$$P = -K(2\pi r L)(dT/dr)$$

$$P\,dr/r = -2\pi KL(dT)$$

$$P\ln(r)\Big]_{r_0}^{r_c} = -2\pi K_{0c}LT\Big]_{T_0}^{T_c} \quad \text{and} \quad P\ln(r)\Big]_{r_c}^{r_t} = -2\pi K_{ct}LT\Big]_{T_c}^{T_t} \ .$$

Therefore

$$P\ln(r_c/r_0) = -2\pi K_{0c}L(T_c - T_0)$$

$$P\ln(r_t/r_c) = -2\pi K_{ct}L^{m}(- T_c)$$

and therefore

$$T_c - T_0 = -(P/2\pi L)\ln(r_c/r_0)K_{0c}^{-1}$$

$$T_t - T_c = -(P/2\pi L)\ln(r_t/r_c)K_{tc}^{-1}$$

and therefore

$$\Delta T = T_0 - T_t = -\big[(T_c - T_0) + (T_t - T_c)\big]$$

$$= (P/2\pi L)\big[\ln(r_c/r_0)K_{0c}^{-1} + \ln(r_t/r_c)K_{tc}^{-1}\big] \ .$$

P/L is the power per unit length conducted in the direction of increasing r. The actual heat flow is in the opposite direction, toward the cavity surface, so P/L is negative. If we redefine P to be a positive quantity, we will have a new negative expression that we can balance against the radiated power:

$$\Delta T = -(P/2\pi L)\left[\ln(r_c/r_0)K_{0c}^{-1} + \ln(r_t/r_c)K_{tc}^{-1}\right].$$

Recall that $\Delta T = T_0 - T_t$ in general is less than zero. The quantity P in the above equation must equal the radiated power, which we may determine from Eq. (7.7) of M. A. Bramson (*Infrared Radiation*, Plenum Press, 1968, p. 214):

$$\text{flux} = \sigma(T_1^4 - T_2^4)\int_{S_1}\int_{S_2}(\cos\phi_1\cos\phi_2/\pi r^2)ds_1 ds_2 .$$

Converting from the terminology of Bramson to that of the present report, we have

flux becomes radiated power

T_1 becomes T_0

T_2 is neglected due to Eq. (A5b)

$\int_{S_1} ds_1$ becomes $2\pi r_0 L$ (as seen in Fig. A3)

$\int_{S_2}(\cos\phi_1\cos\phi_2/r^2)ds_2$ becomes $\int_a d\Omega$, the projected solid angle

We must add a factor of ε to account for a nonideal radiater. Then the radiated power becomes

$$P = \varepsilon\sigma T_0^4 2\pi r_0 L \int_a d\Omega/\pi.$$

This value of P must be equal to that in the last expression for ΔT, so, substituting into the ΔT equation, we have

$$\Delta T = -\varepsilon\sigma T_0^4\pi^{-1}r_0\left[\ln(r_c/r_0)K_{0c}^{-1} + \ln(r_t/r_c)K_{ct}^{-1}\right]\int_a d\Omega. \quad \text{(A13)}$$

Note that Eq. (A13) gives a value for the correction ΔT. Since this is a correction term, we will leave T in the simpler form T_0 instead of converting it to the more complicated form T_t.

Equations (A11), (A12), and (A13) give

$$E_d = A_\alpha \ell_\alpha^{-2} \sigma T_t^4 \pi^{-1} \epsilon + A_\alpha \ell_\alpha^{-2} \sigma T_m^4 \pi^{-1} (1-\epsilon)$$

$$- A_\alpha \ell_\alpha^{-2} \sigma T_m^4 \pi^{-1} (1-\epsilon) \pi^{-1} \int_a d\Omega_{10}$$

$$- A_\alpha \ell_\alpha^{-2} \sigma T_t^4 \pi^{-1} \left[4\epsilon^2 \sigma T_0^4 T_t^{-1} r_0 \left[\ln(r_c/r_0) K_{0c}^{-1} \right. \right.$$
$$\left. \left. + \ln(r_t/r_c) K_{ct}^{-1} \right] \pi^{-1} \right] \int_a d\Omega_{10}$$

$$- A_\alpha \ell_\alpha^{-2} \sigma T_m^4 \pi^{-1} (1-\epsilon)^2 \epsilon^{-1} \pi^{-1} \overline{\int_a d\Omega}$$

$$\cdot \left[1 - \pi^{-1} \int_a d\Omega_{10} \right] \left[1 + \frac{1-\epsilon}{\pi\epsilon} \overline{\int_a d\Omega} \right]^{-1}.$$

(A14)

A3. Evaluation of $\int_a d\Omega$

Equation (A14) shows that the analysis of this report separates all the cavity geometry effects into the single expression

$$\int_a d\Omega = \int_a \cos\phi_1 \cos\phi_2 \, r^{-2} \, ds. \tag{A15}$$

This integral will be solved by assuming that several of the integrand quantities are constant over the aperture:

$$\left. \begin{array}{l} r \simeq \text{constant} \\ \phi_1 \simeq \text{constant} \\ \phi_2 \simeq \text{constant} \end{array} \right\} \quad \text{over} \int_a ds. \tag{A16}$$

These assumptions are fairly accurate for small apertures and deep cavity locations, but they are less reliable for large apertures and for points near the aperture. However, the resulting equations are so simple and useful that we will develop this approximate theory in considerable detail. We must always keep in mind the limitations imposed by these assumptions. In particular, we must remember that the resulting equations become rather poor approximations along the cavity wall near the aperture.

As a result of these assumptions equation (A15) becomes:

$$\int_a d\Omega = \cos\phi_1 \cos\phi_2 A_a r^{-2} \tag{A17}$$

General Cavity Shape

Let us now express Eq. (A17) in terms of a geometry that is very useful for many cavity studies (see Fig. A4):

$\cos\varphi_2 = z/r$

$\varphi_1 = \varphi_3 + u$

$\cos\varphi_1 = \cos\varphi_3 \cos u - \sin\varphi_3 \sin u,$

but

$\cos\varphi_3 = y/r$

$\sin\varphi_3 = z/r;$
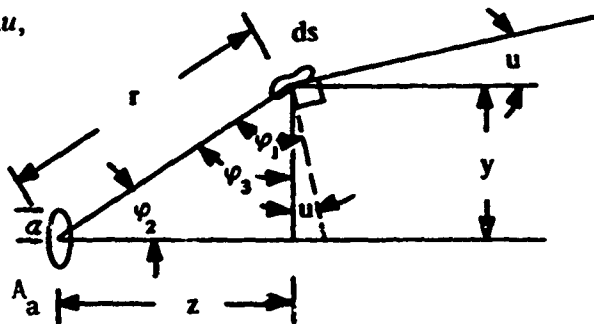
Fig. A4 General cavity geometry.

therefore

$$\cos\varphi_1 = (y \cos u - z \sin u)/r$$

and

$$\int_a d\Omega = (y \cos u - z \sin u)z A_a /r^4.$$

Let us restrict ourselves to circular apertures of radius a. Then

$$A_a = \pi a^2$$

and

$$\pi^{-1} \int_a d\Omega = (y \cos u - z \sin u) z a^2 /r^4. \qquad \text{(general design equation)} \tag{A18}$$

Equation (A18) is a general design equation for blackbody simulators.
We will see that this equation can be applied rather easily to the standard
cavity shapes to reveal a number of interesting properties of these cavities.

Spherical Cavity

Figure A5 shows

$$y = R \cos u$$
$$z = R(1 - \sin u).$$

Fig. A5   Spherical cavity.

By substituting into Eq. (A18) we have

$$\int_a d\Omega = [(R \cos u) \cos u - R(1 - \sin u) \sin u] za^2/r^4$$

$$= R(\cos^2 u + \sin^2 u - \sin u) za^2/r^4$$

$$= R(1 - \sin u) za^2/r^4$$

$$= z^2 a^2/r^4.$$

However, in triangles ABC and ADO in Fig. A5.

$$z/r = \tfrac{1}{2} r/R;$$

therefore

$$z^2/r^4 = 1/4R^2$$

and

$$\pi^{-1} \int_a d\Omega = a^2/4R^2. \quad \text{(sphere)} \tag{A19}$$

Note that the position variables r, y, z, φ_1, φ_2, and u do not appear in Eq. (A19) a constant for all positions within the cavity.

Conical Cavity

Figure A6 shows

$$y = a - az/h$$
$$\cos u = h/(h^2 + a^2)^{1/2}$$
$$\sin u = -a/(h^2 + a^2)^{1/2}.$$
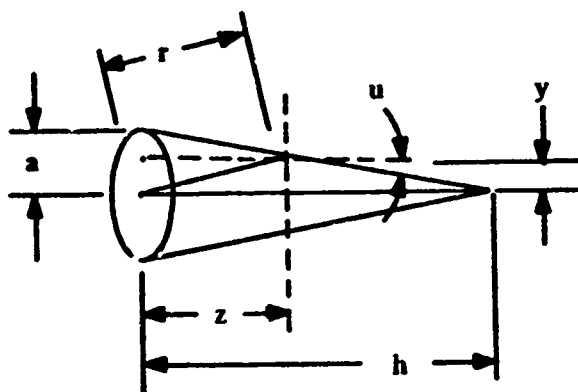
Fig. A6 · **Conical cavity.**

By substituting into Eq. (A18) we have

$$
\begin{aligned}
\pi^{-1} \int_a d\Omega &= \left\{ [(a - az/h)h/(h^2 + a^2)^{1/2}] + za/(h^2 + a^2)^{1/2} \right\} za^2/r^4 \\
&= [ah/(h^2 + a^2)^{1/2}] za^2/r^4 \\
&= za^3/r^4(1 + a^2/h^2)^{1/2}.
\end{aligned}
$$

therefore

$$\pi^{-1} \int_a d\Omega = za^3(1 + a^2/h^2)^{-\frac{1}{2}}[z^2 + a^2(1 - z/h)^2]^{-2}. \quad \text{(cone)} \tag{A20}$$

Note the difference between Eqs. (A19) & (A20). For Eq. (A20), $\int_a d\Omega$ varies sharply with position, and it is very learge near the aperture. This corresponds to the observed temperature drop near the mouth of a conical cavity blackbody simulator.

Cylindrical Cavity

For the side wall, Fig A7 shows

$y = a$
$u = 0$
$\cos u = 1$
$\sin u = 0.$
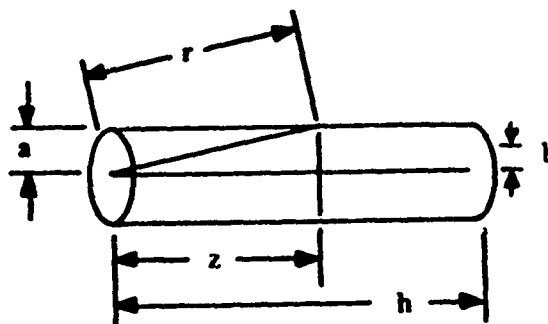
Fig. A7 **Cylindrical cavity.**

By substituting into Eq. (A18) we have

$$\pi^{-1} \int_a d\Omega = (a - 0)za^2/r^4;$$

therefore

$$\pi^{-1} \int_a d\Omega = za^3(z^2 + a^2)^{-2}. \quad \text{(cylinder side wall)} \tag{A21}$$

For the back wall, Fig. A7 shows

$u = -\pi/2$
$\sin u = -1$
$\cos u = 0$
$z = h.$

By substituting into Eq. (A18) we have

$$\pi^{-1} \int_a d\Omega = (0 + h)za^2/r^4;$$

therefore

$$\pi^{-1} \int_A d\Omega = h^2 a^2 (h^2 + b^2 \int^2 \quad \text{(cylinder back wall)} \tag{A22}$$

where b is the distance off axis of the area element ds_1.

Compare Eqs. (A19) through (A22). Only Eq. (A19) for the spheres has $\int_a d\Omega$ independent of position. Both the cone and the cylinder side walls have large values of $\int_a d\Omega$ near the aperture. Thus both Eqs. (A20) and (A21) predict large heat losses near the mouth of conical and cylindrical cavity blackbody simulators. These large heat losses correspond to experimentally observed temperature drops.

At the junction of the cylinder back and side z=h and b=a. Eqs. (A21) and (A22) then become

$$\pi^{-1} \int_a d\Omega = a^3 h (h^2 + a^2 \int^2 \quad \text{(cylinder side wall at back)} \tag{A21a}$$

$$\pi^{-1} \int_a d\Omega = a^2 h^2 (h^2 + a^2 \int^2. \quad \text{(cylinder back wall at side)} \tag{A22a}$$

These equations show that the side wall has less heat loss by a ratio of a:h compared to the back wall at the junction where they meet. Conduction heat balancing then slightly lowers the temperature of the side wall at this junction and slightly raises the temperature of the back wall. These results predicted by Eqs. (A21a) & (A22a) agree with the experimentally observed phenomenon that blackbody simulators with cylindrical cavities have their highest temperatures along the side wall near the back but not at the back. Figure A8 shows the temperature distribution.

Temperatures somewhat below the highest

Lowest temperatures

Highest temperature
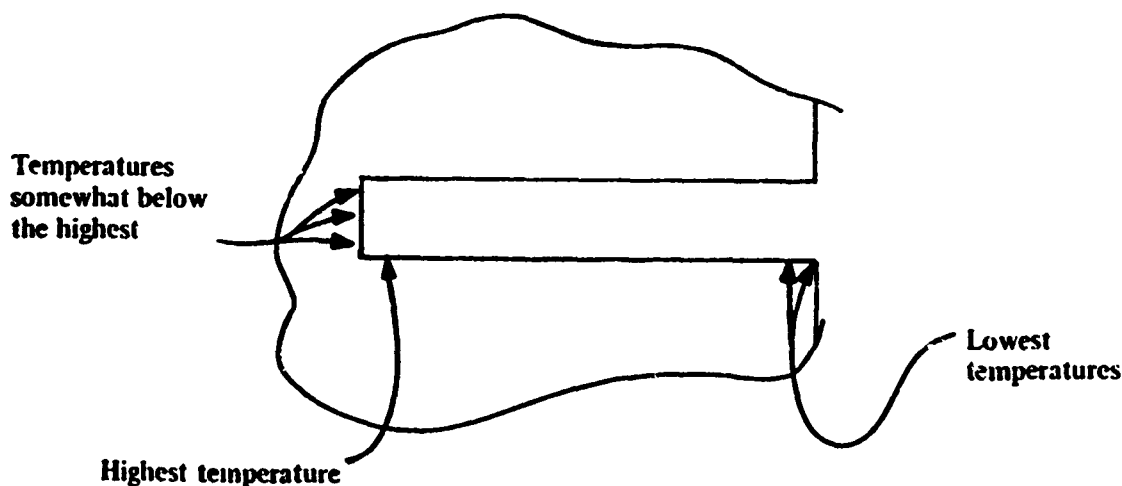
Fig. A8 Cylindrical cavity temperature distribution.

Cylinder Plus Cone

The cylindrical side wall can be treated by the analysis of the previous section. For the cone, Fig. A9 shows

$$y = a - (z - l)a/h$$
$$\cos u = h/(a^2 + h^2)^{1/2}$$
$$\sin u = -a/(a^2 + h^2)^{1/2}.$$
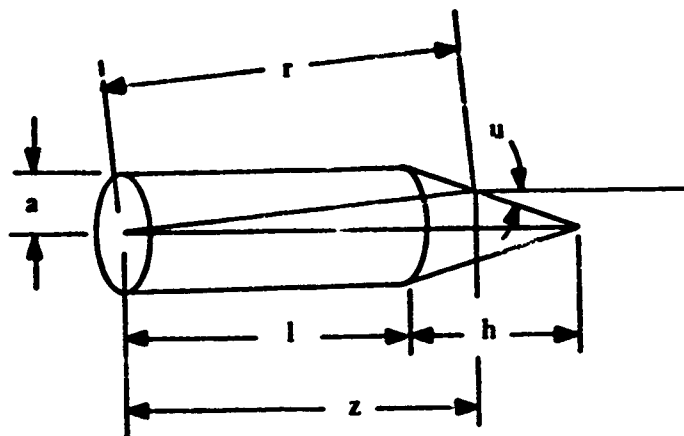
Fig. A9   Cylinder plus cone.

By substituting into Eq. (A18) we have

$$\pi^{-1} \int_a d\Omega = \left(\left\{ [a - (z - l)a/h] h/(a^2 + h^2)^{1/2} \right\} + za/(a^2 + h^2)^{1/2} \right) za^2/r^4$$

$$= [(ah + al)/(a^2 + h^2)^{1/2}] za^2/r^4 ;$$

therefore

$$\pi^{-1} \int_a d\Omega = (h + l)za^3(a^2 + h^2)^{-1/2} \left\{ z^2 + [a - (z - l)a/h]^2 \right\}^{-2}.$$

(cone at rear of cylinder plus cone)   (A23)

Comparison of Several Shapes

The equations for the sphere, cone, cylinder side wall, cylinder back wall, and cone at rear of cylinder plus cone are

$$\pi^{-1} \int_a d\Omega \quad = \quad a^2/4R^2 \qquad\qquad \text{(sphere)} \qquad\qquad \text{(A19)}$$

$$\pi^{-1} \int_a d\Omega \quad = \quad za^3(1 + a^2/h^2)^{-\frac{1}{2}}[z^2 + a^2(1 - z/h)^2]^2 \qquad \text{(cone)} \qquad \text{(A20)}$$

$$\pi^{-1} \int_a d\Omega \quad = \quad za^3(z^2 + a^2)^2 \qquad \text{(cylinder side wall)} \qquad \text{(A21)}$$

$$\pi^{-1} \int_a d\Omega \quad = \quad h^2 a^2 (h^2 + b^2)^2 \qquad \text{(cylinder back wall)} \qquad \text{(A22)}$$

$$\pi^{-1} \int_a d\Omega \quad = \quad (h + l)za^3(a^2 + h^2)^{-\frac{1}{2}}\{z^2 + [a - (z - l)a/h]^2\}^{-2} \qquad \begin{array}{l}\text{(cone at rear} \quad \text{(A23)} \\ \text{of cylinder} \\ \text{plus cone)} \end{array}$$

$$\pi^{-1} \int_a d\Omega \quad = \quad (1 + l/h)za^3(1 + a^2/h^2)^{-\frac{1}{2}}\{z^2 + a^2[1 - (z - l)/h]^2\}^{-2}. \qquad \text{(A23a)}$$

These equations may be used to compare the different cavity designs. Note that, for the cylinder plus cone, when h is very small the design resembles a simple cylinder and $z \simeq l$ in Eq. (A23), so $[a - (z-l)a/h] = b$. Thus, Eq. (A23) becomes

$$\pi^{-1} \int_a d\Omega \quad = \quad lza^3(a^2)^{-\frac{1}{2}}[l^2 + b^2]^{-2} \quad = \quad l^2 a^2 (l^2 + b^2)^{-2},$$

but l in Eq. (A23) is the same as h in Eq. (A22), so Eq. (A23) reduces to Eq. (A22). For the cylinder plus cone, when l is very small, the design resembles a simple cone, and Eq. (A23a) reduces to Eq. (A20).

In the next section of this paper, Eqs. (A21) and (A23a) are compared to the reentrant cone equations.

Reentrant Cone

The reentrant cone is shown in Fig. A10 Blackbody simulators of this design are given special mention by two of the leading books in the infrared field: R. D. Hudson, Jr., *Infrared System Engineering*, Wiley, 1969, p. 73, and M. R. Holter, S. Nudelman, G. H. Suits, W. L. Wolfe, and G. J. Zissis, *Fundamentals of Infrared Technology*, Macmillan, 1962, p. 44.
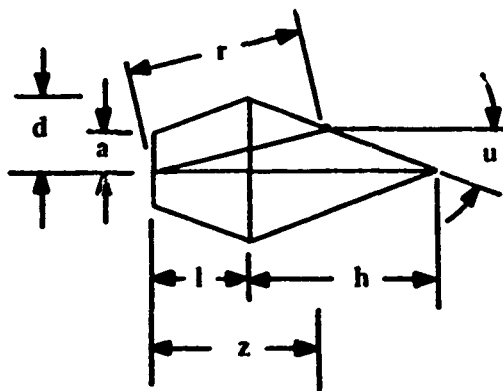
Fig. A10   **Reentrant cone.**

Eq. (A18) may be used to compare variations of this design with each other and with the other configurations of this proposal.

For the rear cone in Fig. A10

$$y = d - (z - l)d/h$$
$$\cos u = h/(d^2 + h^2)^{1/2}$$
$$\sin u = -d/(d^2 + h^2)^{1/2}.$$

By substituting into Eq. (A18) we have

$$\pi^{-1} \int_a d\Omega = za^2/r^4 \left\{ [d - (dz/h) + (dl/h)] [h/(d^2 + h^2)^{1/2}] \right.$$

$$\left. + [dz/(d^2 + h^2)^{1/2}] \right\};$$

therefore

$$\pi^{-1} \int_a d\Omega = (za^2/r^4)[(dh + dl)/(d^2 + h^2)^{\frac{1}{2}}]$$

$$= (a^2 dz/r^4)[(h + l)/(d^2 + h^2)^{\frac{1}{2}}]. \quad \text{(rear cone of reentrant cone)} \quad (A24)$$

For the front truncated cone in Fig. A10

$$y = a + (z/l)(d - a)$$
$$\cos u = h/(d^2 + h^2)^{\frac{1}{2}}$$
$$\sin u = d/(d^2 + h^2)^{\frac{1}{2}}.$$

By substituting into Eq. (A18) we have

$$\pi^{-1} \int_a d\Omega = (za^2/r^4)\left\{[a + (z/l)(d - a)][h/(d^2 + h^2)^{\frac{1}{2}}] \right.$$

$$\left. - [zd/(d^2 + h^2)^{\frac{1}{2}}]\right\};$$

therefore

$$\pi^{-1} \int_a d\Omega = (za^2/r^4)[ah + (zdh/l) - (zah/l) - zd]/(d^2 + h^2)^{\frac{1}{2}}.$$

$$\text{(front truncated cone of reentrant cone)} \quad (A25)$$

Let us rearrange Eqs. (A24) & (A25) First note that $d > a$, so we can let $d = ka$ for some $k > 1$. Then Eq. (A24) becomes

$$\pi^{-1} \int_a d\Omega = ka^3 z(1 + l/h)(1 + k^2 a^2/h^2)^{-\frac{1}{2}}\left\{z^2 + k^2 a^2[1 - (z - l)/h]^2\right\}^{-2}. \quad (A24a)$$

By comparing Eq. (A24a) with (A23a) we see that the reentrant cone has

$$k(1 + a^2/h^2)^{\frac{1}{2}}(1 + k^2 a^2/h^2)^{-\frac{1}{2}}\left\{z^2 + a^2[1 - (z - l)/h]^2\right\}^2\left\{z^2 + k^2 a^2[1 - (z - l)/h]\right\}^{-2}$$

times as large an aperture effect as the cylinder plus cone, and this is approximately equal to k when $a \ll h$ and $a \ll z$. This suggests that the cylinder plus cone may have a more uniform $\int_a d\Omega$ than the reentrant cone. Further study of this comparison is warranted.

When we modify Eq. (A25) by letting $d = ka$, we obtain

$$\pi^{-1} \int_a d\Omega = za^2[ha + (zahk/l) - (zah/l) - zka]\left\{z^2 + [a + (z/l)(ka - a)]^2\right\}^{-2}(h^2 + k^2 a^2)^{-\frac{1}{2}}.$$

$$(A25a)$$

If the cone angles of the rear cone and the front truncated cone are the same, then by similar triangles shown in Fig. A11

$$(h - l)/a = h/d = h/ka; \qquad (A26)$$

therefore

$$hk - lk = h$$

and

$$hk - h - lk = 0.$$
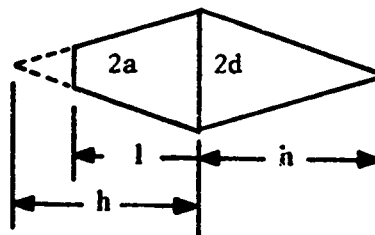
Fig. A11. Eq. (A26) geometry.

Multiplying by za/l we obtain

$$(zahk/l) - (zah/l) - zak = 0;$$

therefore Eq. (A25a) becomes

$$\pi^{-1} \int_a d\Omega = za^2 ha(h^2 + k^2 a^2)^{-\frac{1}{2}} \{z^2 + a^2[1 + (k - 1)z/l]^2\}^{-2}$$

or

$$\pi^{-1} \int_a d\Omega = za^3 (1 + k^2 a^2/h^2)^{-\frac{1}{2}} \{z^2 + a^2[1 + (k - 1)z/l]^2\}^{-2}.$$

(front truncated cone of reentrant cone)   (A25b)

Comparing Eq. (A25b) with Eq. (A21), we see that they are quite similar; the reentrant cone has a smaller variation in directional emissivity by the factor

$$(z^2 + a^2)^2 \{z^2 + a^2[1 + (k - 1)z/l]^2\}^{-2} (1 + k^2 a^2/h^2)^{-\frac{1}{2}}.$$

This is consistent with Hudson's statement on page 73 of his book that the reentrant cone should be less susceptible to excessive cooling at its open end compared to a conventional cone. However, when h is much larger than ka and $(k - 1)z/l$ is small, this effect is not very great. As noted above, further comparison of the reentrant cone and the cone plus cylinder is warranted.

Reentrant Cone Variations

There are several interesting variations on the reentrant cone. We are not sure whether these designs have any merit, but they are examples of how Eq. (A18) can be used to study blackbody simulator designs. Consider Fig. A10 and Eq. (A24) when $\int_a d\Omega$ at the apex of the rear cone is equal to $\int_a d\Omega$ at the junction of the front and rear cones. This condition is an approach toward improving the uniformity of the directional emissivity of conical cavities.

$$z = r = h + l \qquad \text{at apex}$$

$$\left. \begin{array}{l} z = l \\ r = (d^2 + l^2)^{\frac{1}{2}} \end{array} \right\} \qquad \text{at junction}$$

therefore Eq. (A24) becomes

$$[\pi^{-1}\int_a d\Omega]_{apex} = [(a^2 d)(h + l)/(h + l)^4][(h + l)/(d^2 + h^2)^{\frac{1}{2}}]$$

$$[\pi^{-1}\int_a d\Omega]_{junction} = [a^2 dl/(d^2 + l^2)^2][(h + l)/(d^2 + h^2)^{\frac{1}{2}}]$$

and

$$\frac{1}{(h + l)^3} = \frac{l}{(d^2 + l^2)^2} .$$

Let us solve this for l and h as a function of h/l for the normalized case where $d = 1$:

$$l = [(1 + h/l)^{3/2} - 1]^{-\frac{1}{2}}. \tag{A27}$$

Equation (A27) leads to the following table:

h/l	100	10	5	3	1.0	0.333	0.2	0.1	0.01
l		0.0314	0.168	0.270	0.378	0.740	1.36	1.78	2.55	8.15
h		3.14	1.68	1.35	1.13	0.740	0.454	0.357	0.255	0.0815

Sketching several of these cases, we obtain the variations of the reentrant cone shown in Fig. A12. Note how large the cone angles are. For $l > h$ the cone angle is $>90°$. Even the extreme case of $h/l = 100$ has a cone angle of 2 arc cot[3.14] $\approx 35°$. This is in marked contrast to most analyses of conical cavities where small cone angles are suggested for best design. We doubt that these designs are more practical than a sphere, although there

may be situations where this is the case. Note that these designs all have
more uniform directional emissivity than that of Fig. A10, and Fig. A10
is similar to illustrations by Hudson (p. 73) and Holter et al. (p. 44).
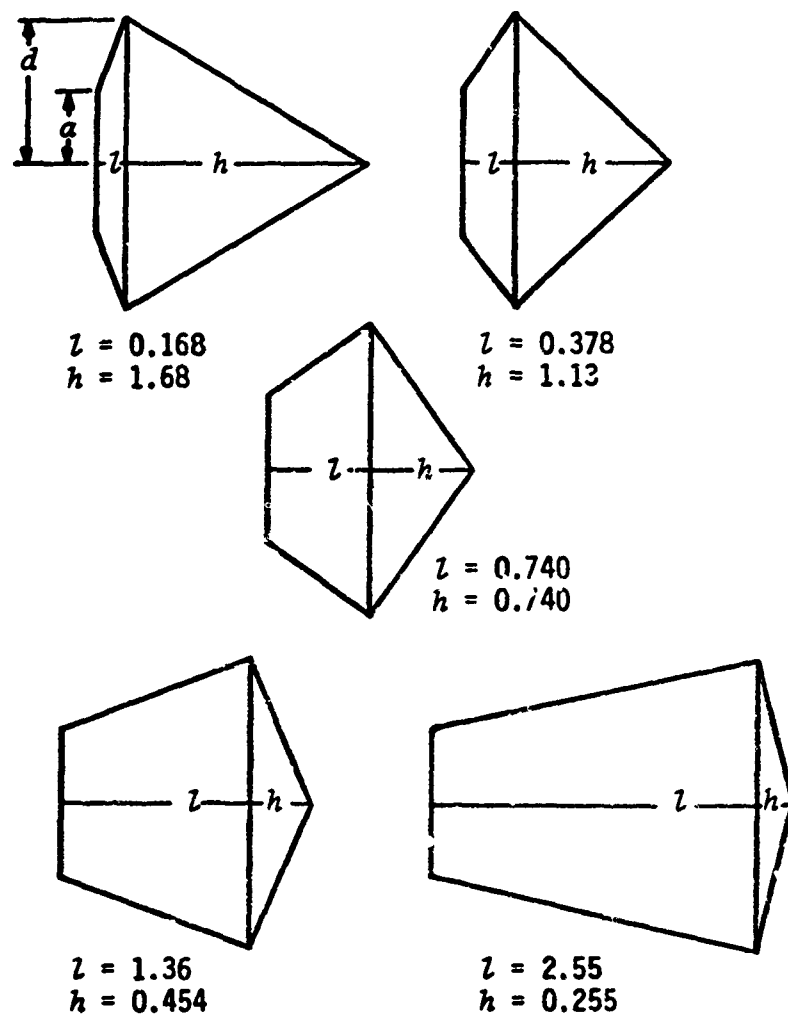

$l = 0.168$
$h = 1.68$

$l = 0.378$
$h = 1.13$

$l = 0.740$
$h = 0.740$

$l = 1.36$
$h = 0.454$

$l = 2.55$
$h = 0.255$

Fig. A12   Reentrant cone variations, normalized
to $d = 1.0$ and $a = 0.5$.

APPENDIX B

EMISSIVITY OF ISOTHERMAL SPHERICAL CAVITY WITH GRAY LAMBERTIAN WALLS*

An exact expression for the emissivity of an ideally diffuse, gray, isothermal spherical cavity is derived directly, making no geometrical approximations, and is shown to agree with the results of DeVos, Gouffé, and Sparrow and Jonsson, as compared by Fecteau. It appears that, even under ideal conditions, the spherical configuration is the only one that will have uniform isotropic emissivity over a wide angle, approaching a full hemisphere, across the entire aperture.

In a recent paper,[1] Fecteau shows that, for the idealized case of a spherical cavity with perfectly uniform, gray, opaque, diffuse (Lambertian), isothermal internal wall surfaces. the emissivity is exactly given, with perfect agreement and no geometrical approximations, for any size of aperture, by the theories of De-Vos,[2] Gouffé,[3] and Sparrow and Jonsson.[4] It is interesting, as a further check, to derive ϵ_a, the emissivity of the aperture of such a spherical cavity radiator, directly. The present derivation parallels to some extent that of Gouffé,[3] but, instead of deriving the effective reflectance of the cavity for radiation incident through its aperture, and then transforming to emissivity by Kirchhoff's law, this law is invoked only for the relationship between reflectance and emissivity for individual opaque surface elements, as in the DeVos[2] approach.

For an isolated opaque, Lambertian, surface element dA, the emissivity ϵ, the directional reflectance* ρ_d, and the bidirectional reflectance-distribution function† ρ' are each constant and are interrelated as follows[5-7]:

$$\epsilon = 1 - \rho_d = 1 - \pi\rho' \quad \text{[dimensionless]}. \quad (1)$$

In order to evaluate the cavity emissivity ϵ_a, we first determine the radiance $N_a(T)$ of the radiating aperture

of the isothermal cavity at temperature $T°$K, attributable to thermal emission alone. Reflections due to incident radiation reaching the internal walls through the aperture from outside are neglected. Then the emissivity of the cavity is

$$\epsilon_a = N_a(T)/N_B(T) \quad \text{[dimensionless]}, \quad (2)$$

where $N_B(T)$ is the radiance of a blackbody at the same temperature, $T°$K (Planck's law). Since radiance in a lossless isotropic medium is invariant[8] along any ray, $N_a(T)$ is also the same as the radiance of the remote portion of the interior cavity wall $N_w(T)$ seen through the emitting aperture, e.g., that of the element dA in the direction of the ray shown in Fig. 1. Under the postulated Lambertian conditions, the radiance of any such element dA of the interior wall in any direction may be expressed as

$$N_w = N_a = N_e + N_{r1} + N_{r2} + \ldots \\
+ N_{rn} + . \quad \text{[W·cm}^{-2}\text{·sr}^{-1}\text{]}, \quad (3)$$

where $N_e = \epsilon N_B(T) = (1 - \pi\rho')N_B(T)$ is the self-emitted thermal radiance of dA (the radiance it would have if it were isolated and emitting at $T°$K), and N_{rn} ($n = 1, 2, 3, .$) is the reflected radiance contributed by such thermal emission from the cavity walls after $(n - 1)$ intermediate reflections have taken place at different points on the internal wall surface.

The reflected radiance upon first reflection is N_{r1}. with no intermediate reflections. Hence. the incident radiance producing it is N_e. and is incident on dA through the solid angle Ω_w subtended by the cavity walls at dA, so that the incident irradiance is given by

$$H_s = N_e\Omega'_w \quad \text{[W·cm}^{-2}\text{]}, \quad (4)$$

where Ω'_w is the projected solid angle subtended at dA by the cavity walls (see Appendix for discussion of the

The author is with Sylvania Electronic Systems, Western Division, Mountain View, California 94040

* This denotes both the directional-hemispherical reflectance $\rho(\theta,\psi; 2\pi)$ and the hemispherical-directional radiance factor $R(2\pi; \theta, \varphi)$ [(D. B. Judd, J. Opt. Soc. Amer. 57, 445 (1967)].

† In Ref. 5, I called this the *partial reflectance* or *reflectance distribution function* and then, in a note added in proof, indicated a later preference for *bidirectional reflectance* for ρ'. However, subsequent experience with confusion and misunderstanding has led me now to favor strongly *bidirectional reflectance-distribution function*.

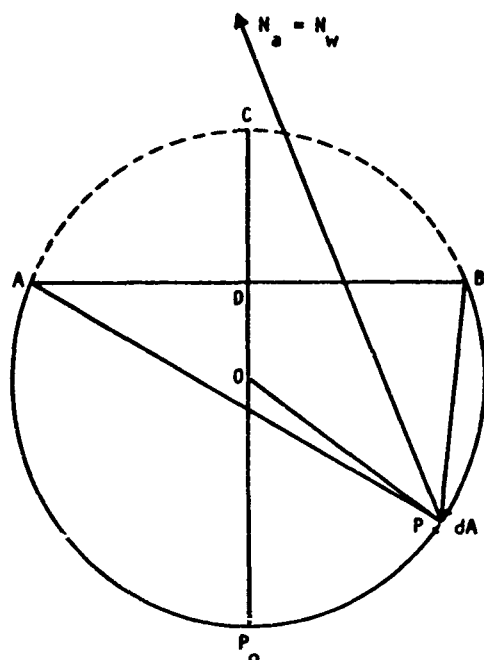*F. E. Nicodemus, Appl. Opt. 7(7):1359-1362, July 1968.

Fig. 1. Spherical cavity configuration. A plane section through the center O of a spherical cavity AP_oPB with an aperture ADB (perpendicular to this plane section); ACB is the spherical cap that would just cover the aperture to complete the sphere. A ray of radiance N_w is shown emitted by an element dA of the internal wall at P. If N_a denotes its radiance as it passes through the aperture and there is no attenuation in the empty cavity,
$$N_a = N_w.$$

concept of *projected solid angle*). From this, we can write

$$N_{r1} = \rho' H_i = \rho' N_e \Omega'_w \ [\mathrm{W \cdot cm^{-2} \cdot sr^{-1}}] \tag{5}$$

Note that, although ρ' and N_e are constants, Ω'_w may be different at different positions P of dA in the general case of an unspecified cavity configuration. A spherical cavity, however, has the convenient and probably unique property that Ω'_w is the same at every position of dA (see Appendix); so, for this case, N_{r1} is the same for all dA.

The reflected radiance upon second reflection is N_{r2}, with one intermediate reflection; so the incident radiance producing N_{r2} in this case is N_{r1}, and we have, similarly,

$$N_{r2} = \rho' N_{r1} \Omega'_w = N_e (\rho' \Omega'_w)^2 \ [\mathrm{W \cdot cm^{-2} \cdot sr^{-1}}]. \tag{6}$$

In general, then,

$$N_{rn} = \rho' N_{r(n-1)} \Omega'_w = N_e (\rho' \Omega'_w)^n \ [\mathrm{W \cdot cm^{-2} \cdot sr^{-1}}]. \tag{7}$$

Equation (3) now becomes

$$N_a = N_e[1 + (\rho' \Omega'_w) + (\rho' \Omega'_w)^2 + \ldots + (\rho' \Omega'_w)^n + \ldots]$$
$$\tag{8}$$
$$= N_e/(1 - \rho' \Omega'_w) =$$
$$\epsilon N_B(T)/[1 - (1 - \epsilon)\Omega'_w/\pi] \ [\mathrm{W \cdot cm^{-2} \cdot sr^{-1}}]$$

It is shown in the Appendix that the projected solid angle subtended at a point P of the surface of a sphere by any portion of the spherical surface, regardless of

shape or location, is directly proportional to its area. Accordingly, if s is the area of the spherical cap ACB (Fig. 1), which just covers the circular aperture ABD, and if S is the total surface area of the entire sphere including the cap, then[*]

$$\Omega'_c/\pi = s/S \ [\mathrm{dimensionless}], \tag{9}$$

since the complete spherical surface subtends a full hemisphere above dA with a projected solid angle of π sr, so that $\Omega'_w + \Omega'_c = \pi$.
Hence,

$$\Omega'_w/\pi = (\pi - \Omega'_c)/\pi = (1 - s/S) \ [\mathrm{dimensionless}]. \tag{10}$$

By combining Eqs. (2), (8), and (10), we can now write,

$$\epsilon_a = N_a/N_B = \epsilon \{1 - (1 - \epsilon)[1 - (s/S)]\}$$
$$= \epsilon/\{(s/S) + \epsilon[1 - (s/S)]\} \ [\mathrm{dimensionless}]. \tag{11}$$

This last expression is the same as Eq. (3) of Gouffé[2] for the isothermal spherical cavity. The equivalence to DeVos[2] and to Sparrow and Jonsson[4] has been demonstrated by Fecteau.[1]

It must be emphasized that this is an ideal case. A perfectly diffuse (Lambertian) surface has the same radiance in all directions, regardless of the way in which it is irradiated and/or heated. Since real surfaces, even rough natural ones, tend to become specular reflectors at grazing angles, it is possible that real cavities may depart substantially from the ideal situation treated here.

It should also be emphasized that Eq. (11) applies only to gray surfaces (or within spectral regions where the wall emissivity ϵ is a constant with respect to wavelength). In the general case, the relation holds only between the spectral quantities at any given wavelength:

$$\epsilon_a(\lambda) = \epsilon(\lambda)/\{(s/S) + \epsilon(\lambda)[1 - (s/S)]\} \ [\mathrm{dimensionless}] \tag{11a}$$

It is clear that, when the walls are not gray, the spectral cavity emissivity $\epsilon_a(\lambda)$ will also vary with wavelength. Then, in general, the total emissivity is

$$\epsilon_a(T) = [1/N_B(T)] \int_0^\infty \epsilon_a(\lambda) N_{\lambda,B}(\lambda,T) d\lambda$$
$$= [1/N_B(T)] \int_0^\infty \frac{\epsilon(\lambda) N_{\lambda,B}(\lambda,T) d\lambda}{(s/S) + \epsilon(\lambda)[1 - (s/S)]}$$
$$[\mathrm{dimensionless}]. \tag{11b}$$

This is *not* the same expression that results if one substitutes into the right side of Eq. (11), the following expression for ϵ, the total emissivity of the wall surfaces:

$$\epsilon(T) = [1/N_B(T)] \int_0^\infty \epsilon(\lambda) N_{\lambda,B}(\lambda,T) d\lambda \ [\mathrm{dimensionless}].$$

$[N_{\lambda,B}(\lambda,T)]$ is the spectral radiance of a blackbody at temperature T°K.]

---

[*] The subscripts a, c, and w are used throughout to refer, respectively, to the aperture (ADB), the spherical cap (ACB), and the internal spherical wall ($AP_oP'B$—See Fig. 1).

Incidentally, the note just after Eq. (5) suggests that the spherical cavity configuration is the only one that can achieve Lambertian radiation from its entire aperture (if the problem of heating the walls uniformly to achieve a truly isothermal condition can be solved). Even if the walls themselves are ideally Lambertian, as assumed in this analysis, and, further, if their reflectance is so low that all but the first two terms in Eq. (3) may be neglected, N_w will still vary with position, because of variations in N_A if there are variations in Ω'_w for the different elements dA that originate the rays passing through the aperture. It seems clear that departures from these ideal conditions can only add to the deviations from that uniform N_w (for all wall elements) that is necessary for uniform and isotropic N_a at the cavity aperture.

Appendix. Geometry of Radiometry—Projected Solid Angles

This appendix includes brief tutorial discussions of (a) some basic radiometric relations involving the concepts of radiance, projected solid angle, and throughput [Eqs. (A-1) to (A-8), inclusive] and (b) a theorem, used in the derivation in the body of this paper, concerning the projected solid angle subtended at a point on a spherical surface by any portion of that surface.

In general, the radiant power flowing in a beam of radiation passing through some convenient reference surface (emitting surface of source; stop, aperture, pupil, or window of optical system; receiving surface of detector; etc.) is given by[7]

$$P = \int_A \int_\Omega N(x,y,\theta,\varphi)\, \cos\theta\, d\Omega\, dA \quad [W], \qquad (A-1)$$

where x,y are position coordinates on the reference surface; $dA = dx\,dy$ is an element of the surface area (for simplicity, a plane surface is assumed); θ,φ are direction angles in spherical coordinates at dA (θ is the angle from the normal to dA, φ is the azimuth angle in the plane of dA); $d\Omega = \sin\theta\,d\theta\,d\varphi$ is an element of solid angle containing the ray of radiance $N(x,y,\theta,\varphi)$ which intersects dA at (x,y) in the direction (θ,φ); Ω is the complete solid angle containing all rays of the beam passing through dA; and A is the full area of the reference surface that is intersected by rays of the beam.

Equation (A-1) follows from the definition of radiance (N) as the radiant power (P) per unit solid angle (Ω) in the direction of a ray per unit projected area ($A\cos\theta$) perpendicular to the ray,[8]

$$N \equiv \partial^2 P / \cos\theta\, A\, \partial\Omega \quad [W\cdot cm^{-2}\cdot sr^{-1}], \qquad (A-2)$$

if we confine our attention to geometry (position and direction) and disregard any dependence on the other radiation parameters (wavelength or frequency ν, time or fluctuation frequency f, and polarization).

When the value of radiance N is the same everywhere (uniform for all x,y) and in all directions (isotropic for all θ,φ) throughout the beam, Eq. (A-1) simplifies to

$$P = N \int_A \int_\Omega \cos\theta\, d\Omega\, dA = N\Im \quad [W], \qquad (A-3)$$

where

$$\Im = \int_A \int_\Omega \cos\theta\, d\Omega\, dA \quad [cm^2\cdot sr] \qquad (A-4)$$

is the throughput, étendue, or area-solid-angle product of the beam.[8] In a lossless medium, where P remains constant all along the beam, it is easy to see that, since N is invariant along every ray, the throughput $\Im$ must also remain constant all along the beam. And since $\Im$ is determined entirely by the geometry, it follows that when losses (absorption and scattering) do occur, but do not modify the geometry of the main beam, the throughput $\Im$ will still be the same all along the beam. This holds true as long as there is no change in the index of refraction. Otherwise, in passing into another medium with a different index n, it is $N\,n^2$ that is invariant along a ray.[9] Hence, $n^2\Im$ will be invariant in the more general case.

Equation (A-4) can also be written:

$$\Im = \int_A \Omega'\, dA \quad [cm^2\cdot sr], \qquad (A-5)$$

where

$$\Omega' = \int_\Omega d\Omega' = \int_\Omega \cos\theta\, d\Omega = \iint_\Omega \cos\theta \sin\theta\, d\theta\, d\varphi \quad [sr] \qquad (A-6)$$

is the projected solid angle containing the rays that intersect dA. Furthermore, if there is no vignetting, so that Ω and Ω' do not change as the element dA passes to different points over the entire surface A, Eq. (A-5) can be further separated as

$$\Im = \Omega' \int_A dA = A\Omega' \quad [cm^2\cdot sr]. \qquad (A-7)$$

Obviously, computation can be greatly simplified by choosing, if possible, a reference surface on which there is no vignetting or the vignetting is negligible.

In the reverse situation, in which the total power P has been measured and the geometry of the beam is known so that the throughput $\Im$ can be evaluated, the radiance, from Eq. (A-3), is

$$N = P/\Im \quad [W\cdot cm^{-2}\cdot sr^{-1}]. \qquad (A-8)$$

Even when the beam is not uniform and isotropic, with constant N, Eq. (A-8) is often used to obtain an average or effective value of N, the equivalent uniform isotropic N.

An interesting property of a spherical surface, first presented by Sumpner,[9] is that the projected solid angle subtended at any surface element dA, by any portion of the same spherical surface, is determined completely by its area, irrespective of the configuration (its shape and its position, with respect to dA, on the
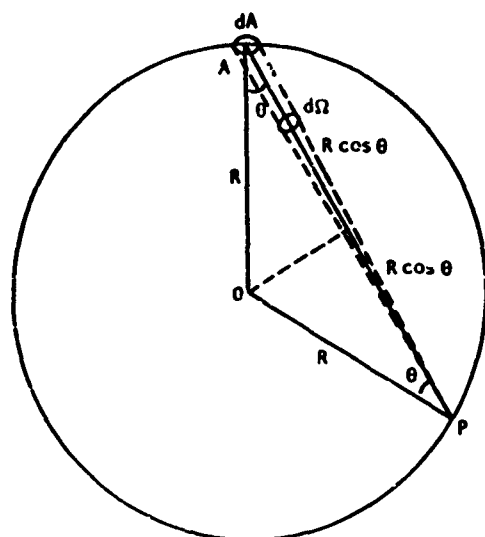
Fig. 2. Solid angle subtended by surface element dA of a spherical surface at P, a point on the same spherical surface.

spherical surface). It follows that the throughput between any two portions of the spherical surface is directly proportional to the product of their areas.

To prove these statements, consider any surface element dA at A on the surface of a sphere (Fig. 2). The element of solid angle $d\Omega$ subtended by dA at any other point P on the same spherical surface is

$$d\Omega = dA \cos\theta / (\overline{AP})^2 = dA \cos\theta / (2R \cos\theta)^2 \text{ [sr]}$$
$$= dA / (4R^2 \cos\theta) \text{ [sr]}, \quad (A-9)$$

where $\overline{AP}$ denotes the length of the line AP, and R is the radius of the sphere.

Hence, the projected solid angle subtended by dA at P is

$$d\Omega' = \cos\theta d\Omega = dA / 4R^2 \text{ [sr]}. \quad (A-10)$$

For a larger portion of the surface area, $A = \int dA$, the projected solid angle subtended at P is then

$$\Omega' = \int d\Omega' = \int (4R^2)^{-1} dA = A / 4R^2 \text{ [sr]}, \quad (A-11)$$

which, for any given sphere of radius R, is proportional only to the area A and is independent of its shape or configuration.

The surface area of a complete sphere is, of course, $4\pi R^2$, and, at any point P on that surface, it subtends a complete hemisphere. Accordingly, by substituting $4\pi R^2$ for A in Eq. (A-11), we obtain the projected solid angle for a hemisphere,

$$\Omega'_h = 4\pi R^2 / 4R^2 = \pi \text{ [sr]}. \quad (A-12)$$

This is easily verified by direct integration of Eq. (A-6) over a full hemisphere.

Accordingly, the ratio of the projected solid angle Ω'_a subtended at any point P on the sphere (Fig. 1) by a circular aperture ADB, or its equivalent spherical cap ACB, to the projected solid angle of a hemisphere, or π sr, is equal to s/S, where s is the area of the spherical cap and $S = 4\pi R^2$ is the surface area of the complete sphere, including the cap.

$$\Omega'_a / \pi = s/S \text{ [dimensionless]}. \quad (A-13)$$

Incidentally, this ratio Ω'/π is variously called the angle factor, configuration factor, form factor, or shape factor in the literature on radiant heat transfer. It is just the projected solid angle in hemispheres rather than steradians.

References

1. M. L. Fecteau, Appl Opt. 7, 1363 (1968).
2. J. C. DeVos, Physica 20, 669 (1954).
3. André Gouffé, Rev. Opt. 24, 1 (1945).
4. E. M. Sparrow and V. K. Jonsson, J Heat Transfer 84, 188 (1962); also NASA Tech. Note D-1289, National Aeronautics and Space Administration, Washington, D.C. (June 1962).
5. F. E. Nicodemus, Appl. Opt. 4, 767 (1965).
6. W. L. Wolfe and F. E. Nicodemus, in Handbook of Military Infrared Technology, W. L. Wolfe, Ed. (Office of Naval Research, Washington, D.C., 1965), Chap. 2.
7. F. E. Nicodemus, in Applied Optics and Optical Engineering, R. Kingslake, Ed. (Academic Press Inc., New York, 1967), Vol. 4, Chap. 8.
8. F. E. Nicodemus, Am. J Phys. 31, 368 (1963).
9. W. E. Sumpner, Proc. Phys. Soc. (London) 12, 10 (1892); also Phil. Mag. 35, 81 (1893).

APPENDIX C

MATERIALS

C1. Thermal Conductivity

The table of thermal conductivity of various materials that is reproduced on the following page was taken from Materials Engineering, 78(4):16, Mid-September 1973.

C2. Hardness

The following excerpt is from S. Wernick and R. Pinner, The Surface Treatment and Finishing of Aluminum and Its Alloys, ed. 3, Robert Draper, Ltd., Teddington, England, 1964, pp. 34 and 35.

While coatings formed by chemical treatment may be relatively soft and sometimes even powdery, films formed anodically are usually extremely hard and adhere tenaciously. Table 7 gives some comparative hardness values for various materials. On the other hand, the coatings are not as brittle as might be expected and do not usually crack[67] until the material has been stretched beyond its elastic limit, and brittleness may be further reduced by sealing the film in boiling water, or dichromate solution, etc.

Table 7. Hardness of materials (Bierbaum test)

Razor steel	1,550
Glass	2,000
Chromium	3,100
Aluminium	80
Aluminium anodic oxide film	
soft finish :	
face of film	180
centre of film	1,200
base of film	1,550
hard finish :	
face of film	140
centre of film	3,000
base of film	5,000

C3. Tensile Strength

The table of tensile strength of various materials that is reproduced on pages 148 through 149 was taken from Materials Engineering 78(4):6-7, Mid-September 1973.

Thermal Conductivity*

Btu hr sq ft °F/ft

Material ↓	High	Low	Material ↓	High	Low
Silver[b]	242	—	Austenitic Stainless Steels[b]	9.4	8
Copper	2~~	196	Columbium Carbide	8.2	—
Chromium Copper	187	—	Carbon[b]	5	3
Gold[b]	172	—	Calcia[d]	4[?]	—
Beryllia[d]	150	145	Zircon	3.6	2.9
Aluminum & Its Alloys	135	67.4	Cordierite & Forsterite	2.4	0.9
Plain Brasses	135	67	Polycrystalline Glass	2.1	1.1
Graphite[b]	120	70	Steatite	1.94	1.45
Phosphor Bronzes	120	29	Electrical Ceramics	1.6	0.9
Beryllium Copper	110	100	Magnesia[d]	1.5	—
Leaded Brasses	104	67	Wood Comp Board	1.5	0.08
Tungsten[b]	96.6	—	Wool Felts (1 in.), Sheet	0.91	0.30
Aluminum & Its Alloys (cast)	92.5	51.0	Silicon Nitride[d]	0.9	—
Beryllium[b]	87	—	Epoxies (cast)	0.8	0.1
Molybdenum & Its Alloys	84.5	67.1	Silica Glasses[b]	0.8	—
Magnesium Alloys	80	24	Silica, Vitreous[d]	0.8	—
Tin & Aluminum Brasses	67	58	Borosilicate Glasses[b]	0.7	—
Zinc & Its Alloys	65.3	60.5	Alkyds	0.60	0.20
Tungsten Carbide Cermet	50.1	25.7	Wood Comp Board, Softboard	0.6	0.3
Rhodium[b]	50	—	Lead Silicate & Soda-Lime Glasses[b]	0.5	—
Columbium & Its Alloys	42	31.5	Zirconia[d]	0.5	—
Platinum[b]	42	—	Polyvinyl Alcohol	0.46	—
Palladium[b]	41	—	Melamines	0.41	0.17
Alloy Steels[b]	38.5	21.7	Micas	0.4	0.2
Tin & Its Alloys	37	34	Phenolics (molded)	0.39	0.10
Nickel & Its Alloys[b]	36	8.7	Wool Felts (1 in.), Roll	0.39	0.24
Wrought Irons[b]	34.5	—	Plastics Laminates, High Pressure	0.29	0.17
Iridium[b]	34	—	Ureas	0.24	0.17
Aluminum Bronzes (cast)	33	22	Cellulose Acetate & Propionate	0.19	0.10
Tungsten-Titanium Carbide Cermet	32.9	16.5	Polyethylenes	0.19	—
Tantalum	31.5	—	Ethyl Cellulose	0.17	0.09
Silicon Bronzes	31	20	CFE Fluorocarbons	0.145	—
Gray Irons (cast)[b]	30	28	Nylons 6, 11, 66 & 610	0.14	0.10
Nitriding Steels[b]	30	—	Styrene-Butadiene & Nitrile Rubber	0.14	—
Malleable Irons	29.5	—	TFE Fluorocarbons	0.14	—
Alumina Cermets[e]	29	—	Acetal	0.13	—
Silicon Carbide[d]	29	9	Cellulose Nitrate	0.13	—
Tin Bronzes (cast), Leaded	28	—	ABS Resins	0.12	0.08
Carbon & Free-Cutting Steels[b]	27	—	Acrylics	0.12	0.10
Alloy Steels (cast)[b]	27	—	Nylon, Glass-Filled	0.12	—
Tin Bronzes (cast), High Leaded	27	—	Polyesters (cast)	0.12	0.10
Cupro-Nickels & Nickel Silvers	26	17	Silicone Rubber	0.12	0.11
Thorium	21.4	—	Polypropylene	0.11	0.10
Martensitic Stainless Steels[b]	21.2	11.7	Neoprene Rubber	0.11	—
Nodular or Ductile Irons[b]	20	18	Polycarbonate	0.11	0.05
Lead & Its Alloys[b]	19.6	16.0	Polyvinyl Chloride	0.10	0.07
Cobalt-Base Superalloys[e]	18.0	11.9	Silicones (molded)	0.097	0.089
High Temperature Steels[e]	17.3	15.8	Polyester, Thermoplastic. GP	0.095	—
Boron Nitride[e]	16.6	—	Phenylene Oxide SE-100	0.095	—
Ultra High Strength Steels[e]	16.6	—	Polyvinyl Formal	0.09	—
Boron Carbide[d]	16	—	Natural Rubber	0.08	—
Heat Resistant Alloys (cast)[b]	15.2	7.7	Polystyrenes, GP	0.08	0.06
Ferritic Stainless Steels[b]	15.1	12.2	Modified Polystyrenes	0.07	0.02
Cr-Ni-Fe Superalloys[e]	15	12.2	Butyl Rubber	0.05	—
Nickel-Base Superalloys[e]	15	9.5	Vinylidene Chloride	0.05	—
Stainless Steels (cast)[b]	14.5	8.2	Urethane Foamed-in-Place, Rigid	0.03	0.01
Uranium	14.5	—	Neoprene Foams	0.029	0.021
Tin-Lead-Antimony Alloys[b]	14	—	Prefoamed Cellulose Acetate, Rigid	0.027	0.025
Tantalum Carbide	12.8	—	Butadiene-Acrylonitrile Foams	0.025	0.021
Age Hardenable Stainless Steels[b]	12.1	8.87	Natural Rubber Foam	0.025	0.021
Zirconium Carbide	11.9	—	Silicone Foams, Rigid	0.025	—
Alumina Ceramics[b]	10.7	6.2	Phenolic Foamed-in-Place, Rigid	0.02	—
Low Expansion Nickel Alloys[b]	10.3	7.8	Polystyrene Foamed-in-Place, Rigid	0.02	—
Titanium Carbide	9.9	—	Prefoamed Epoxy, Polystyrene, Rigid	0.02	—
Titanium & Its Alloys[b]	9.8	4.3	Butadiene Styrene Foams	0.018	—
Zirconium & Its Alloys[b]	9.6	8.1	Thoria[d]	9	—

* Values represent high and low sides of a range of typical values at room temperature except where noted
[b] At temperatures between 20 and 212 F. • At room temperature (96+%. purity) [d] At temperatures above 1500 F
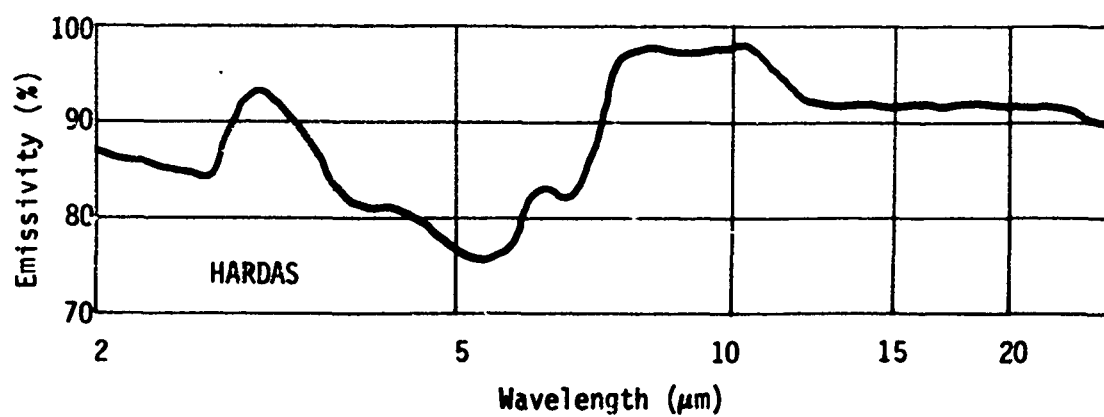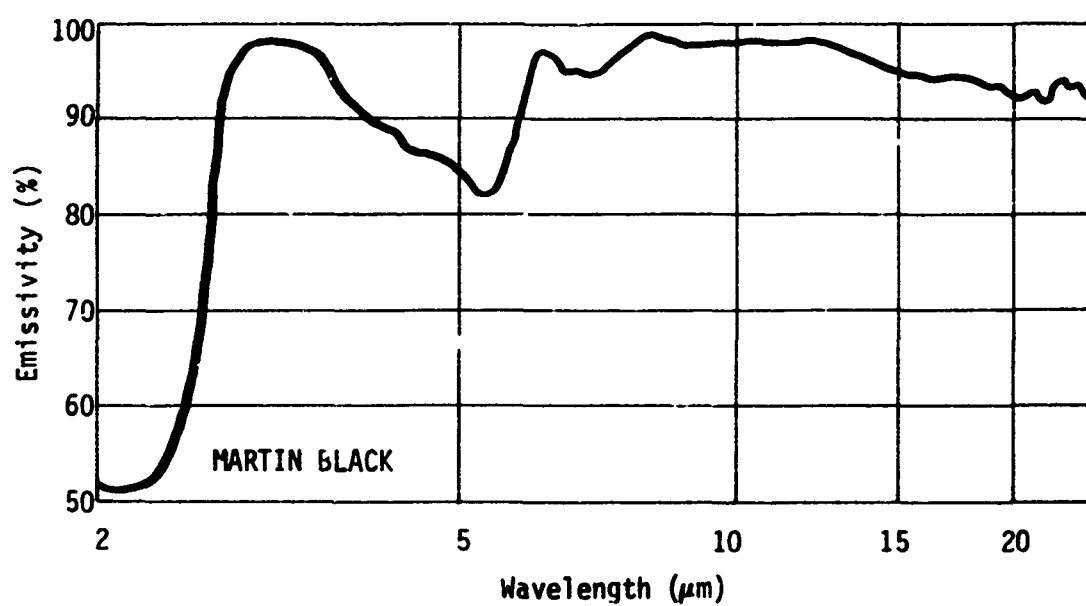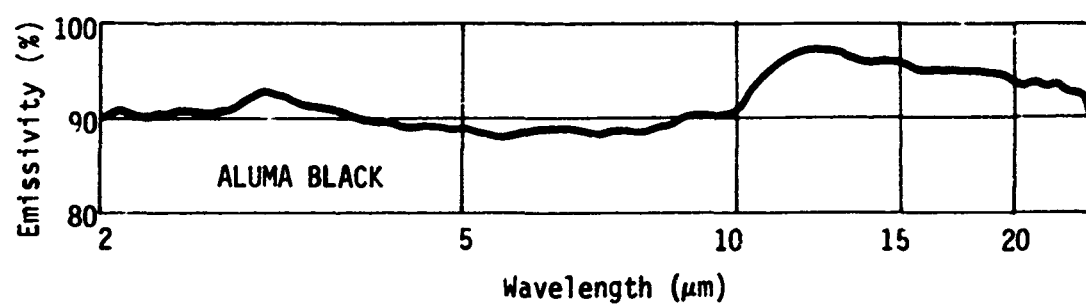CONVERSION FACTOR: To obtain cal/sec/sq cm/°C/cm, multiply by 0.004.

Tensile Strength*

1000 psi

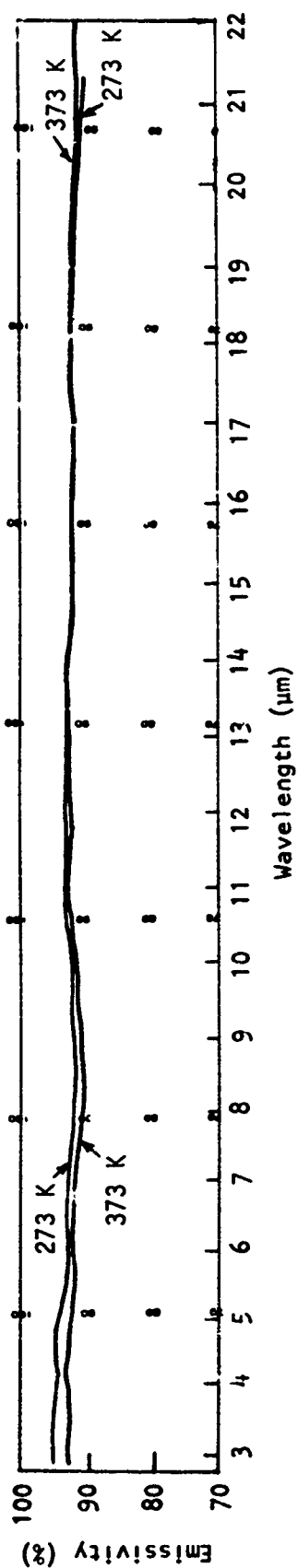| Material ↓	High	Low	Material ↓	High	Low
Asbestos, Chrysotile	570	200	Aluminum Bronzes (cast)	95	75
Alloy Steels, H & T.	345	98	Alloy Irons, Cast	90	13
Ultra High Strength Steels, H & T	319	275	Beryllium, Ann.	90	60
Asbestos, Crocidolite	300	100	Ferritic Stainless Steels, CW	90	75
Rhodium, CW	300	—	Polyethylene Fibers	90	11
Martensitic Stainless Steels, H & T	285	90	Silicon Bronzes, Ann.	90	40
Age Hardenable Stainless Steels, Sol'n Tr & Aged	240	86	Aluminum & Its Alloys, Sol'n Tr & Aged	88	35
Titanium & Its Alloys, Ht Tr	240	145	Ferritic Stainless Steels, Ann.	85	65
Carbon Steels, H & T.	237	75	Plastics Laminates, Low Pressure	85	8
High Temperature Steels, H & T.	235	139	Tin & Aluminum Brasses, Half Hard	84	75
Aluminum Silicate Fibers	230	50	Animal Fibers	83	20
Glass Fibers	220	200	Carbon Steels, V-Bearing	80	65
Stainless Steels (cast), H & T	220	110	Beryllium-Copper, Ann.	80	60
Tungsten, Str Rel	220	—	Cupro-Nickels, Hard & Light Drawn	80	60
Alloy Steels, Carb Grades	218	102	Leaded Brasses, Hard	80	55
Nitriding Steels, H & T.	206	121	Zirconium Copper, Hard	80	56
Nickel-Base Superalloys, Sol'n Tr & Aged	205	162	Hafnium, Ann.	77	—
			Low Expansion Nickel Alloys, Ann.	77	68
Alloy Steels (cast)	200	70	Cartridge Brass, 70%, Hard	76	—
Cr-Ni-Fe Superalloys, Sol'n Tr & Aged	196	114	Uranium, Depleted	75	—
Nickel & Its Alloys, Ann & Age Hard	190	130	Carbon Steels, Cb-Bearing	75	60
Austenitic Stainless Steels, CW	185	110	Low Alloy, High Str Steels	75	63
Beryllium-Copper, Hard	185	165	Gray Irons	75	15
Titanium & Its Alloys, Ann.	170	60	Low Brass, 80%, Hard	74	—
Cobalt-Base Superalloys, Sol'n Tr & Aged	165	101	Yellow Brass, Hard	74	—
			Ingot Iron, CD	73	—
Cellulosic Fibers	155	20	Rhodium, Ann.	73	—
Cr-Ni-Co-Fe Superalloys, Sol'n Tr & Aged	154	118	Vanadium, Ann.	72	—
Nodular Irons	150	60	Red Brass, 85%, Hard	70	—
Nickel & Its Alloys (cast), Ann. & Aged	145	30	Austenitic Nodular Irons	69	58
Tungsten-Titanium Carbide Cermet	145	118	Free-Cutting Brass, Half Hard	68	—
Low Expansion Nickel Alloys, CW	140	90	Zirconium & Its Alloys, Ann.	68	49
Titanium Carbide Cermet	134	26	Phosphor Bronzes, Ann.	66	40
Bast Fibers	132	57	Nickel Brasses & Bronzes (cast), Leaded.	65	30
Nickel-Base Superalloys	131	114	Tin & Aluminum Brasses, Ann.	65	53
Phosphor Bronzes, Hard	130	65	Vanadium, Ann.	64	—
Tungsten Carbide Cermet	130	—	Nickel Silvers, Ann.	63	49
Nylon Fiber	128	59	Chromium Copper, Hard	62	—
Polyester Fibers	126	67	Commercial Bronze, 90%, Hard.	61	—
Molybdenum & Its Alloys, Str Rel	125	95	Aluminum & Its Alloys, Hard	60	22
Hard Fibers	125	100	Architectural Bronze (extr).	60	—
Martensitic Stainless Steels, Ann.	125	65	Cupro-Nickels, Ann.	60	44
Columbium & Its Alloys, Str Rel	120	40	Leaded Brasses, Ann.	60	49
Nickel & Its Alloys, Ann.	120	50	Standard Malleable Irons	60	52
Pearlitic Malleable Irons	120	65	Tantalum, Str Rel	60	—
Yellow Brasses (cast), High Strength	120	60	Acrylic Fibers	57	26
Austenitic Stainless Steels, Ann.	115	80	Gilding, 95%, Hard	56	—
Heat Resistant Alloys (cast), Ht Tr	115	73	Copper, Hard	55	50
Vanadium & Hafnium, CW	113	112	Leaded Commercial Bronze, Half Hard	55	—
Carbon Steels, Carb Grades.	113	73	Micas, Natural & Synthetic	55	40
Free-Cutting Steels, CD	110	70	Magnesium Alloys	55	34
Heat Resistant Steels (cast)	110	65	Muntz Metal, Ann.	54	—
Cotton Fiber	109	44	Silver, CW	54	—
Vanadium, CW	109	—	Forging Brass (extr)	52	—
Zirconium & Its Alloys, CW	108	82	Sulfur Copper, Half Hard	50	—
Nickel Silvers, Hard	105	83	Aluminum & Its Alloys (cast) Sol'n Tr & Aged	49	36
Stainless Steels (cast)	105	69	Free-Cutting Brass, Ann.	49	—
Carbon Steels (cast)	100	60	Thorium, CW	49	—
Heat Resistant Nodular Irons	100	60	Tellurium Copper, Half Hard	48	—
Silicon Bronzes, Hard	100	70	Tin Bronzes (cast), Leaded	48	33

* Values represent high and low sides of a range of typical values at room temperature.

Material ↓	High	Low	Material ↓	High	Low
Wrought Irons, HR.	48	39	Tin & Its Alloys	2.7	2.8
Zinc & Its Alloys (cast)	47.6	25	ABS Resins	8.5	3
Fluorocarbon Fiber	47	—	Cellulose Acetate	8.5	1.9
Palladium. CW	47	—	Polyvinyl Butyral	8.5	4
Red Brasses (cast), Leaded	46	29	Polyvinyl Chloride Film, Rigid	8.5	6.5
Yellow Brass, Ann	46	—	Acrylics (cast), GP	8	6
Zinc & Its Alloys, CR	46	21	Cellulose Nitrate	8	7
Aluminum & Its Alloys, Ann	45	12	Polyethylene Film	8	1.6
Vinyl Fibers	45	12	Polystyrenes, GP	8	5
Yellow Brasses (cast), Leaded	45	30	Wood Comp Board (par. to sur), Hard-		
Cartridge Brass, 70%, Ann	44	—	board	7.8	2
Aluminum & Its Alloys (cast)	43	19	Cellulose Propionate	7.5	1.5
Ingot Iron, Ann	42	—	Lead & Its Alloys (cast)	7.4	2
Low Brass, 80%, Ann	42	—	Acrylics, High Impact	7.3	5.5
Zinc & Its Alloys, HR	42	19.5	Diallyl Phthalate	7	4
Magnesium Alloys (cast)	40	23	Electrical Ceramics	7	2.5
Vinylidene Chloride	40	4	Ethyl Cellulose	7	3
Alumina Ceramics	39	20	Mica, Glass-Bonded	7	5
Red Brass, 85%, Ann.	39	—	Cellulose Acetate Butyrate	6.8	1.9
Tin Bronze (cast), High Leaded	38	25	CFE Film	6.6	6.3
Chromium Carbide Cermet	37	36	Chlorinated Polyether	6	—
Commercial Bronze, 90%, Ann	37	—	Rubber Hydrochloride Film	6	5
Plastic Laminates, High Pressure	37	7	Urethane Rubber (gum)	>5	—
Copper, Ann	35	32	CFE Fluorocarbons	5.7	4.6
Cobalt (cast)	34.4	—	Polypropylene	5	—
Gilding, 95%, Ann	34	—	Polyvinyl Alcohol	5	1
Thorium, Ann	34	—	Polyvinyl Chloride Film, Nonrigid	5	1
Gold, CW	32	—	Silicones (molded)	5	4
Nylon, Glass-Filled	31	19	Wood Comp Board (par. to sur),		
Platinum, CW	30	28	Particle	5	0.5
Palladium, Ann	28	20	Lead & Its Alloys (rolled)	4.7	2.4
Polyester Film	28	17	Natural Rubber (black)	4.5	3.5
Silicon Carbide	25	3	Nitrile Rubber (black)	4.5	3
Boron Carbide	22.5	—	Polythylene, High Density	4.4	2.9
Silver, Ann	22	—	Pollyallomer	4.2	3.5
Platinum, Ann	21	18	Alkyds GP & Elec	4	3
Alumina Cermets	21	—	Neoprene Rubber (black)	4	3
Cellophane	19	7	PVC-Nitrile Rubber Blend Film	4	1.5
Gold, Ann	19	—	Styrene-Butadiene Rubber (black)	3.5	2.5
Polyester, Thermoplastic, reinf	17.3	8	TFE Fluorocarbons	3.5	2.5
Nylon 6 Film	17	13.8	Lead & Its Alloys (extr)	3.3	2
Polystyrenes, Glass-Filled	17	11	Butyl Rubber (black)	3	2.5
Epoxies (molded)	16	5	Cordierite	3	—
Polyvinylidene Chloride Film	15	7	TFE Film	3	2
Steatite	15	4.8	Polyethylene, Medium Density	2.4	2
Nylon 66 & 610	12.6	7.1	Viton Rubber (gum)	>2	—
Epoxies (cast)	12	0.1	Graphite	2	0.4
Nylon 6 & 11	12	8.5	Wood Comp Board (par. to sur), Soft-		
Polystyrene Film	12	7	board	2	0.2
Zircon	12	4.5	Fluorinated Acrylic Rubber (gum)	1.2	—
Tin-Lead-Antimony Alloys (cast)	11.8	6.8	Urethane Foamed-in-Place, Rigid	1.2	0.020
Modified Polystyrenes	11	3	Carbon	1.1	0.3
Polyvinyl Formal	11	9	Polysulfide Rubber (gum)	>1	—
Acrylics (molded, extr)	10.5	5.5	Silicone Rubber (gum)	1	0.6
Acetal	10	—	Polyethylene, Low Density	0.9	2.5
Alkyds, Impact	10	6	Wool Felts, Sheet	0.8	0.4
Ethyl Cellulose Film	10	6	Polyethylene Foam, Flexible	0.67	—
Forsterite	10	—	Prefoamed Epoxy, Rigid	0.65	0.05
Melamines, Phenolics (molded)	10	3.5	Wool Felts, Roll	0.6	0.08
Polyesters (cast)	10	0.9	Vinyl Foams, Flexible	0.2	0.01
Polypropylene Film	10	5	Prefoamed Polystyrene, Rigid	0.19	0.030
Polyvinyl Alcohol Film	10	6	Prefoamed Cellulose Acetate, Rigid	0.18	0.11
Ureas	10	5	Polystyrene Foamed-in-Place, Rigid	0.13	0.030
Polycarbonate	9.5	9	Neoprene Foams	0.1	0.02
Hard Rubber	9.3	2	Butadiene-Styrene Foams	0.03	—
Methylstyrenes	9.3	6.6	Phenolic Foamed-in-Place, Rigid	0.075	0.004
Phenoxy	9.5	9.0	Butadiene-Acrylonitrile Foams	0.04	—
Phenolics (cast)	9	2.5	Natural Rubber Foam	0.020	0.010
Polyvinyl Chloride	9	1			

* Values represent high end low sides of a range of typical values at room temperature.

C4. Spectral Emissivity Measurements

Measurements by TRW

Emissivity (%) vs Wavelength (μm) — ALUMA BLACK

Emissivity (%) vs Wavelength (μm) — MARTIN BLACK

Emissivity (%) vs Wavelength (μm) — HARDAS

Measurements by Naval Electronics Laboratory Center

ALUMA BLACK

HARDAS, dc current

151
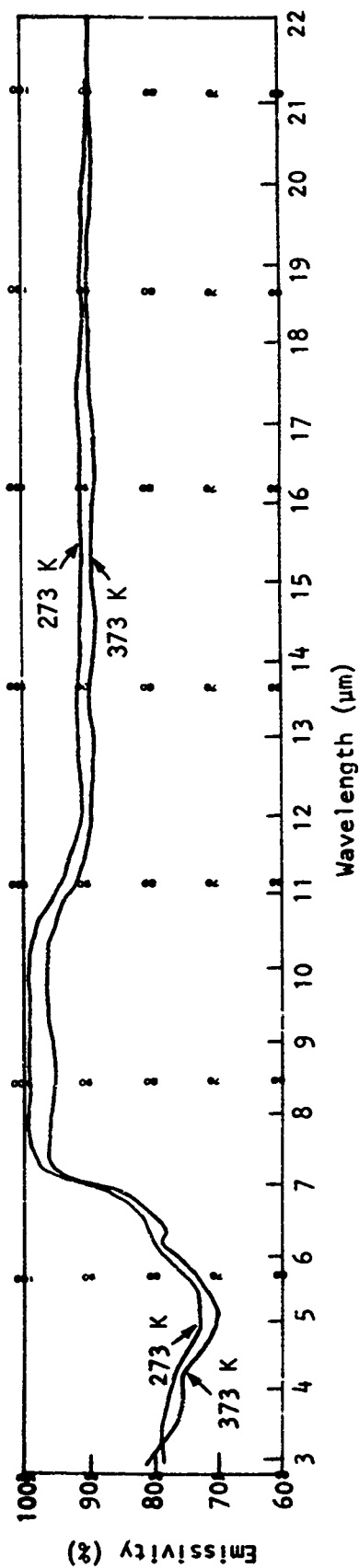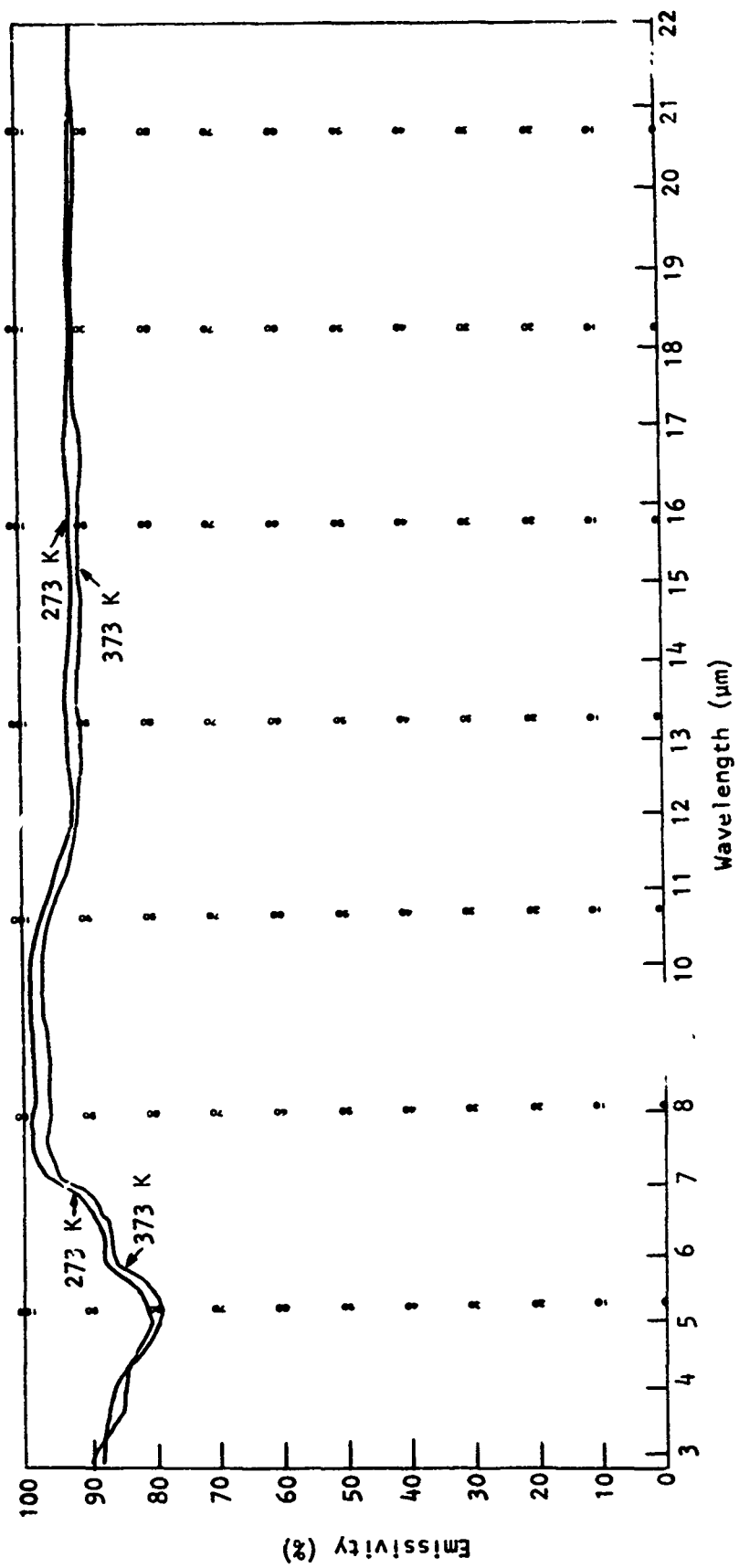
HARDAS, ac-dc current
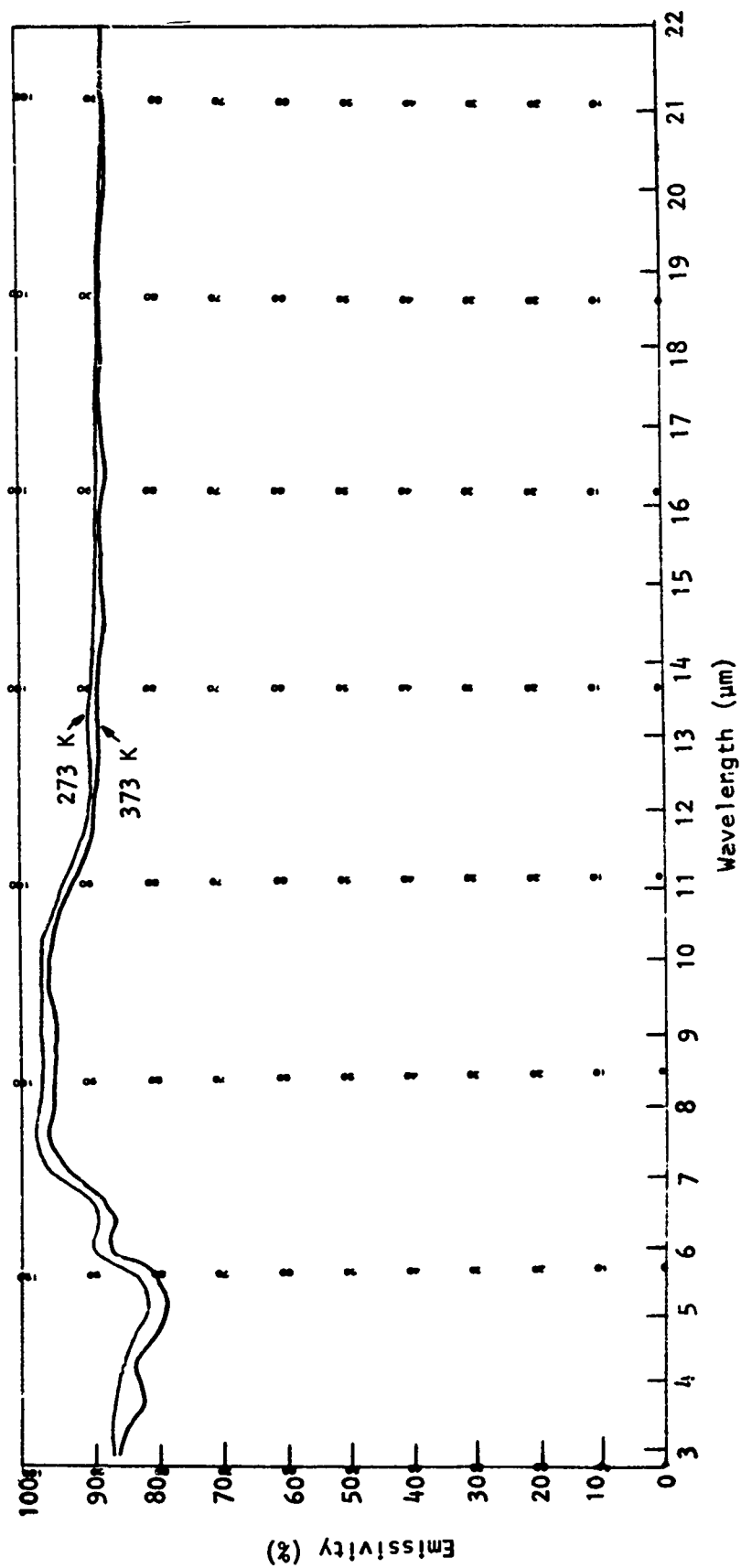
HARDAS (run at same time as delivered unit)
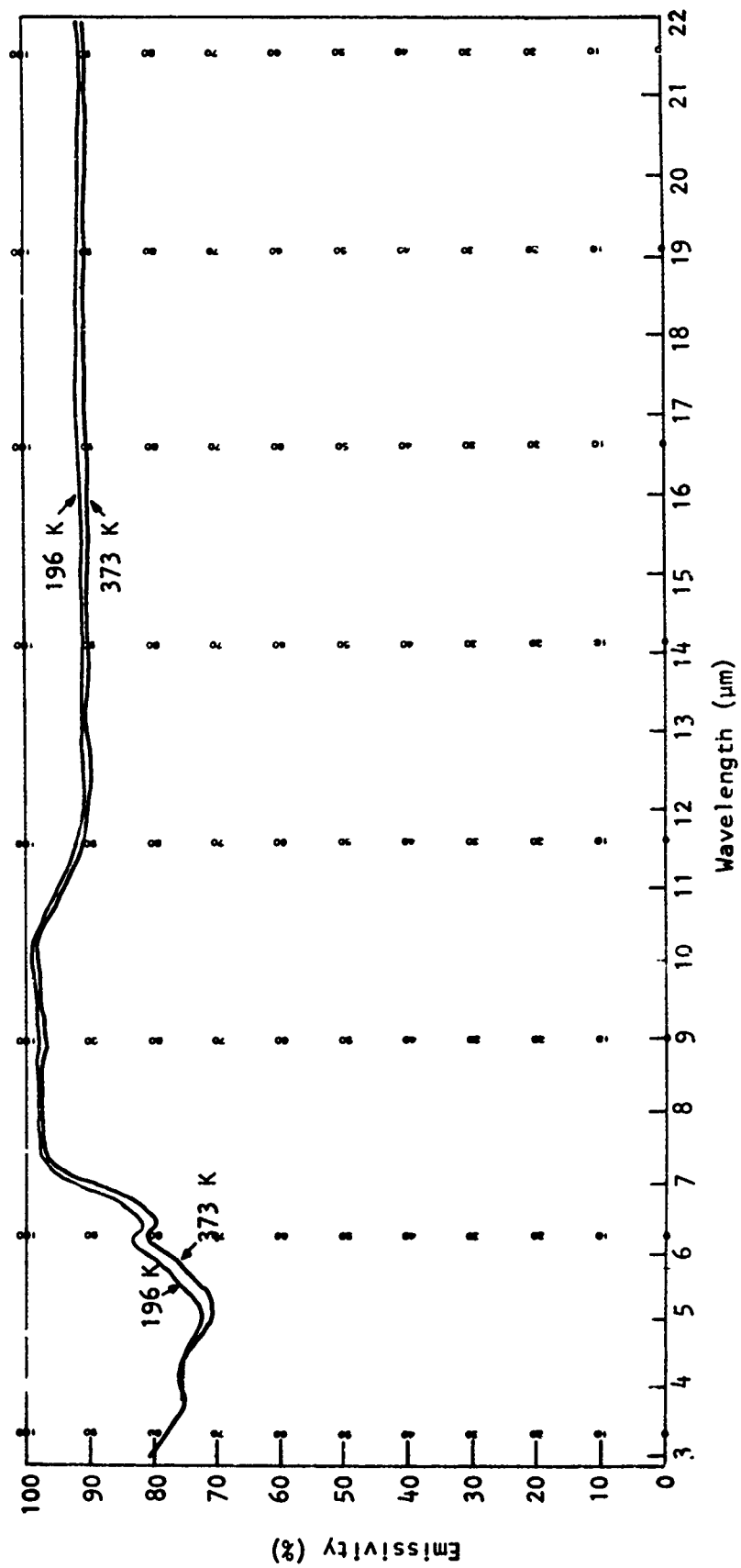
HARDAS (heated 60 h in air at 600 K)

154

C5. Effective Cavity Emissivity

$$\varepsilon' = \frac{\varepsilon[1 + (1-\varepsilon)(s/S - s/S_0)]}{\varepsilon(1 - s/S) + s/S}$$

$$\varepsilon = \pi r^2 = \pi(0.1)^2 = \pi/100$$

$$S = 4\pi R^2 = 4\pi(0.625)^2 = 1.5625\pi$$

$$s/S = 1/156.25 = 0.0064$$

$$S_0 = S$$

$$\varepsilon' = \frac{\varepsilon}{0.9936\varepsilon + 0.0064} = \frac{1}{0.9936 + 0.0064/\varepsilon}$$

The first equation is from Gouffé (André Gouffe, 1945, Rev. d'Optique 24:1-10). Fecteau (M. L. Fecteau, 1968, Appl. Opt. 7(7):1363-1364) showed that, for a diffuse, isothermal, spherical cavity, Gouffé, De Vos, and Sparrow and Johnson give the same closed-form expression for cavity emissivity. The last equation is used to calculate Table III on page 36 of this report.

APPENDIX D

PROBLEMS WITH LOW SIGNALS

D1. Measurement Difficulties

The difficulties in making accurate measurements of low-level infrared signals have been described by two authorities as follows:

(1) The following is by Fred E. Nicodemus in Applied Optics and Optical Engineering, ed. by Rudolf Kingslake, Vol. IV, Academic Press, New York, 1967, pp. 263-264:

The term "radiometry" is applied in this chapter to the measurement of the energy or power of electromagnetic radiation. The treatment will be limited primarily to incoherent optical radiation (infrared, visible, and ultraviolet), which obeys the laws of geometrical optics.

Radiometry enjoys the dubious distinction of relatively poor attainable precision and accuracy, especially when contrasted with the measurement of frequency or time,[1] where one part in 10^{10} or even 10^{11} is achieved. In radiometry, accuracies of a few percent or more are often acceptable as being results of careful work, and extreme precautions are required to achieve a fraction of one percent, or even one percent.

Many factors contribute to this state of affairs including, ultimately, the following basic assumptions of geometrical optics: time intervals (even differential elements) are large with respect to a single period of the radiation frequency and, correspondingly, distances are large with respect to a wavelength.[2] Radiant power is distributed, and may vary simultaneously, with wavelength, with position, with direction, with time, and with polarization. Furthermore, every particle of matter in a measurement situation is emitting and/or absorbing and/or scattering radiation. Included are the gas molecules in the direct radiation path and every portion of the measuring instrument itself. These effects, too, may vary greatly with wavelength, position, direction, time, and polarization.

[1] A. G. McNish, *Electro-Technol.* (*New York*) 71, 113-128 (1963) (No. 53 in Electro-Technology Science and Engineering Series).

[2] M. Planck, "Theory of Heat" (transl. by H. L. Brose) (Vol. V of "Introduction to Theoretical Physics"). Macmillan New York, 1957.
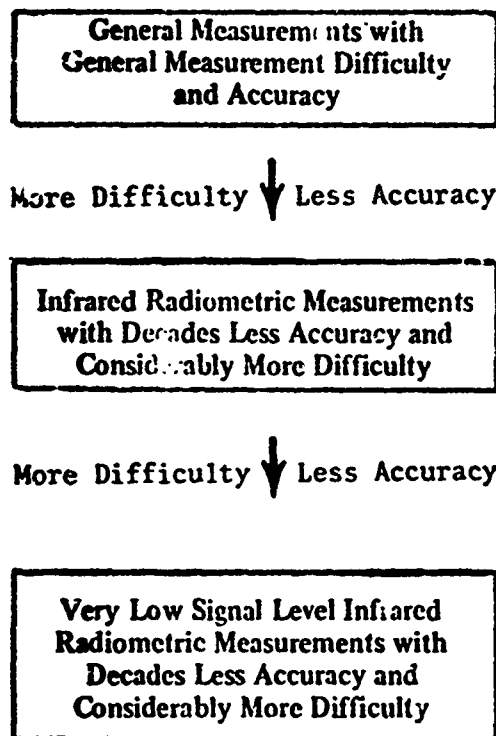
(2) The following is from an editorial on "Opportunities in Astrophysics," by Nobel laureate Charles H. Townes, in Physics Today, March 1973, p. 116:

One can foresee many interesting problems for optical physicists in the area of astrophysics that engages our group at Berkeley—the development and exploitation for astrophysics of techniques for electromagnetic waves ranging from a few centimeters to a few microns. Recently at a symposium of the Optical Society of America on the future of science and technology I had the opportunity to point out that this broad region of the spectrum represents one of the more neglected areas of physics, and one that has been particularly underdeveloped for astrophysical uses. One should not underestimate the importance of x-ray astronomy, ultraviolet astronomy, or even further developments in the more extensively exploited visible region. But between 1-cm and 1-micron wavelengths there are four decades of the spectrum that are promising for astronomy and where fascinating discoveries have recently been made, but which are as yet remarkably undeveloped.

Consider sensitivity, for example. In the optical and in the microwave region, techniques are available that can detect a signal borne on only a few photons. In much of the infrared region, 10^4 to 10^5 photons are presently needed, so that one can hope to gain several orders of magnitude in sensitivity. Why does the infrared region appear so poor in sensitivity? In part, it is because infrared heat radiation is so pervasive that it interferes with infrared signal detection. On the other hand, with modern cryogenics, as well as the possibility of working in space beyond the atmosphere, there is no reason why instruments cannot be in a very cool environment and thus realize several orders of magnitude gain in sensitivity even in the regions of most abundant heat radiation.

A general rule of thumb for calibration holds that calibration errors should be limited to about 0.1 measurement errors.

The previous discussion can be summarized in the following art of measurement accuracy and difficulty:

```
┌────────────────────────────────┐
│   General Measurements with     │
│  General Measurement Difficulty │
│          and Accuracy           │
└────────────────────────────────┘
```

More Difficulty ▼ Less Accuracy

```
┌────────────────────────────────┐
│ Infrared Radiometric Measurements│
│   with Decades Less Accuracy and │
│    Considerably More Difficulty  │
└────────────────────────────────┘
```

More Difficulty ▼ Less Accuracy

```
┌────────────────────────────────┐
│  Very Low Signal Level Infrared  │
│   Radiometric Measurements with  │
│     Decades Less Accuracy and    │
│   Considerably More Difficulty   │
└────────────────────────────────┘
```

Note: Calibration measurements associated with
      the bottom box should have ten times the
      accuracy of the measurements themselves,
      so they are even more difficult to make.

D2. Ultralow Radiometric Signals

Definition: Ultralow radiometric signals are defined as propagations of electromagnetic radiation that are so low that they can be satisfactorily measured only by the use of a collecting optical system that forms a concentrated image on a detector.

Because radiometric signals are propagations of electromagnetic energy, they can be thought of in terms of electric field vectors $\vec{E}$, magnetic field vectors $\vec{H}$, and Poynting vectors $\vec{S} = \vec{E} \times \vec{H}$. Measurement of these signal levels might consist of evaluation of the $\vec{E}$ and $\vec{H}$ vectors or the $\vec{S}$ vectors as functions of time and position in space. This representation of radiometric signal propagation and measurement is valid as long as the signals are strong enough that a small detector can be placed in the path (or field or beam) and readings of satisfactory accuracy can be observed. However, if the signal levels are decreased, the readout becomes less well defined, and if the signal levels are reduced more and more, then for any given detector there is a level below which measurement cannot be made with the detector operating alone. However, in the upper levels of this region of signal strength, reasonably accurate measurements can be made by introducing a collecting optical system that concentrates the energy falling on a large area so that it falls onto a small area detector.

The concepts associated with ultralow radiometric signals are best considered in terms of wave optics. Imperfections in the optical quality of ultralow radiometric signals are then imperfections in wavefronts. Wavefront imperfections can be described in terms of the aberration function or wave aberration function (see R. S. Longhurst, Geometrical and Physical Optics, Longman, London, ed. 2, 1967, pp. 343-346).

In general, ultralow radiometric signals have imperfections in their wave configurations, so imperfect images are formed on the detector, and these imperfect images give rise to measurement errors. "Satisfactorily measured," as used in the definition of ultralow radiometric signals, means that signal-to-noise problems when the detector is used alone are greater than measurement problems due to the imperfect image when a collecting optics system is used.

The above discussion provides an introduction to the properties of ultralow radiometric signals.

Properties:

(1) The simplest, or ideal, case of ultralow radiometric signal is a section of a spherical wave from a point source at a very great distance with no disturbing medium or other influence between the source and the point of detection. If the section of the sphere is small compared to the distance from the point source, then the wave is approximately a plane wave.

(2) Real--in contrast to ideal--radiometric signals have imperfections from true spherical wave or plane wave configurations, and these wave imperfections cause image imperfections when the ultralow signals are collected to form a concentrated image on a detector.

(3) The upper limit of these signals is dependent on the detector involved. For a very sensitive detector, the upper limit is at a lower level than for a less sensitive detector.

(4) The readout from ultralow radiometric signals depends on several quantities in an approximately proportional way: signal level, area of the entrance pupil of the collecting optical system, responsivity of the detector.

(5) The readout signals depend on the spatial properties of the image and the detector in a more complicated way. Most detectors have contours of varying sensitivity, and all concentrated energy images have contours of higher and lower intensity, so readout signals for ultralow radiometric signals depend in general on how the contours of intensity in the image fall on the contours of sensitivity in the detector.

(6) Readout signals depend on the quality of the collecting system optics. This is an obvious corollary of property (5), where the contours of intensity of the image were described.

(7) Readout signals depend on the quality of the optics of the optical simulator for the case where ultralow radiometric signals have been formed by an optical simulator consisting of a radiation source and an optical system. This property is similar to the last two mentioned above.

Ultralow radiometric signals are customarily treated like ordinary radiometric signals, and this is not correct. Consider for example the paper by Ralph Stair, William B. Fussell, and William E. Schneider, "A Standard for Extremely Low Values of Spectral Irradiance," Appl. Opt. 4(1):85-89, Jan. 1965.

That paper gives a description of the production and evaluation of extremely low irradiance values but fails to consider how poor optical quality can lead to erroneous readings if collecting optics are employed. This is an especially serious deficiency because very low signals are involved and because the optical system employed has very severe astigmatism. If the radiation fields delivered by the equipment described in that paper are used to irradiate bare detectors, then the work of that paper is correct. But if the fields are used with collecting optics, then the severe astigmatism must be taken into account. In general, ultralow radiometric signals with less optical imperfection are more useful than ones with greater optical imperfection: More accurate and more repeatable measurements can be made for signals with better optical quality. If Stair, Fussell, and Schneider had considered this point, they might have redesigned their optical system to have nearly normal incidence of their radiation on their spherical mirrors instead of the approximately 45° angles of incidence actually employed.

In summary, ultralow radiometric signals are signals too low to be satisfactorily measured by a detector alone, and they must be detected by a collecting optic system that forms a concentrated image on a detector. The optical quality of these ultralow radiometric signals influences any readout measurements made on them, so it is not sufficient to specify such signals in terms of watts per square centimeter or in terms of the electric field vector, magnetic field vector, or Poynting vector but it is necessary to include an expression of optical quality.

D3. Normalization*

It may be helpful to look at an example for which numbers are given. A somewhat extreme though not unrealistic situation is examined to gain a better impression of the order of magnitude of the discrepancies that may be encountered. In Fig. 2, the upper curve is the spectral radiance $L_\lambda(\lambda)$ [W·cm^{-2}·sr^{-1}·μm^{-1}] of a black thermal radiator at about 100°C (boiling water); the middle curve is an arbitrarily selected spectral radiance responsivity $R_L(\lambda)$ [V·W^{-1}·cm^2·sr] for a radiometer placed close to the black vessel of boiling water, so the throughput of the radiometer is completely filled by radiation from that source only; and the bottom curve, as before, is the resulting spectral output $V_\lambda(\lambda) = L_\lambda(\lambda) \cdot R_L(\lambda)$ [V·μm^{-1}], the observed output V [V] being the area under that spectral curve. This illustrates a poorer match between the spectral intervals of the incident radiation and of the instrument responsivity than that in Fig. 1. The resulting effects of uncertainties in the limits λ_1 and λ_2 are, thus, greater than before.

Furthermore, because of the very poor match of spectral intervals, the peak-normalized radiance,

$$L_{np} = V / R_L(\lambda_m)[\text{W} \cdot \text{cm}^{-2} \cdot \text{sr}^{-1}], \qquad (18)$$

is a very poor approximation to the actual total radiance

$$L = \int_0^\infty L_\lambda(\lambda) \cdot d\lambda \, [\text{W} \cdot \text{cm}^{-2} \cdot \text{sr}^{-1}], \qquad (19)$$

or even to the total radiance in the interval $\Delta\lambda = \lambda_2 - \lambda_1$,

$$L_{\Delta\lambda} = \int_{\lambda_1}^{\lambda_2} L_\lambda(\lambda) \cdot d\lambda \, [\text{W} \cdot \text{cm}^{-2} \cdot \text{sr}^{-1}]. \qquad (19a)$$

The peak of the (Planck law) curve of $L_\Lambda(\lambda)$ actually occurs at about 7.7 [μm] (not shown in Fig. 2), and only about 2% of the total radiation (all wavelengths) lies in the spectral region below 4.25 [μm] (shown in Fig. 2 as λ_2), the upper limit for $R_L(\lambda)$. By graphical integration of the area under the spectral output curve $V_\lambda(\lambda)$, the output is found to be approximately $V = 0.95$ [V]. The peak spectral radiance responsivity at $\lambda_m = 3.5$ [μm] is $R_L(\lambda_m) = 3000$ [V·W^{-1}·cm^2·sr]. Hence, the peak-normalized radiance is

$$L_{np} = V/R_L(\lambda) = 0.95/3000$$

$$= 3.2 \times 10^{-4} \, [\text{V} \cdot \text{cm}^{-2} \cdot \text{sr}^{-1}]; \qquad (20)$$

i.e., a source of radiance 3.2×10^{-4}

[W·cm^{-2}·sr^{-1}], concentrated in a narrow wavelength band about 3.5 [μm], would produce the same output of 0.95 [V], so it is called the peak-normalized equivalent at that wavelength with respect to the given spectral responsivity $R_L(\lambda)$. On the other hand, the total incident radiance (Stefan-Boltzmann law) is given by Eq. (19), or by

$$L = \sigma \cdot T^4/\pi = 5.67 \times (373.2)^4/3.1416$$

$$= 3.5 \times 10^{-2} \, [\text{W} \cdot \text{cm}^{-2} \cdot \text{sr}^{-1}]$$

$$= 109 \cdot L_{np} \qquad (21)$$

which is certainly not a very close approximation.

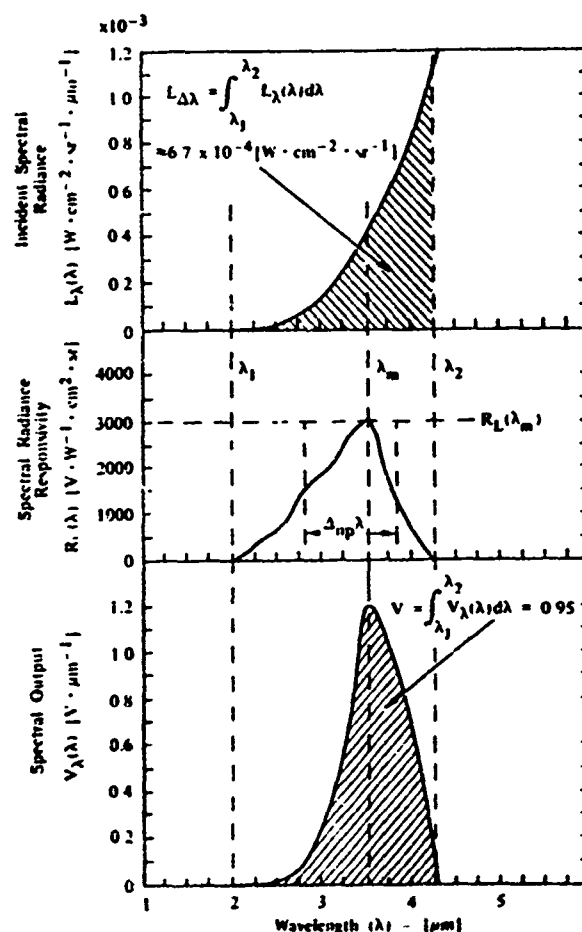

Fig. 2. Selective (peak response at 3.5 μm), radiance radiometer response to 100°C black surface. (Adapted from Fig. 3-2, p. 3-12, Ref 18).

*From F. E. Nicodemus, "Normalization in Radiometry," Appl. Opt. 12(12): 2960-2973, Dec. 1973; part of p. 2964 is reproduced here.

APPENDIX E

TILTED-COMPONENT TELESCOPE REFERENCE MATERIAL

E1. Ray Fan Diagrams

There are a number of useful graphical presentations that are helpful in the evaluation of lens designs. Examples are spot diagrams, MTF curves, and transverse ray intercept plots or ray fan diagrams. The most valuable for designing and appraising the progress of a lens is the ray fan diagram. This method has several advantages: We can see where the rays are coming from; pupil aberrations are noted by slope errors; and the shape and slope of the plot tell the nature of the aberration as well as its magnitude. The effect of vignetting is easily understood in terms of these plots.

The drawing below shows what a transverse ray intercept aberration plot is. We would actually be interested in rays passing through every point of the entrance pupil, but, generally, sufficient information is gained by tracing fans of rays in two mutually perpendicular planes. The one shown is the "meridional" (or tangential) plane, and the one perpendicular to it is known as the "sagittal" plane. Generally, rays in the sagittal plane are well behaved. The rays in the tangential plane need show no symmetry and can be very complex in an aspheric lens. We can assume that the rays in some intermediate plane will be no worse than those in the two planes traced. (Occasionally, this is a poor assumption.)
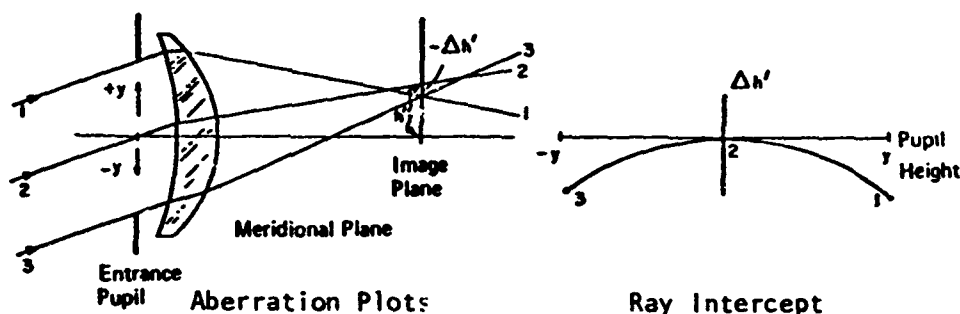
Aberration Plots   Ray Intercept

163

Note: The optical design just shown actually has mirror, not lens, el-
ements, but a lens is shown because it is easier to understand.

The ray passing through the center of the pupil, if it reaches the ex-
treme field of view, is known as the "principal" (or chief) ray. Any other
central ray can be considered a fractional principal ray. Its intercept height
is on the image plane, which we take as the paraxial focal plane. The inter-
cepts of the other rays, with respect to this intercept, are then plotted
versus the height of the ray on the entrance pupil. The abscissae are pupil
heights, y, and the ordinates are $\Delta h'$ or h'. We can also plot the slopes of
the emerging rays versus $\Delta h'$, which, strictly speaking, is the best way. If
we plot pupil height versus $\Delta h'$, the pupil information is concealed.

Similarly, sagittal fans can be traced and their intercepts plotted.
With the slope plotted against the intercept, these are termed (z' - tanv')
curves. It is only necessary to trace half a fan because it shows an inverted
mirror symmetry.

E2. Design Examples of Tilted-Component Telescopes (TCT's)*

A telescope with reflecting rather than refracting surfaces has considerable appeal since
it is perfectly achromatic. In any sufficiently complex reflector, of course, the limiting
defect is the problem of one mirror obscuring another. The only way to avoid this ob-
scuration is to have the center of view run obliquely through the collection of mirrors.
The same applies to catadioptrics. The purpose of this report is to describe one class of

---

*Sections E2 and E3 are reprinted from R. A. Buchroeder, "Design Examples
of Tilted-Component Telescopes (TCT's) (a Class of Unobscured Reflectors)," Op-
tical Sciences Center Tech. Rept. 68, 1971, an abstract of which is as follows:

A tilted component telescope (TCT) is one that features no obstructions in the light
path yet is appreciably simpler to build than conventional off-axis instruments. The
principles of TCT design are applicable to scanning and image-stabilized optics and
should allow improvements in that field.

The author has collected and computer-evaluated designs representative of existing
art: Schiefspiegler, Yolo, catadioptric Herschelian, and Schupmann. It is expected that
these evaluations will enable optical scientists to appraise the merits of the TCT ap-
proach and will stimulate the development of second-generation designs.

unobscured reflectors—the "TCT's" (tilted-component telescopes)- and to describe and evaluate some examples of TCT designs.

For purposes of discussion, most existing unobscured reflectors may be classed into one of three types (Figs. 1a-c).

First is the *eccentric pupil* class, an ordinary coaxial design used with an eccentric stop. Its center of view coincides with the parent axis. Common examples are the "off-axis" paraboloid and "off-axis" Schmidt.

Fig. 1a

ECCENTRIC
PUPIL
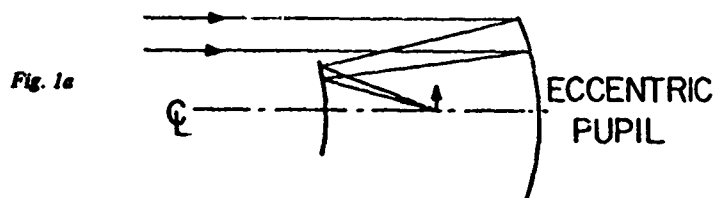
In the *off-axis* class, the center of view coincides not with the parent axis but with a principal (chief) ray of a nominally coaxial design. The Herschelian telescope is of this form. We have excluded the "off-axis" paraboloid from this class. Although the distinction is perhaps only semantic, a designer approaches the problem differently than he approaches the problem of an eccentric.

Fig. 1b

OFF-AXIS
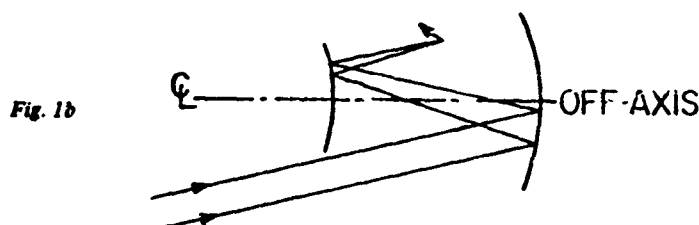
Third is the *tilted-component* class, the subject of this report. In the TCT, each component is treated as being rotationally symmetric in its own coordinate system, and it is centered on its vertex, which will define the optical axis of the telescope. Each component may be assigned, in its own coordinate system, a marginal and a principal ray, with the principal ray passing through the vertex. The components are then assembled so that their principal rays define the optical axis of the completed telescope. The axial aberration is described by the summation of the axial and field aberration of each component. Since each component is centered on its vertex, the system may be assembled by conventional methods such as boresighting and autocollimation.

Fig. 1c

TCT
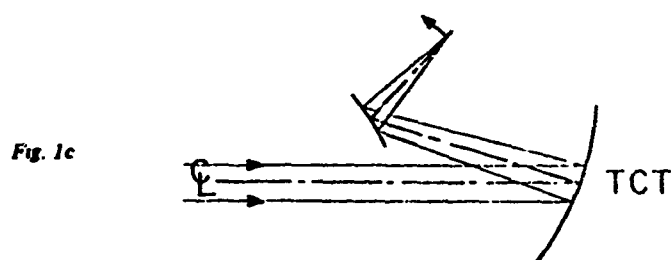
For a single element this is identical to the off-axis class. Some designers suspect that it is possible to relate all TCT's to a sufficiently complex off-axis design. We have not yet resolved the question. However, if any of our three-mirror TCT's are reduced to an equivalent coaxial off-axis design, the asphericities are extraordinarily large. Indeed, none are of common form in regard to pupil position and principal ray path. None are similar to the usual coaxial three-mirror reflectors; our formulas show that these cannot give a corrected "axis" on the assumption that the local vertex is spherical or even coaxially aspheric. On the other hand, our formulas show that the TCT configuration gives perfect third order correction.[1]

1. R. A. Buchroeder, "Some possibilities in large unobscured optics," Optical Sciences Center Newsletter 3(1):14-16, Jan-Mar 1969.

E3. Fundamentals of the TCT

The idea behind the TCT is simplicity itself. Each component is assumed to be centered on the effective optical axis, and each element is assumed to be spherical. Fig. 2 gives the geometry. In the designing process, the "axial" ray is the principal ray for each element in terms of its local coordinate system, and the Seidel aberration for each component is easily computed. The idea is to have the field aberrations of each component offset those of the other components, giving a corrected axis to the telescope. It is usually convenient to do this iteratively on a calculator rather than to attempt to solve the pertinent formulas,[2] which are helpful but awkward. One quickly gets a feel for successful configurations, and it can be shown without much difficulty that only certain ones are successful. Similarly, it can be shown that others are unsuccessful and are to be avoided.

$$K = \frac{i_{pr}}{i}$$

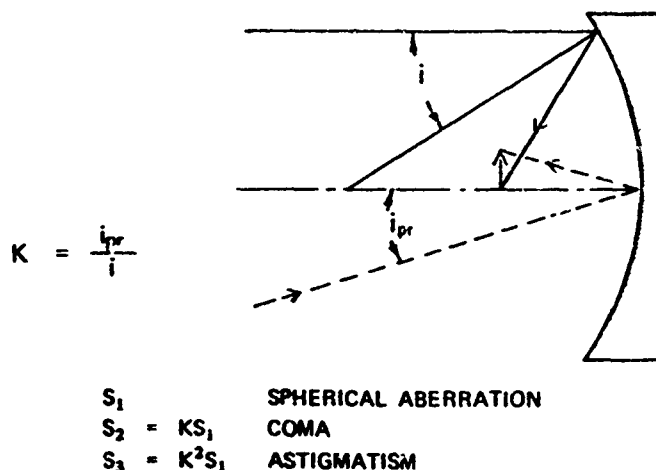|	
S_1	SPHERICAL ABERRATION
$S_2 = KS_1$	COMA
$S_3 = K^2 S_1$	ASTIGMATISM

Fig. 2. Local coordinate system.

2. R. A. Buchroeder, "Tilted-component telescopes. Part I. Theory," Applied Optics 9(9) 2169-2171, Sept. 1970.

Design Classes

For purposes of discussion the writer has divided into four broad groups the TCT designs that are to be described here.

Schiefspiegler. The Schiefspiegler is any TCT that has a convergent mirror objective followed by a *convex* secondary mirror. Like most of the examples of this type, the name Schiefspiegler was created by a German, Anton Kutter. It has no exact translation but means approximately "leaning mirror telescope."

Yolo. The Yolo is any TCT with a convergent mirror objective followed by a *concave* secondary mirror. It has the general form of two mirrors, one of which is usually toroidal, but at least two all-spherical forms are possible as well. Its theoretical advantage over the Schiefspiegler is that its mirrors are cooperative in power, allowing lower sensitivity to misalignment, or, if this is sacrificed, greater relative aperture for a given sensitivity. Compared with the Schiefspiegler, it seems capable of reduced image tilt. The name Yolo is that of a county in California dear to its inventor, Arthur S. Leonard, retired professor of mechanical engineering (University of California), who is responsible for all the Yolo designs described in this report.

CHT. A CHT (catadioptric Herschelian telescope) is any TCT that has a convergent mirror objective followed by one or more tilted, nonwedged spherical lenses. Prof. Leonard has proposed the use of full-aperture lenses to seal off the tube, but we do not deal with this in the present report. A catadioptric Herschelian is not a new idea, but in the past this type has utilized wedged or noncentered elements.

Schupmann. In 1899, the German mathematician Ludwig Schupmann was granted U.S. Patent 620,978 for a unique family of catadioptric telescopes. In a preferred embodiment, the Schupmann applies the tilted-component concept to eliminate obstruction, but the concept is equally applicable to coaxial designs of higher speed.

The Schupmann consists of a convergent *refractive* objective (usually a singlet), a field element near its focus, and a reimaging catadioptric relay known as a Mangin mirror (which in its simplest form is a singlet). The field element images the objective onto the relay, while the overcorrect color of the Mangin corrects the undercorrect color of the simple objective. A proper disposition of the three groups, with all elements made from the same glass, allows complete elimination of secondary spectrum. The relay usually has a coma-free form, as does the objective. Either may or may not be aspheric, according to the design. In the coma-free case, the Mangin may be tilted to eliminate the conflict of the image with the light, and its resulting astigmatism may be corrected by tipping the objective. More sophisticated forms employing peculiar aspherics have been reported by Baker,[3] but experience in the fabrication of these has been discouraging. The writer recommends the tilted-component approach despite the fact that these have a slight amount of chromatic astigmatism.

The Schupmann is similar to its predecessor, the Hamiltonian telescope, in using a simple objective corrected with a Mangin mirror. It differs, however, in that a field lens is used, whereas the Hamiltonian Mangin reimages a virtual rather than a real image. Consequently, the Hamiltonian has lateral color and cannot be perfectly corrected for secondary spectrum.

3. J G. Baker, Astron. J. 59(2):74-83, Mar. 1954.

The Schupmann design evaluated in this report was described in a bulletin of the Schupmann Club, a group that is doing a great deal to dispel the pessimism previously associated with the difficulty of making a Schupmann telescope. Actually, although considerable skill and patience are required to extract the full capability of this form of telescope, a satisfactory (though perhaps not perfect) Schupmann telescope need be no harder to build than an ordinary refracting doublet.

General Behavior

In a high-acuity telescope it is important that the axial image be free of spherical aberration, coma, and astigmatism. Ideally, distortion and image tilt also would be zero, but designs that offer this advantage are usually too difficult to interest the average customer, who is an amateur astronomer. Consequently, many of the designs disregard these latter two defects since they do not harm contrast or resolution.

Astigmatism, Coma, Distortion. Figure 3 compares the astigmatism in a TCT with that of two ordinary coaxial designs. Note that the astigmatism in a TCT resembles the anastigmatic node of a complex lens, which is obtained by balancing higher order aberration against the Seidel terms. In the TCT this crossing is obtained entirely by third order calculation. It is found that in the simple three-mirror Schiefspiegler this astigmatism is linear with field (in the meridional plane) rather than increasing with the square of the image height, as is usual in a normal lens. This simple variation of astigmatism suggests that it can be cured by appropriate aspheric figuring. What is needed is a parabolically varying deformation on one of the components—in this case the tertiary mirror for best results. One side should be turned up, the other turned down. This is well approximated by an off-axis section of an aspheric mirror, which itself could be further approximated by a toroid. The implications are controversial and will not be dwelt upon here.
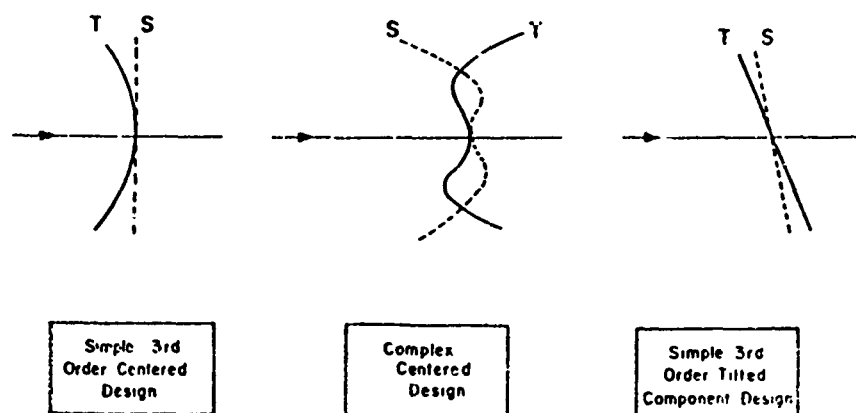

Fig. 3. Comparison of astigmatism.

Three axially symmetric elements allow the simultaneous elimination of astigmatism, coma, and distortion. The successful configurations are the three-mirror Schiefspiegler and three-mirror Yolo. These always require that the third mirror reflect the light back toward the incoming axis. Tilting of the third mirror in the opposite direction gives an unsuccessful configuration.

With only two axially symmetric elements, astigmatism and coma cannot be simultaneously eliminated. However, it is possible to use one less mirror if one of the two mirrors is toroidal. Some of the best designs described here use toroidal mirrors. Because a toroid is hard to obtain by usual optical fabrication techniques, A. S. Leonard has spent a number of years developing a simple means of mechanically warping and holding a nominally spherical mirror. He has built a number of such devices, and they seem to work satisfactorily. Figure 4 shows how a successful version works. Prof. Leonard has a more complex version in use for a 12½-in. telescope of the same form.

Clearly, one could temporarily distort the mirror, figure it as a sphere, then release the distortion when finished and use the mirror in the ordinary fashion. The point is, toroidal mirrors *have* been made and *are* successful, so there is no great objection to using them, at least in professional instruments.
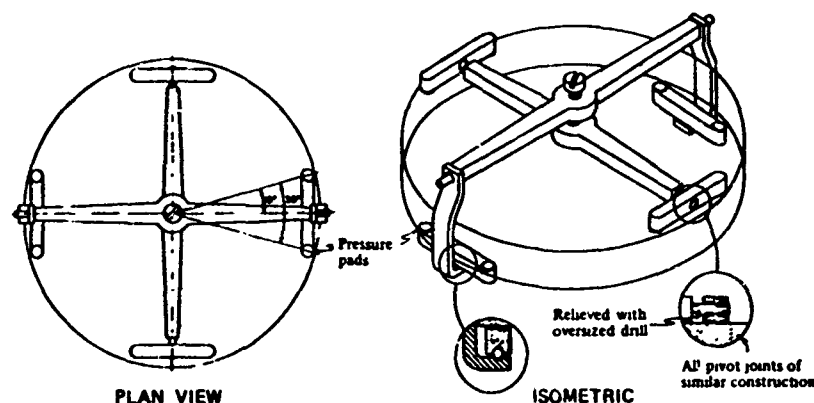
Fig. 4. Warping harness for 8-in. Yolo.

Image Tilt and Anamorphic Distortion. Figure 5 shows how image tilt, which is a fairly natural occurrence in any "off-axis" telescope, can be corrected by an additional element, either a lens or a mirror. Our experience suggests that if only axially symmetric components are used, four elements will be required for a perfectly corrected axis in a TCT. However, we have not proved that three elements cannot do the same job. Using toroids, it is possible to achieve a fully correct axis with three elements; with only two elements, one achieves a sufficient approximation to perfection.

When we change our reference system on an off-axis telescope and use some field point as the "axis," distortion must be reevaluated. It is proper to speak of tangential and sagittal distortion, the two being mutually perpendicular. Points above and below the center (as well as left to right in a three-dimensional TCT) are not symmetric about

Positive Relay

Negative Relay
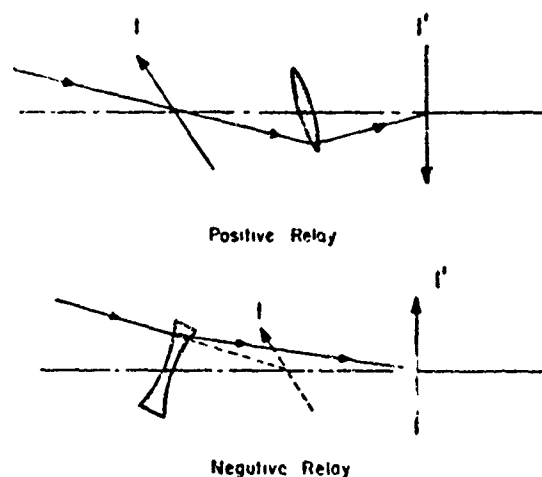
Fig. 5. Two simple methods of image rectification.

the center of the field. If the field of view is small compared with that chosen as the axis for the off-axis system, the rate of change over the new field of view is small and the distortion changes only slowly.

To a first approximation, a circular object will be reimaged as an ellipse with its axes proportional to the tangential and sagittal focal lengths at the center of the image. This behavior is characteristic in the TCT.

Rather than deal with paraxial quantities, we can use the centroid data for the spot diagrams at the smallest field angle, ±3.75 arc min. Here the centroids are not greatly disturbed by aberration, which can confuse one's definition of distortion.

It is difficult to define the image tilt since the image may be some complicated toroidal sheet. Since these designs are slow and have small fields of view, however, we will assume the image is flat and compute a value for it from the centroid data. The following somewhat arbitrary definitions will be used to specify anamorphic distortion (due to the difference in tangential (t) and sagittal (s) focal length) and image tilt.

Given: x, y, and z coordinates of the spot centroids for the upper, r, left, and right image points for a field diameter of 7.5 arc min. The reference axis of the design has been adjusted so that it nearly (or exactly) follows the path of the central ray of light.

Distortion $$D = \frac{[y(\text{upper}) - y(\text{lower})] - [x(\text{left}) - x(\text{right})]}{x(\text{left}) - x(\text{right})}$$

Tilt (t) $$T(t) = \frac{z(\text{upper}) - z(\text{lower})}{y(\text{upper}) - y(\text{lower})}$$

Tilt (s) $$T(s) = \frac{z(\text{left}) - z(\text{right})}{x(\text{left}) - x(\text{right})}$$

Symmetry simplifies these for the two-dimensional designs The observer's perspective is that of looking in with an eyepiece, and x is positive to the left. The incoming rays approach from the left and focus to the right. In situations where this doesn't occur naturally, it is accomplished with a dummy plane reflector at the front. Consequently, all the designs give inverted and reverted images except for the Schupmann, where a dummy reflector after the Mangin gives an erect image.

Up and down, right and left, are with regard to the untilted system (i.e., when the tilts are set to zero). When these are set to their proper values, the *apparent* observing angles for the designs may have different signs. A positive tangential image tilt means that the top of the field of view (not necessarily the apparent top), as seen by the observer with his eyepiece, will protrude toward his eye. Similarly, in the skewed designs, a positive sagittal tilt means that the left side protrudes.

The distortion is with respect to a plane normal to the TCT's axis. Distortion on the inclined focal surface would be calculated by considering the cosine elongation. A negative distortion is partially corrected by a tilt of either sign, while positive distortion is always aggravated by an inclined image plane. Data for the normal (perpendicular) distortion and image inclination are presented below.

ANAMORPHIC DISTORTION AND FIELD TILT

Design	D, %	Tilt (t), degrees	Tilt (s), degrees
Schiefspieg .			
25-cm f/20, Kutter lens	- .072	+ 7.712	--
4¼-in. f/26.6, anastigmatic	+ .310	+ 4.373	--
12½-in. f/20.2, 3-mirror O'Neill	- .889	+ 9.019	--
10-in. f/19.2, 3-mirror equiradius aspheric	-5.609	+16.658	--
Yolo			
12-in. f/15, 2-mirror anamorphic	+ .213	- 1.129	--
10-in. f/15.2, 3-mirror (2D)	+3 34!	- 7.000	--
10-in. f/13.3, 3-mirror (3D)	+ .253	- 833	- 442
10-in. f/13.9. 3-toroid	900	+ 1.043	--
CHT			
10-in. f/10.2	+ .381	+ 7.013	--
4¼-in. f/10 7	+ .251	+ 5.528	--
4¼-in. f/10 5, single lens	+ .349	+ 4 084	--
48-in. f/6.4, monochromat	--	--	--
10-in. f/15.1, hybrid (Schief/CHT)	+ .944	+16.501	--
Schupmann			
4-in. f/12	.000	- 2.757	-2.015

In general, image tilt is more objectionable than distortion since the eye loses its range of accommodation as it grows older. With the equiradius Schiefspiegler, it is essential to tilt the eyepiece for even a young eye, whereas with the other Schiefspieglers experiments show the tilt to be acceptable. The reaction to the inclined field of the CHT's has been mixed, so apparently it depends on the observer.

NBS TRACEABILITY DOCUMENTS

F1. Distance Calibration

Certificate of Calibration
DIAL INDICATOR LABORATORIES

7044 Lankershim Boulevard   North Hollywood, Calif. 91605

983-1414 — Phone — 877-4636

TEST #_____D2474_____

FOR _____OPTICAL SCIENCES CENTER_____ DATE ___12-18-73___

This Is To Certify That The Following Instruments Have Been Calibrated In Compliance With All Applicable Portions Of Federal Specifications, GGG-C-00105a, Mil. Std. 120, Mil-C-45662, H28, Mil-I-18422D, Mil-G-18997B, Mil-H-4034B, Mil-Q-9858A

Using Standards Traceable to National Bureau of Standards, Wash., D.C., Cert. No. 232 09/208031

INSTRUMENT	SER. NO.	SIZE	CALIBRATION DATA
SPECIAL PLATE WITH 2 SCRIBE LINES .025" APART 30 INDIVIDUAL CHECKS WERE .KEN USING AS FAR AS POSSIBLE THE CENTER OF THE SCRIBED LINES DETERMINATED AVERAGES SHOW THE DISTANCE OF THE LINES TO BE .02445 ± .00001			INSTRUMENTS USED MITUTOYO PH 350 OPTICAL COMPARATOR UNITRON TM TOOLMAKERS MICROSCOPE 400X WITH BENEFIT OF A NIKON .001 MM GRADUATED CALIBRATION PLATE.

Calibration Condition: Air Temperature, 20°C.   Certified

DIAL INDICATOR LABORATORIES

F2. Temperature Calibration

Certificate of Calibration and Testing

Part Name **Platinum Resistance Temperature Sensor**   Rosemount Model No. __146NV.1COF-4X__

Customer Part No. _____—_____   Customer P.O. # __1-41678__

Serial No. __6973,6974,6975__

All applicable tests required by __RMT spec. 146MA__ Revision __—__ were successfully conducted utilizing equipment whose calibration is directly traceable to the National Bureau of Standards. All materials used in the manufacture of this unit are in strict accordance with the applicable specification requirements. Applicable test data is on file subject to examination Specific calibration and test data are attached or recorded on the reverse side of this form.

__4 June 1973__
Date of Certification

R. M. Peterson
Quality Control Representative

Rosemount Inc.

Form no. 4833A

Certificate of Calibration and Testing

Part Name **Plat. Resis. Temp. Sensor** Rosemount Model No. **146MA100F-4X**

Customer Part No _____ Customer P.O # **1-16670**

Serial No. **7760, 7761** _____

_____

_____

_____

All applicable tests required by **MMT spec. 146MA** Revision **A** were successfully conducted utilizing equipment whose calibration is directly traceable to the National Bureau of Standards. All materials used in the manufacture of this unit are in strict accordance with the applicable specification requirements. Applicable test data is on file subject to examination. Specific calibration and test data are attached or recorded on the reverse side of this form.

17 January 1974
Date of Certification

O. M. Peterson
Quality Control Representative

Rosemount Inc.

Form No. 4002a

ROSEMOUNT ENGINEERING COMPANY TEST REPORT
QUALITY CONTROL APPROVED   IPTS 1948

MODEL 146MA100F4X
SERIAL 6973
DATE 12 26 72

ACTUAL CALIBRATION POINTS	
TEMP C	RESISTANCE OHMS
0.0000	99.97400
-195.8284	16.94370

FSC IS   3.90826380
DRM IS   0.00000000

TEMP C	RESISTANCE OHMS
-200.00	17.15025
-190.00	21.46523
-180.00	25.80498
-170.00	30.11815
-160.00	34.10022
-150.00	38.65315
-140.00	42.87882
-130.00	47.07898
-120.00	51.25530
-110.00	55.40933
-100.00	59.54253
-90.00	63.65624
-80.00	67.75172
-70.00	71.83009
-60.00	75.89240
-50.00	79.93958
-40.00	83.97247
-30.00	87.99178
-20.00	91.99815
-10.00	95.99208
0.00	99.97400

ROSEMOUNT ENGINEERING COMPANY TEST REPORT
QUALITY CONTROL APPROVED   IPTS 1948

MODEL 146MA100F4X
SERIAL 6973
DATE 12 26 72

ACTUAL CALIBRATION POINTS

TEMP C	RESISTANCE OHMS
0.0000	99.97400
100.0258	138.93400
260.0031	198.94600

ALPHA IS   .00389602
DELTA IS   1.41905
BETA   IS   .11000 BELOW 0 DEG C
BETA   IS   .00000 ABOVE 0 DEG C

TEMP C	RESISTANCE OHMS
10.00	103.91875
20.00	107.85245
30.00	111.77510
40.00	115.68668
50.00	119.58721
60.00	123.47669
70.00	127.35511
80.00	131.22249
90.00	135.07881
100.00	138.92407
110.00	142.75828
120.00	146.58143
130.00	150.39352
140.00	154.19456
150.00	157.98456
160.00	161.76349
170.00	165.53138
180.00	169.28820
190.00	173.03396
200.00	176.76868
210.00	180.49235
220.00	184.20496
230.00	187.90652
240.00	191.59702
250.00	195.27626
260.00	198.94485
270.00	202.60218
280.00	206.24847
290.00	209.88369
300.00	213.50787
310.00	217.12099
320.00	220.72304
330.00	224.31406
340.00	227.89402

ROSEMOUNT ENGINEERING COMPANY TEST REPORT
QUALITY CONTROL APPROVED   IPTS 1948

MODEL 145MA10014X
SERIAL 7760
DATE 6 12 73

ACTUAL CALIBRATION POINTS

TMP C	RESISTANCE OHMS
0.0000	100.13750
00.0248	132.15600
260.1136	199.35200

ALPHA IS   .00329553
DELTA IS 1.36659
BETA IS   .11000 BELOW 0 DEG C
BETA IS   .00000 ABOVE 0 DEG C

TMP C	RESISTANCE OHMS
-200.00	17.84442
-190.00	22.18666
-180.00	26.49459
-170.00	30.77040
-160.00	35.01610
-150.00	39.23368
-140.00	43.42499
-130.00	47.59178
-120.0	51.73568
-110.00	55.85826
-100.00	59.96096
-90.00	64.04509
-80.00	68.11191
-70.00	72.16255
-60.00	76.19805
-50.00	80.21931
-40.00	84.22718
-30.00	88.22237
-20.00	92.20549
-10.00	96.17706
0.00	100.13750
10.00	104.08707
20.00	108.02583
30.00	111.95376
40.00	115.87089
50.00	119.77719
60.00	123.67267
70.00	127.55735
80.00	131.43119
90.00	135.29422
100.00	139.14643
110.00	142.98783
120.00	146.81841
130.00	150.63817

ROSEMOUNT ENGINEERING COMPANY TEST REPORT

MODEL 146MA100 4X
SERIAL 7760
DATE 6 12 73

TEMP	RESISTANCE OHMS
40.00	154.44712
50.00	158.24523
60.00	162.03354
70.00	165.80403
80.00	169.57470
90.00	173.32956
200.00	177.07359
210.00	180.60680
220.00	184.52920
230.00	188.24078
240.00	191.94154
250.00	195.63149
260.00	199.31062
270.00	202.47893
280.00	206.63642
290.00	210.28309
300.00	213.91895
310.00	217.54398
320.00	221.15821
330.00	224.76161
340.00	228.35419
350.00	231.93596
360.00	235.50690
370.00	239.06703
380.00	242.61635
390.00	246.15484
400.00	249.68252
410.00	253.19938
420.00	256.70542
430.00	260.20064
440.00	263.68504
450.00	267.15863
460.00	270.62140
470.00	274.07335
480.00	277.51448
490.00	280.94480
500.00	284.36430

ROSEMOUNT ENGINEERING COMPANY TEST REPORT
QUALITY CONTROL APPROVED   IPTS 1948

MODEL 146MA100F4X
SERIAL 7761
DATE 6 12 73

ACTUAL CALIBRATION POINTS

TEMP C	RESISTANCE OHMS
0.0000	100.12950
100.0472	139.18100
260.1230	199.35700

ALPHA IS   .00399828
DELTA IS   1.41905
BETA IS   .11000 BELOW 0 DEG C
BETA IS   .00000 ABOVE 0 DEG C

TEMP C	RESISTANCE OHMS
-200.00	17.70899
-190.00	22.06016
-180.00	26.37674
-170.00	30.66090
-160.00	34.91472
-150.00	39.14012
-140.00	43.33899
-130.00	47.51307
-120.00	51.66401
-110.00	55.79334
-100.00	59.90252
-90.00	63.99288
-80.00	68.06567
-70.00	72.12201
-60.00	76.16293
-50.00	80.18937
-40.00	84.20214
-30.00	88.20198
-20.00	92.18949
-10.00	96.16519
0.00	100.12950
10.00	104.08268
20.00	108.02479
30.00	111.95581
40.00	115.87575
50.00	119.78463
60.00	123.68242
70.00	127.56912
80.00	131.44476
90.00	135.30931
100.00	139.16280
110.00	143.00520
120.00	146.83651
130.00	150.65677

ROSEMOUNT ENGINEERING COMPANY TEST REPORT

MODEL L40M/100H4X
SERIAL 7751
DATE 6 12 73

TMP	RESISTANCE OHMS
40.00	154.46594
50.00	158.26402
60.00	162.05105
70.00	165.82696
80.00	169.59182
90.00	173.34560
200.00	177.08829
210.00	180.81991
220.00	184.54046
230.00	188.24991
240.00	191.94830
250.00	195.63562
260.00	199.31184
270.00	202.97700
280.00	206.63107
290.00	210.27406
300.00	213.90597
310.00	217.52682
320.00	221.13658
330.00	224.73526
340.00	228.32286
350.00	231.89939
360.00	235.46484
370.00	239.01920
380.00	242.56251
390.00	246.09473
400.00	249.61586
410.00	253.12592
420.00	256.62489
430.00	260.11280
440.00	263.58962
450.00	267.05536
460.00	270.51003
470.00	273.95362
480.00	277.38614
490.00	280.80756
500.00	284.21793

APPENDIX G

CONSTRUCTION DRAWINGS

BLACKBODY	SIMULATOR
AS EMPLY	70 - 120
10/13/73	H.A.D. B-11

181

NOTES:

1) ALUMINUM
2) MAKE ONE (1)
3) MACHINE FINISH

4-40 THRU
THREE (3) PLACES @
120°

TYPICAL- DRILL AND COUNTERBORE
FOR 6-32 BUTTON HEAD CAP SCREWS
IN SIX (6) PLACES

C'SINK FOR APERTURE

2.875 DIA
2.375 DIA
.625
.225
.375
175°
30°
50°
70
3.125 DIA
4.002
4.227

BLACKBODY	SIMULATOR
INNER SHIELD	70-121
6-14-73	W A DeBell

LOC PIN HOLES
3 PLCS

750 .125

2 DD

1.250

.275

.125

.0625 DIA

.60

.124 DIA

.125 DIA

20 GROOVES /INCH
ALL BUT TOP AND BOTTOM 1/8"

.050

HTR. WNDG ANCHOR
HOLES 2 PLCS

THERMOMETER HOLES
3 PLCS.

1.50

.25

60°

NOTES:

1) ALUM. 6061-T651
2) MACHINE FINISH ONLY
3) MAKE THREE (3)
4) DO NOT ASSEMBLE
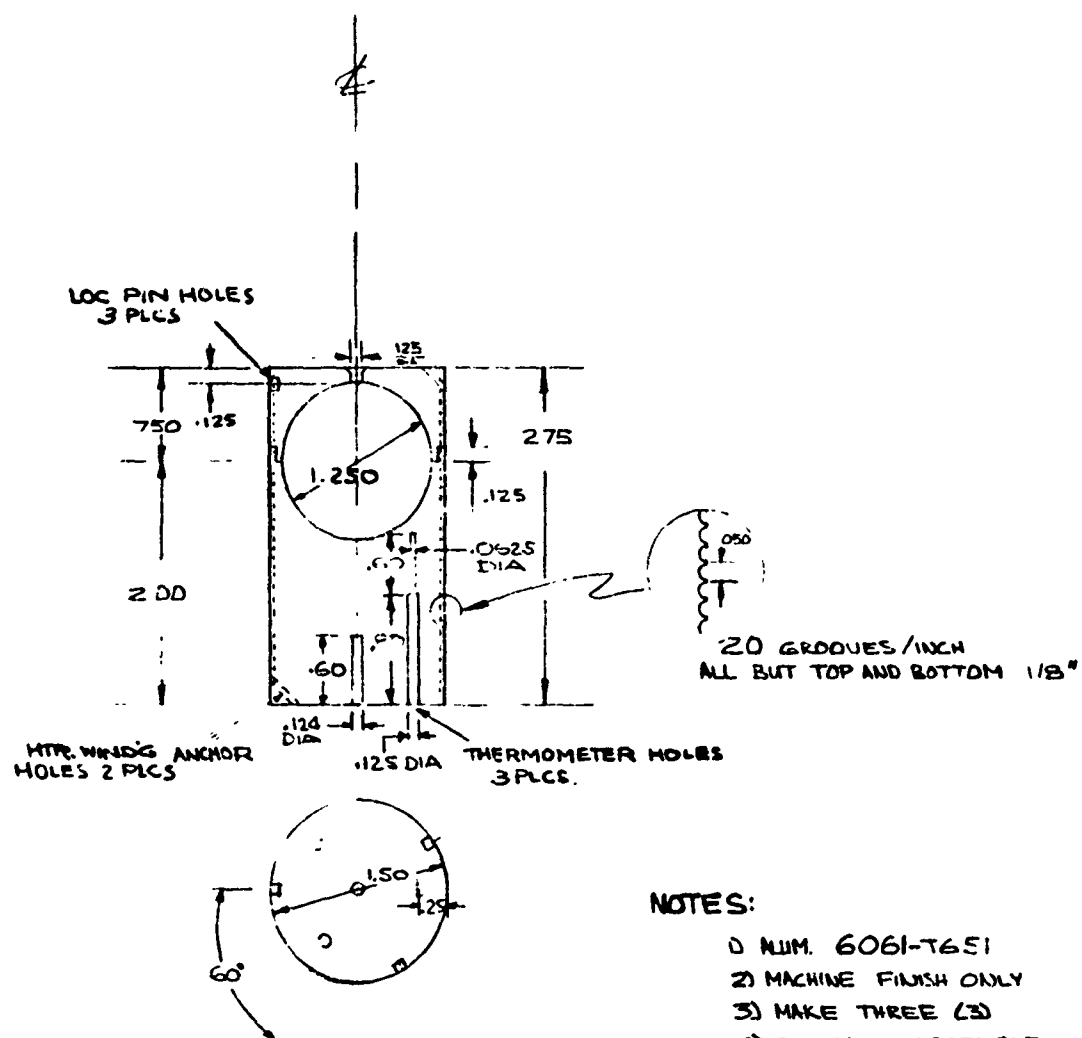
| BLACKBODY SIMULATOR |
| LARGE CAVITY |
| M.A.DeBall | JUNE 13,1973 |
| DWG. NO 70-116 | |

TYPICAL: TAP SIX (6)
4-40 AS SHOWN

TYPICAL: TAP THREE
(3) 4-40 THRU

TYPICAL: TAP SIX (6)
6-32 AS SHOWN

1.60 APPROX

1.30 APPROX

.35 RAD

17.5°

.25

.300

.25

.20 DIA.

1.00 DIA.

NOTES:
1) ALUMINUM
2) MAKE ONE (1)
3) MACHINE FINISH

TYPICAL: TAP
SIX (6) 1/4-20 HOLE
ON THREE INCH
BOLT CIRCLE
@ 60°

BLACKBODY SIMULATOR	
BASEPLATE	70-123
7-18-70	M. A. DeBell
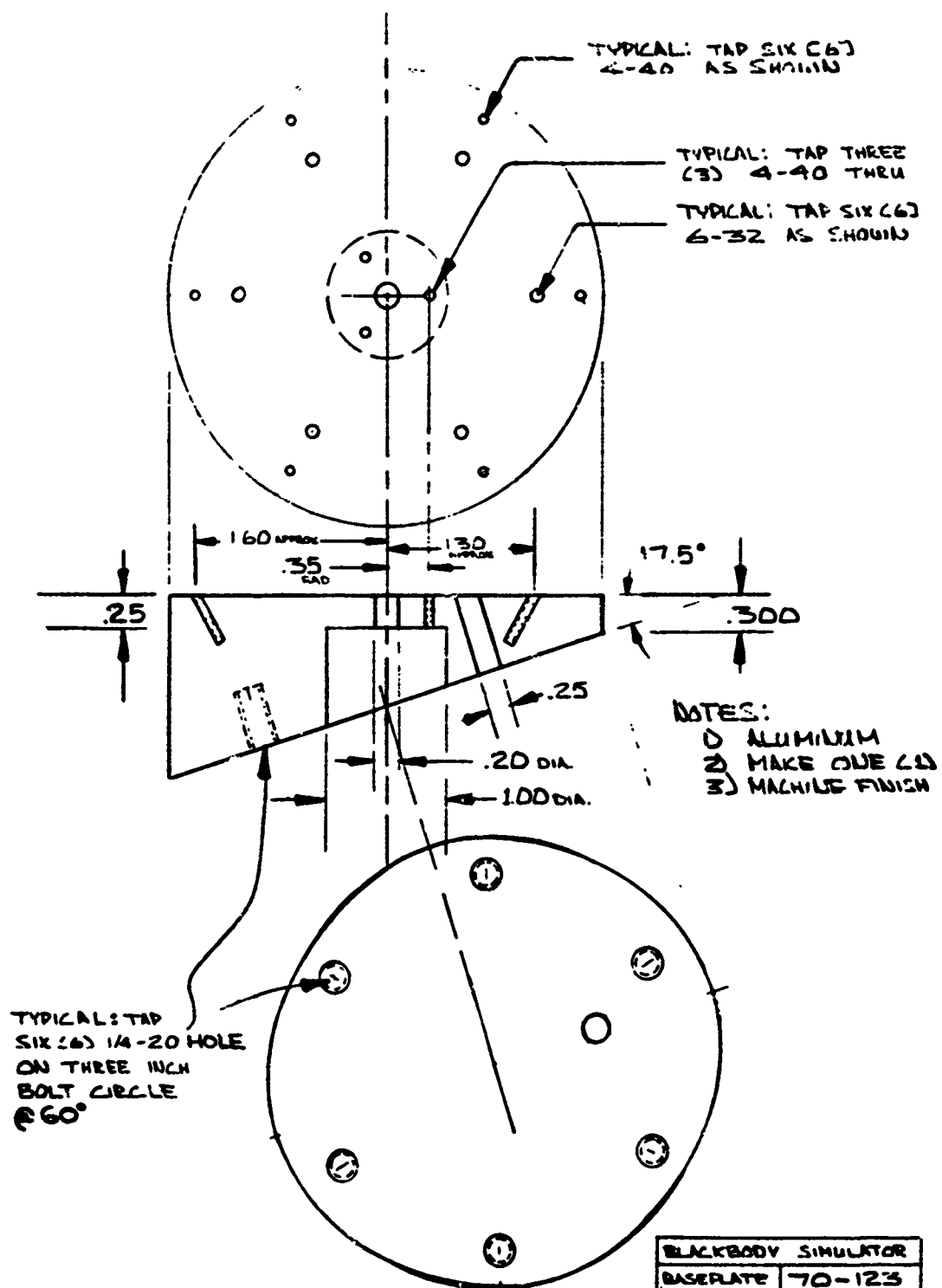
**DETAIL DRAWING SHOWING TEMPERING
OF HEATER WIRE LEADS AND PRT WIRE
LEADS**

3 each PRT's
with 4 wire
assemblies per
PRT

3 in.   12 in.

7 strands of 0.003-in. diam
copper wire with teflon insulation

0.0125-in. diam platinum
wire with fiberglass sheath insulation

Two each
heater wires

Fiberglass
sheath

AWG-25 nichrome wire
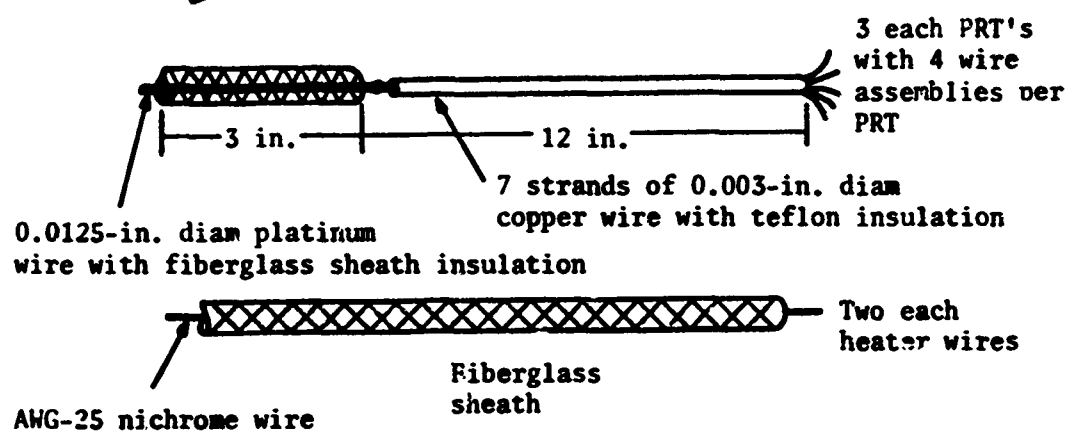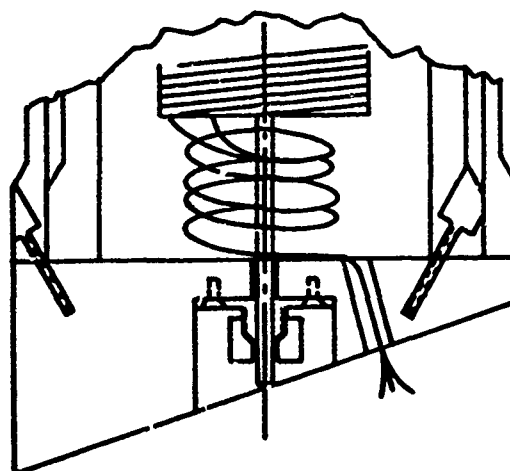
APPENDIX H

CEMENT DATA*

General Description

SermeTel P-1 and SermeTel PBX Ceramic Cements consist of two separate components - a dry mix and an activating solvent. Packaging in dry and liquid components eliminates waste as only enough for the job at hand need be prepared. These cements are easily applied and form strongly adherent bonds with aluminum, Inconel, Stainless, low carbon steel and titanium, as well as with a number of alloys. The bond is air-setting, and curing is accomplished at relatively low temperatures. The cements are completely inorganic and have no flash point. The toxicity factor is low. After curing at 600°F, these cements become water insoluble and are insoluble in organic solvents.

Cement Applications

Used in high temperature instrumentation such as strain gages, thermocouples and transducers, PBX and P-1 ceramic bondings and coatings maintain their electrical insulating properties and mechanical strength at elevated temperatures. P-1 has better bond strength, PBX has better electrical resistance at temperatures above 1000°F. Hence, in some applications, both cements are used - a precoat of P-1 and PBX as the insulating cement. In equipment which must function under severe environmental conditions - in Steam Turbines, Jet Engines, Nuclear Reactors and Missile Systems, PBX Ceramic Cement has proved thoroughly dependable.

Surface Preparation

In order to form a strong bond, the surface of the metal to be coated must be absolutely clean. It should be free of scale, film, grease, oil and fingerprints. Stronger adhesion will be obtained if the surface is slightly roughened. (Grit blasting or grit paper is excellent.) Rinse the area clean of metal particles and grit using distilled water. Test the surface with a clean cotton swab for cleanliness.

Mixing Procedure

The recommended method for mixing SermeTel Ceramic Cements is as follows: PBX: Add the mix to the liquid vehicle in the proportions of 2-1/4 grams of dry material to 1cc of liquid, mixing thoroughly. Set the mixture aside for 30 minutes to an hour to allow the chemical action to take place. If the mixture seems to thin or to thick, the ratio of solids to liquid may be varied to some degree, depending on the application.

---

*From Surface Engineering Bulletin #200, SermeTel Division of Teleflex, Inc., P.O. Box 187, North Wales, Pa. 19454, Tel. (215) 699-4861.

P-1: Follow the same procedure as previously stated, but start with a ratio of 2 grams of dry material to 1 cc of liquid. Allow a li le more time for the chemical reaction to take place than with the PBX; no bubbles should be visible at the time of application.

Application and Cur ing Procedure

The mixed cements may be applied by means of a brush, spatula, spraying or dipping. Allow the coated metal to air-dry in a clean, dry atmosphere for 30 minutes to one hour. Drying at room temperature is preferable but when high humidity conditions prevail, it may be necessary to use infra-red lamps or even a 100-watt electric light bulb to counteract humid conditions. If infra-red lamps are used, it is suggested whenever possible to apply heat under the coated surface in order to prevent rapid hardening of the skin while the interior still retains some moisture. If a comparatively thick application is required (on the order of 5 mils), several thin coats are preferable to one thick coat, allowing time to air-dry and cure briefly between applications of cement.

SermeTel PBX and SermeTel P-1 will bond to ceramic surfaces as well as metals. The procedure is the same.

After completion of air-set:

.....1) Set oven to 200°F and bake for 1 hour.
.....2) Set oven to 600°F and bake for 1 hour minimum.
.....3) Allow oven to cool at normal rate before removing coated part.

Coating Electronic Components

Spraying or dipping may be accomplished in most cases with a single coating. Dip coating is more rapid and economical and eliminates spray equipment. Beyond thicknesses of .004" - .005", multiple coating with slow and complete air-set and brief cure between coats is desirable.

If complete moisture-proofing is desired from ambient to 800°F, we suggest a top coat of our SermeTel Sealant SD, which provides an hermetic seal. If moisture resistance only is required from ambient to 500°F - 600°F, we suggest the following procedure:

.....1) Heat the completely cured area to 150°F.
.....2) While still warm, spray or brush a thin film of Silicone Lacquer over the coated area and allow to cool.

Both SermeTel PBX and SermeTel P-1 have hygroscopic tendencies until cured.

Potting Elements

Painstaking cleanliness is a major factor in successful potting of elements. Parts should be cleaned by procedures best suited. PBX is the preferred cement for potting applications although P-1 is also used.

.....1) Remove all foreign matter from object to be filled.
.....2) Fill tube or cavity with cement; gentle agitation will aid in eliminating air bubbles.

.....3) Air dry slowly under infra-red lamps; volume of cement used will govern drying time.

.....4) Cure slowly at 200°F; set oven at 600°F and allow oven to reach this temperature at a normal rate.

.....5) Cure for 1 hour at 600°F, longer if possible. Cements will become water insoluble at this temperature. Allow oven to cool normally.

Tentative Resistivity Values

I°C	P-1	PBX
625	3.6×10^7	
650	2.4×10^7	
700	1.2×10^7	
750	5.8×10^6	
800	2.4×10^6	5×10^7
825	1.8×10^6	
850	$.59 \times 10^6$	9.2×10^6
875		4.6×10^6
900		3.9×10^6
925		2.8×10^6
950		1.6×10^6
975		$.92 \times 10^6$

Method

Samples approximately 4 cm. by 5 mm. by 1 mm. were prepared with two platinum wires embedded in the cement. Wet strength was provided by pressing lightly between two sheets of paper which subsequently burned off. Samples were dried at 110°C, then placed in furnace and heated slowly to 400°C for curing. The furnace power was then increased and measurements of resistance made as the temperature increased. A Chromel-alumel thermocouple in close proximity to the samples was used to indicate temperature.

Results

Some cracking parallel to the direction of current flow occurred in the P-1. The PBX appeared still in good condition after heating to 975°C. The resistances as functions of temperature are shown graphically on the attached sheet and tabulated above. These values should be considered as qualitive only, as variations in preparation of samples may be expected to lead to variations in the exact resistivity.